Synthesis and Investigation of Functional Polymer Materials

Dissertation

zur Erlangung des Grades
"Doktor der Naturwissenschaften“
(Dr. rer. nat.)

am Fachbereich Chemie, Pharmazie und Geowissenschaften
der Johannes Gutenberg-Universität
in Mainz

im Promotionsfach Makromolekulare Chemie

Christoph F. Kins
geboren in Offenbach a. M.

April 2012

Die vorliegende Arbeit wurde in der Zeit

von Oktober 2009 bis April 2012

am Max-Planck-Institut für Polymerforschung in Mainz

unter der Anleitung von … angefertigt.

Dekan:	…
1. Berichterstatter:	…
2. Berichterstatter:	…
Datum der mündlichen Prüfung:	24.05.2012

Meinen Eltern

Table of Contents

1 General Introduction 8

2 Background of Research Methods 11

2.1 Solid State NMR 11

2.1.1 Zeeman Interaction 11

2.1.2 Nuclear Spin Interactions 12

2.1.3 Chemical Shift 13

2.1.4 Dipolar Coupling 16

2.1.5 Quadrupolar Coupling 19

2.2 Mechanical Measurements 25

2.2.1 Tensile tests 25

2.2.2 Dynamic Mechanical Analysis 27

3 Literature 30

Part I

4 Introduction 32

4.1 Strategies for Tuning Epoxy Properties 32

4.1.1 Mechanical Properties of Polymers 32

4.1.2 Monomers and Additives 32

4.1.3 Fillers 35

4.1.4 Molecular Fortification 36

5 Motivation 39

6 Results and Discussion 41

6.1 Outline 41

6.2 Reaction of Phosphonates 42

6.3 Identification of Suitable Cure Conditions 47

6.3.1 Reactivity of Phosphonate Based Fortifiers 47

6.3.2 Reactivity Difference of Methyl and Benzyl Group 49

6.3.3 Clustering of Phosphonates 51

6.3.4 Side Reactions 51

6.4 Thermal and Mechanical Properties 53

6.5 Effect of Aging on Thermal and Mechanical Properties 58

6.6 Fortifier Dynamics 64

6.6.1 Deuteron NMR 64

6.6.2 ^{31}P Chemical Shift Anisotropy 66

7 Summary 70

8 Experimental Section 72

8.1.1 Network Fabrication 72

8.1.2 Materials 72

8.1.3 Synthesis 72

8.1.4 Thermal and Mechanical Analysis 79

8.1.5 Line Shape Analysis 79

9 Literature 80

Part II

10 Introduction 84

10.1 Fuel Cells 84

10.1.1 Need for Alternative Energy Sources 84

10.1.2 Basic Principles 84

10.1.3 Polymer Electrolyte Membranes 89

11 Motivation and Outline 92

11.1 Block Copolymers 92

11.2 Characterization Methods 94

12 Results and Discussion 95

12.1 Synthesis and Characterization 95

12.2 Morphology 98

12.3 ^{1}H MAS NMR 101

12.4 Proton Conductivity 105

12.5 ^{2}H Quadrupolar NMR 107

12.6 ^{1}H Pulsed Field Gradient NMR 112

13 Summary 118

14 Experimental Section 119

14.1.1 Materials 119

14.1.2 Synthesis of random sulfonated copolyimide 119

14.1.3 Synthesis of multiblock sulfonated copolyimide 119

14.1.4 Preparation of sulfonated copolyimide membranes 120

14.1.5 Membrane characterization 120

14.1.6 ^{1}H PFG NMR 123

14.1.7 ^{2}H NMR 124

15 Literature 125

16 Appendix 130

16.1 Curriculum Vitae 130

16.2 Acknowledgements 131

1 General Introduction

Functional Materials

Functional Materials cover a broad range of material classes including polymers, biomaterials, glasses, metals, ceramics, composite materials etc. Thus, they are not limited to the traditional classification organic, inorganic or metallic compounds but also comprise hybrid mixtures. Per definition, they have to possess a particular intrinsic property and function of their own, where important functions include magnetism, ion conductivity, energy storage and conversion, toughness, elasticity or superior adhesion, to name a few. These properties are closely related to the underlying design of the material. Therefore, rational control over local arrangements of the building blocks or functional moieties on length scales ranging from nano- to micrometer (µm) scale is highly necessary. In general, functional materials are tailored for a specific, definite purpose and the continuous development of synthetic procedures and controlled adjustment of resulting properties constitutes an essential task to master the challenges of increasing urbanization, mobility, energy and food supply of a growing world population in view of rather limited natural resources. Further stimulus for materials development stems from the need for advanced materials in future space and military applications, where conventional materials often fail due to extremely harsh conditions.[1] In addition to their specific function successful commercialization of newly invented high performance materials require reliable shape persistency, flame and chemical resistance and long life span.

In this thesis, two rather distinct examples of functional materials are studied, namely epoxies with improved mechanical properties (Part I) and proton conducting copolymers with potential application in fuel cells (Part II). The increasing complexity of such materials calls for advanced techniques of characterization over a wide range of length- and time scales.[2] The primary technique used in this thesis is solid state NMR, which therefore is briefly introduced here.

Solid-State NMR

Polymers constitute a particularly important class of possibly functional materials due to their extraordinary range of properties. Many of them provide high performance at rather low cost and may be readily modified by a variety of additives and processing techniques. In addition to selective chemical modifications, tailored morphologies may allow for property enhancement.[3] While formation of particular morphologies in principle can be governed by immiscibility between chemically distinct blocks or particles, a rational adjustment of desired material properties often depends on a complex interplay of several factors that are typically not well understood.

In addition, polymer systems are often inhomogeneous, comprising partly crystalline and disordered fractions. Below a characteristic glass transition temperature (T_g), such materials tend to be relatively brittle, while above T_g but well below the melting point (if existing), enhanced segmental motion of polymer chains constituting the amorphous part transfers the polymer into a soft state. In conclusion, mobility of polymer segments is already pronounced in the solid state, rendering local dynamics a crucial parameter for polymer performance.

Reliable determination of polymer structures and morphology based on powder diffraction techniques can be rather challenging, as amorphous systems lack the regularity of crystal lattices[4]. In contrast, modern solid-state NMR facilitates characterization of short-range ordered structural motifs. Solid-state NMR is a suitable method for the selective analysis of localized molecular and segmental motions, e.g. based on averaging of anisotropic nuclear spin interactions. This includes the chemical shift anisotropy (CSA), quadrupolar interactions and dipole-dipole couplings, depending on the time scale of the dynamics and the considered probe nuclei, thus rendering solid-state NMR a valuable tool in polymer research. In this thesis, the ^{31}P CSA and the line width of acidic ^{1}H were exploited to determine additive dynamics (chapter 6.6) and proton mobility (chapter 12.3) respectively. Anisotropic channel alignment was probed by ^{2}H quadrupolar NMR in sulfonated poly(imide) (SPI) membranes (chapter 12.5).

Part I

Epoxies are industrially produced on large scales and similar to other technically relevant polymer systems, their bulk properties are mainly controlled by admixture of a multitude of additives. Since they are extensively used as adhesives and as matrix in composite materials, their thermal and mechanical properties are quite important. Therefore, in the first part of this thesis, possible improvement of mechanical properties of model epoxies upon admixture of novel phosphonate-based additives as well as the underlying fortification mechanism were investigated in detail.

Part II

In the second part, the morphology, structure and resulting proton conductivity (or mobility) of sulfonated block copolyimide membranes, including anisotropic channel alignments, have been studied. Indeed, such materials are considered promising for fuel cell application and hence environmentally less detrimental energy supply. Intensive research efforts are currently devoted to the rational design of sulfonated (and to some extent phosphonated) aromatic polymers, which have considerable potential to eventually replace the commonly utilized perfluorosulfonated ionomers, including the industrial benchmark material Nafion.

2 Background of Research Methods

2.1 Solid State NMR[5-11]

NMR spectroscopy is a method that exploits the electronic environment of nuclei and their interaction with other nuclei on the nanometer (nm) scale. This allows for both structure elucidation and the investigation of dynamics of chemical compounds. Furthermore, it is also possible to determine concentrations, chemical compositions, reaction rates, bond angles and morphologies of a variety of systems, just to name a few applications. Hence, NMR has become an irreplaceable tool in many fields of science, in academia as well as in industry. Especially with regard to disordered solids that do not form suitable crystals (e.g. polymers and inorganic glasses), it nicely supports diffraction techniques as it does not require a periodic structure. [12-14]

2.1.1 Zeeman Interaction

In organic chemistry, the most abundant elements are hydrogen, carbon, oxygen, nitrogen and phosphorus. Every chemical element has different variants, called isotopes. They share the same number of protons but differ in the number of neutrons. This has tremendous effects on the suitability of nuclei for NMR experiments. In general, it is necessary that the nucleus in question possesses an *angular momentum* $\mathbf{P}$ which is proportional to the *magnetic moment* $\boldsymbol{\mu}$. The bold character denotes a vector or matrix quantity. The proportionality factor is the *magnetogyric ratio* γ.

$$|\boldsymbol{\mu}| = \gamma|\mathbf{P}| = \gamma\sqrt{I(I+1)}\hbar \tag{2.1}$$

Where $\hbar = {}^{h}/_{2\pi}$ is Planck's constant and I is the *angular momentum quantum number*. From this it becomes clear that $\mathbf{P}$ is a quantized parameter being equal to zero if $I = 0$. This applies to important isotopes such as ^{12}C and ^{16}O and excludes them from any NMR experiments, because the energy splitting of a nucleus in a static magnetic field $\mathbf{B_0}$ along z-direction (per definition) is given by

$$\Delta E = E(m) - E(m+1) = \gamma\hbar|\mathbf{B_0}| \tag{2.2}$$

and the *magnetic quantum number* m can only take values according to $m = I, I-1, \dots, -I$. For $I = 0$, there is no transition and hence no detectable radiofrequency signal. Importantly, $\Delta m = \pm 1$ for quantum mechanical reasons. The angular momentum quantum number I

itself is restricted to integer and half-integer values. Equation (2.2) was derived from the classical picture of the energy of a magnetic dipole placed in a magnetic field

$$E = -\mu_z|\mathbf{B_0}| = -\gamma I_z|\mathbf{B_0}| = -m\gamma\hbar|\mathbf{B_0}| \tag{2.3}$$

From Equation (2.2), the transition frequency is readily calculated according to

$$h\nu = \gamma\hbar|\mathbf{B_0}| \tag{2.4}$$

$$\nu_{\mathrm{L}} = \frac{\gamma|\mathbf{B_0}|}{2\pi} \tag{2.5}$$

ν_{L} is called the *Larmor frequency* and is in the order of megahertz (MHz) for common magnetic fields (i.e. 5 to 20 Tesla).

The signal-to-noise ratio of a magnetic resonance experiment strongly depends on the gyromagnetic ratio γ and the absolute temperature T. Sensitivity is an important issue in NMR due to the small energy level difference ΔE (cf. Equation 2.2) that leads to small population differences between the lower and higher energy levels. As a rule of thumb, the signal intensity is $\propto {}^{1}/_{T}$ and $\propto |\mathbf{B_0}|$. Furthermore, the signal intensity is proportional to the number of spins in the experiment, rendering large sample volumes favorable.

2.1.2 Nuclear Spin Interactions

To develop and describe NMR results, it is necessary to put the interaction of the nuclear spin with electric and magnetic fields into a theoretical frame. These electromagnetic fields may originate from internal spin interactions or are externally applied. Thus, they are divided into internal and external interactions

$$\widehat{H} = \widehat{H}_{\mathrm{ext}} + \widehat{H}_{\mathrm{int}} \tag{2.6}$$

Irrespective of its specific interaction, each Hamiltonian can be formally expressed as

$$\widehat{H}_i = -\gamma\hbar\,\hat{\mathbf{I}}\cdot\mathbf{B_i} = -\gamma(\hat{I}_x B_x^i + \hat{I}_y B_y^i + \hat{I}_z B_z^i) \tag{2.7}$$

where the interaction between a local field $\mathbf{B_i}$ and a nuclear spin I is described.

External interactions are

- Zeeman interaction $\widehat{H}_Z$
- Radiofrequency pulses $\widehat{H}_{RF}$

Internal interactions are

- Chemical shift $\widehat{H}_{CS}$
- Dipole-dipole coupling $\widehat{H}_{DD}$
- Quadrupolar coupling $\widehat{H}_Q$
- Indirect spin-spin coupling $\widehat{H}_J$

With the terms arranged according to their approximate strength the full Hamiltonian is

$$\hat{H} = \sum_i \hat{H}_Z^{(i)} + \sum_i \hat{H}_Q^{(i)} + \sum_i \hat{H}_{RF}^{(i)} + \sum_{i \neq j} \hat{H}_{DD}^{(i)} + \sum_i \hat{H}_{CS}^{(i)} + \sum_{i \neq j} \hat{H}_J^{(i)} \qquad (2.8)$$

However, this arrangement is only valid for most spin 1/2 nuclei. Some transition metal nuclei exhibit a low gyromagnetic ratio (related to the Zeeman interaction) and a large quadrupolar interaction that is in the order of a few MHz. Notably, this has also crucial consequences for the quantum mechanical description and complicates theoretic approaches if both interactions are of similar size.

$\hat{H}_J$ is in the order of a few hertz (Hz) and much weaker than the next larger Hamiltonian $\hat{H}_{CS}$, whose magnitude is around several kilohertz (kHz). $\hat{H}_{CS}$, $\hat{H}_{DD}$ and $\hat{H}_Q$ are strongly anisotropic, i.e. a strong dependence of sample orientation relative to the applied magnetic field $\mathbf{B_0}$ is found. In the liquid state, the high mobility of the molecule of interest associated with fast rotation and tumbling averages nearly all anisotropic interactions so that the effect of $\hat{H}_J$ as isotropic component may be very prominent and valuable. Ironically, $\hat{H}_J$ is mostly neglectable in the solid state.

2.1.3 Chemical Shift

The electrons surrounding the nucleus interact with $\mathbf{B_0}$, similar to the nucleus itself. According to classical physics, they start to circulate in their molecular orbitals under the influence of the applied magnetic field. In doing so, they produce (small) magnetic fields itself that add up to the external magnetic field. Hence, the effective magnetic field varies for identical nuclei if their molecular environment, i.e. electron density distribution, is different.

$$\mathbf{B_{loc}} = \boldsymbol{\sigma} \cdot \mathbf{B_0} \qquad (2.9)$$

$\mathbf{B_{loc}}$ is the local field produced and $\boldsymbol{\sigma}$ the *chemical shielding tensor*. Accurate calculation of unknown chemical shielding values is challenging.[15]

The shielding interaction generates oscillating fields perpendicular to the direction of $\mathbf{B_0}$ only. So in the laboratory frame, specified by the direction of the applied field $\mathbf{B_0}$ (parallel to z-direction), each component of $\boldsymbol{\sigma}$, except σ_{zz}^i, vanishs. It determines the shielding field in the direction of the quantization axis. Note that $|\mathbf{B_0}| = B_z$ in the laboratory frame.

$$\hat{H}_{cs} = +\gamma \hat{I}_z \sigma_{zz}^i B_z \qquad (2.10)$$

From this Equation it can be seen, that the chemical shift interaction is proportional to B_z. However, in a powder sample with sample molecules possessing all possible orientations, we

cannot define the orientation of $\boldsymbol{\sigma}$ with respect to the molecule in such a way that σ_{zz}^{i} is constant for every molecule orientation. So it is convenient to define $\boldsymbol{\sigma}$ in the *principal axis frame* (PAF), where all components except for the diagonal are zero. This frame is fixed with respect to the molecule geometry. $\sigma_{xx}^{\mathrm{PAF}}$, $\sigma_{yy}^{\mathrm{PAF}}$ and $\sigma_{zz}^{\mathrm{PAF}}$ are the *principal values* and by convention $|\sigma_{zz}-\sigma_{\mathrm{iso}}| \geq |\sigma_{xx}-\sigma_{\mathrm{iso}}| \geq |\sigma_{yy}-\sigma_{\mathrm{iso}}|$, where σ_{iso} is the *isotropic chemical shielding*. It is defined by

$$\sigma_{\mathrm{iso}} = {}^{1}/_{3}\,\mathrm{Tr}\{\boldsymbol{\sigma}^{\mathbf{PAF}}\} = {}^{1}/_{3}\left(\sigma_{xx}^{\mathrm{PAF}} + \sigma_{yy}^{\mathrm{PAF}} + \sigma_{zz}^{\mathrm{PAF}}\right) \tag{2.11}$$

Notably, σ_{iso} is the *isotropic chemical shielding* and identical to the chemical shielding value observed in liquid state NMR (however usually expressed as chemical shift δ, cf. Equations (2.16) and (2.19)). $\boldsymbol{\sigma}^{\mathbf{PAF}}$ is not traceless and thus, $\boldsymbol{\sigma}^{\mathbf{PAF}}$ contains an isotropic element.

The total spectral frequency is the Larmor frequency of the bare nucleus ω_0 plus the chemical shift contribution $\omega_{\mathrm{cs}}(\theta.\phi)$:

$$\omega = \omega_0 + \omega_{\mathrm{cs}}(\theta.\phi) = \gamma B_0(1-\sigma_{zz}^{l}) \tag{2.12}$$

Note that ω is given in rad/s (instead of Hz). For a specific nuclei, the orientation of $\boldsymbol{\sigma}^{\mathbf{PAF}}$ with respect to the laboratory frame is defined by the polar angles θ and ϕ and yields

$$\omega_{cs}(\theta,\phi) = \underbrace{-\omega_0\sigma_{\mathrm{iso}}}_{\omega_{\mathrm{iso}}} - \frac{1}{2}\omega_0(3\cos^2\theta - 1 + \eta\sin^2\theta\cos 2\phi) \tag{2.13}$$

where η is termed asymmetry and defined as

$$\eta = \left(\sigma_{yy}^{\mathrm{PAF}} - \sigma_{xx}^{\mathrm{PAF}}\right)/\left(\sigma_{zz}^{\mathrm{PAF}} - \sigma_{\mathrm{iso}}^{\mathrm{PAF}}\right) \tag{2.14}$$

Similarly, the anisotropy Δ is defined according to

$$\Delta = \sigma_{zz}^{\mathrm{PAF}} - \sigma_{\mathrm{iso}} \tag{2.15}$$

These definitions follow the Haeberlen notation. For the sake of completeness, it should be mentioned that further notations exist. Equations (2.13) and (2.14) define the resonance frequency for a given orientation. To obtain the experimental powder pattern, it is necessary to sum up over all orientations because the resulting spectrum is a superposition of single sharp resonances. In this respect every orientation has to be weighed corresponding to its probability of occurrence.

The *chemical shift* δ is defined as

$$\delta\ (\mathrm{ppm}) = 10^6 \cdot \frac{\nu_{\mathrm{L}} - \nu_{\mathrm{ref}}}{\nu_{\mathrm{ref}}} \tag{2.16}$$

with ν_{ref} as frequency of a reference compound and ν_{L} as Larmor frequency of the respective nucleus in question. This definition is introduced for reasons of convenience. First, the factor 10^6 shifts the values for the chemical shift in the range of 0 – 100 ppm for the

important nuclei ^{1}H and ^{13}C (hence, δ is expressed in parts per million *ppm*). Second, the Larmor frequency ν_{L} for a given nucleus is proportional to the external magnetic field strength $|\mathbf{B_0}|$ (cf. Equation (2.5)). Dividing $(\nu_{\mathrm{L}} - \nu_{\mathrm{ref}})$ by ν_{ref}, this field-dependence is canceled out and thus δ remains constant for different spectrometer field strengths. Notably, even though the separation of two resonances remains constant in *ppm*, the separation in Hz, i.e. resolution, is proportional to $|\mathbf{B_0}|$. In combination with an additional gain in intensity per scan, this explains the wish for high-field spectrometers for most experiments.

Equation (2.17) expresses the relation between δ and σ.

$$\delta_{pq} = \frac{\sigma_{pq,\mathrm{ref}} - \sigma_{pq}}{1 - \sigma_{pq,\mathrm{ref}}} \approx \sigma_{pq,\mathrm{ref}} - \sigma_{pq} \tag{2.17}$$

δ_{pq} is an element of the *chemical shift tensor*

$$\boldsymbol{\delta} = \begin{pmatrix} \delta_{xx} & \delta_{xy} & \delta_{xz} \\ \delta_{yx} & \delta_{yy} & \delta_{yz} \\ \delta_{zx} & \delta_{zy} & \delta_{zz} \end{pmatrix} \tag{2.18}$$

determining the magnitude of the local shielding in p-direction if a magnetic field B_q is applied. $(1 - \sigma_{\mathrm{iso,ref}})$ is approximately 1 because $\sigma_{\mathrm{iso,ref}} \ll 1$.

In analogy to Equation (2.11), δ_{iso} is defined as

$$\delta_{\mathrm{iso}} = {}^{1}/_{3}\left(\delta_{xx}^{\mathrm{PAF}} + \delta_{yy}^{\mathrm{PAF}} + \delta_{zz}^{\mathrm{PAF}}\right) \tag{2.19}$$

Note that the elements are defined in the principal axis frame.

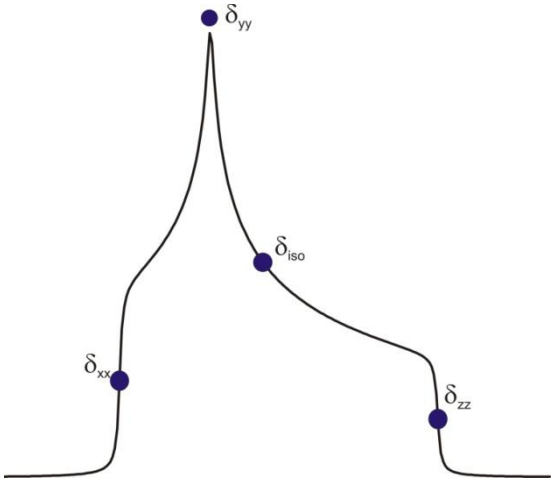

Figure 2.1: Typical chemical shift anisotropy powder pattern with $\eta \neq 0$. Notation is in accordance with the Haeberlen convention. Figure is taken from ref. [16]. It should be noted that δ_{iso} is at the centre of mass of the powder spectrum and not necessarily equal to $(\delta_{xx} + \delta_{zz})/2$.

2.1.4 Dipolar Coupling

As mentioned above, in liquid state NMR $\hat{H}_J$ is often a much appreciated source of information. The term indirect (scalar) spin-spin coupling refers to the mediation of the interaction through a covalent bond connecting two nuclei. Hence, it provides information about *intra*molecular structures. $\hat{H}_J$ is only assessable over the length of a few chemical bonds and depends on the magnitude of the coupling constant *J*. In contrast, dipole-dipole coupling allows for the elucidation of couplings between nuclear spins that are not necessarily connected through covalent bonds. This is of particular interest in the determination of *inter*molecular structures, such as supramolecular complexes, phase separated block copolymers or inclusion compounds.

The dipolar Hamiltonian is given by

$$\hat{H}_{dd} = -2\,\hat{\mathbf{I}} \cdot \mathbf{D} \cdot \hat{\mathbf{S}} \tag{2.20}$$

It should be noted, that this tensorial form is formally similar to Equation (2.10) in that the interaction between a spin $\hat{\mathbf{I}}$ and a local magnetic field (with origin $\hat{\mathbf{S}}$ in Equation (2.20)) is mediated by an interaction tensor. $\mathbf{D}$ is the *dipolar coupling tensor*. However, in the case of chemical shift the local magnetic field is caused by an external magnetic field $\mathbf{B_0}$ rather than another nucleus possessing a magnetic moment. It turns out, that $\mathbf{D}$ is given by

$$\mathbf{D} = \begin{pmatrix} -d/2 & 0 & 0 \\ 0 & -d/2 & 0 \\ 0 & 0 & d \end{pmatrix} \tag{2.21}$$

in the principal axis frame with

$$d = \left(\frac{\mu_0}{4\pi}\right)\frac{\gamma_I \gamma_S \hbar}{r^3} \tag{2.22}$$

The trace of the dipolar coupling tensor is always zero. Thus, the dipolar interaction has no isotropic component and vanishes when it is averaged to zero (e.g. by fast molecular motion).

The external magnetic field $\mathbf{B_0}$ defines the quantization axis as it is much larger than the local field origination from the dipolar coupling. This leads to an anisotropic interaction, i.e. it depends on the direction of $\mathbf{B_0}$ with respect to the vector connecting I with S. The local field caused by *S* at the location of I is calculated according to

$$\hat{\mathbf{B}}_{\mathbf{S}}^{\mathbf{loc}} = \left(\frac{\mu_0}{4\pi}\right)\frac{1}{r^3}(3\cos^2\theta - 1)\hat{\boldsymbol{\mu}}_{\mathbf{S}} \tag{2.23}$$

with the magnetic dipole moment $\hat{\boldsymbol{\mu}}_{\mathbf{S}}$ of spin S.

It is related to the spin angular momentum $\hat{\mathbf{S}}$ by

$$\hat{\boldsymbol{\mu}}_{\mathbf{S}} = \gamma\hbar\hat{\mathbf{S}} \tag{2.24}$$

θ is the polar angle specifying the orientation of the $I-S$ internuclear vector with respect to the $\mathbf{B_0}$ field. The tensor $\mathbf{D}$ is axially symmetric, thus θ is sufficient to describe its orientation in space.

Equation (2.20) may be expanded to

$$\hat{H}_{dd} = -\left(\frac{\mu_0}{4\pi}\right)\gamma_I\gamma_S\hbar\frac{\hat{\mathbf{I}}\cdot\hat{\mathbf{S}}}{r^3} - 3\frac{(\hat{\mathbf{I}}\cdot\mathbf{r})(\hat{\mathbf{S}}\cdot\mathbf{r})}{r^5} \tag{2.25}$$

$$= -\left(\frac{\mu_0}{4\pi}\right)\frac{\gamma_I\gamma_S\hbar}{r^3}(3\cos^2\theta - 1)\left[\hat{I}_z\hat{S}_z - \frac{1}{2}\left(\hat{I}_x\hat{S}_x + \hat{I}_y\hat{S}_y\right)\right] \tag{2.26}$$

$$= -d\frac{1}{2}(3\cos^2\theta - 1)\left[3\hat{I}_z\hat{S}_z - \hat{\mathbf{I}}\cdot\hat{\mathbf{S}}\right] \tag{2.27}$$

d is the dipolar coupling constant defined in Equation (2.22). Equation (2.25) describes the interaction between two spins and can also be readily derived from classical physics theory where the energy of interaction between two point-magnetic dipoles $\boldsymbol{\mu_1}$ and $\boldsymbol{\mu_2}$ is

$$E_{DD} = \left(\frac{\boldsymbol{\mu_1}\cdot\boldsymbol{\mu_2}}{r^3} - 3\frac{(\boldsymbol{\mu_1}\cdot\mathbf{r})(\boldsymbol{\mu_2}\cdot\mathbf{r})}{r^5}\right)\frac{\mu_0}{4\pi} \tag{2.28}$$

where **r** is the vector between both magnetic dipoles.

Notably, the expression of $\hat{H}_{dd}$ according to Equation (2.27) is sufficient for considering the effect of the dipolar coupling on the energy transitions of the nuclei. However, $\hat{H}_{dd}$ has to be expanded if it is necessary to derive the influence of the dipolar coupling on other processes, e.g. relaxation. The most general form is

$$\hat{H}_{dd} = -\left(\frac{\mu_0}{4\pi}\right)\frac{\gamma_I\gamma_S\hbar}{r^3}[A + B + C + D + E + F] \tag{2.29}$$

and known as the *dipolar alphabet*.

Equation (2.27) comprises terms A and B only. Nevertheless, in the case of a two-spin heteronuclear dipolar coupling, i.e. the resonances of spins I and S are well separated, the dipolar Hamiltonian is further truncated:

$$\hat{H}_{dd}^{hetero} = -d\underbrace{(3\cos^2\theta - 1)\hat{I}_z\hat{S}_z}_{\text{Term } A} \tag{2.30}$$

where Term B is discarded. Comparing Equation (2.26) and (2.30), term B is identified as

$$\text{Term } B = -\frac{1}{2}\left(\hat{I}_x\hat{S}_x + \hat{I}_y\hat{S}_y\right)(3cos^2\theta - 1) \tag{2.31}$$

Calculating the transition frequencies yields

$$\omega_{dd}^I = \omega_0^I \pm \frac{1}{2}d(3\cos^2\theta - 1) \tag{2.32}$$

with ω_0^I as transition frequency without dipolar coupling to spin *S*. Note that there are two transitions for spin I, leading to a splitting of the resonance centered around ω_0^I.

Physically this corresponds to one transition where spin I is coupled to spin S being '*spin-down*' and a second transition where I is coupled to spin S being '*spin-up*'. Similar to the chemical shift powder spectrum, it is necessary to sum up over all orientations in order to calculate the powder line shape for the I spin because the resulting spectrum is a superposition of single sharp resonances.

However, calculated spectra as seen in Figure 2.2 are hardly observed. Most often, this is due to two reasons. First, there is often more than one neighboring spin S that is coupled to the observed spin I, leading to a much more complicated spectrum. Second, there is a severe linebroadening seen in NMR spectra of *homonuclear* dipolar-coupled spin systems with more than two spins involved. Quantum mechanically this is explained by the fact that term A and B do not commute, i.e. they have no common eigenfunctions and thus no eigensolution can be found for the dipolar Hamiltonian $\widehat{H}_{dd}$. Instead, the possible states of the system are linear combinations of Zeeman functions (functions found for the absence of dipolar coupling) that are a function of time, evolving under the influence of the dipolar coupling.

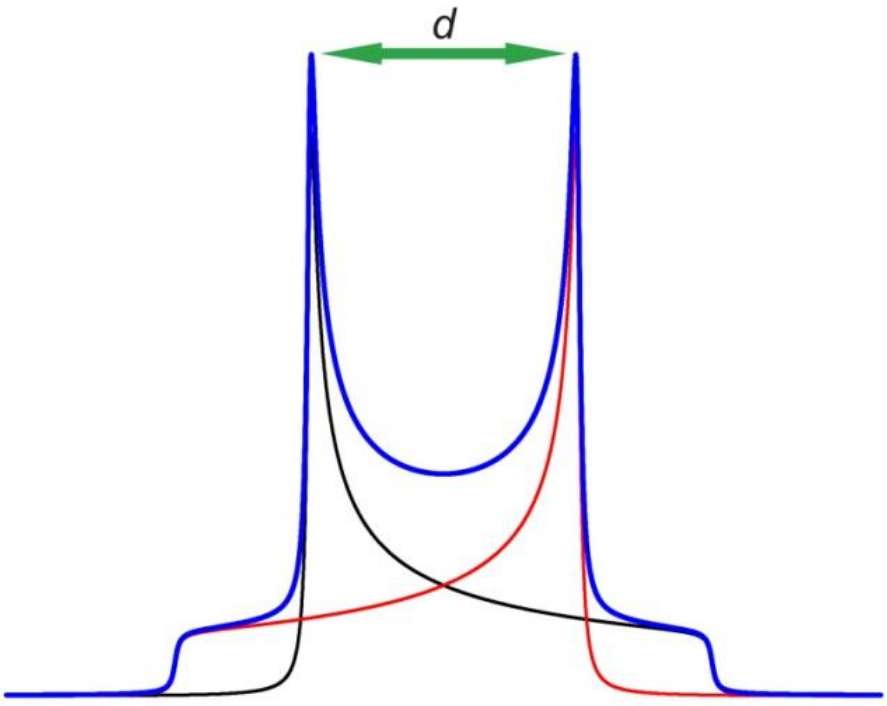

Figure 2.2: Calculated powder line shape for a spin-1/2 nucleus coupled to another spin-1/2 nucleus with well separated Larmor frequency (heteronuclear case). Both transitions (plotted in red and black respectively) sum up to a so called dipolar Pake pattern. The frequency separation of both 'horns' is equal to the dipolar coupling constant d. The 'horns' are formed by $I-S$ spin pairs with the internuclear vector being perpendicular to the external magnetic field. Reference is taken from ref. [16].

The effect on a transition in a multispin system is shown in Figure 2.3. The resonance line is broadened, rendering the observation of a dipolar Pake pattern impossible.

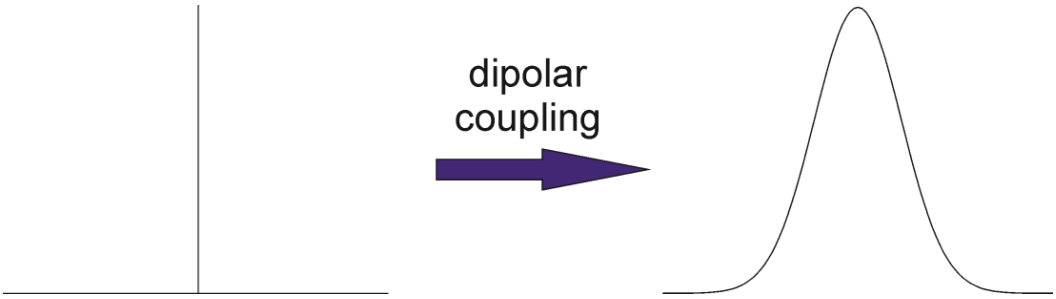

Figure 2.3: Schematic description of the effect of homonuclear dipolar broadening on the resonance. The broadening is due to the time-dependence of the wave function of the spin. Figure is adapted from ref. [7].

2.1.5 Quadrupolar Coupling

In addition to the magnetic dipole moment, the quadrupole Hamiltonian $\hat{H}_Q$ has to be considered for all nuclei possessing an electric quadrupole moment. It affects all nuclei with a spin larger than 1/2. As important nuclei like ^{1}H, ^{13}C, ^{29}Si and ^{31}P are spin 1/2, it may seem that only a minority of nuclei is quadrupolar. However, for around 75% of all isotopes $I > 1/2$ and in most cases, the quadrupolar interaction dominates the NMR spectrum. Physically explained, the origin of this interaction lies in a non-spherical charge distribution within the nucleus. Thus, the energy of the nucleus depends on the relative orientation of this distribution (specified by the term *electric quadrupole moment*) with respect to the gradient of an electric field. The quantization axis is defined by $\mathbf{B_0}$, even though the applied magnetic field does not interact with the electric quadrupole moment. However, the orientation of the electric quadrupole moment is non-trivially connected to the magnetic dipole, as they belong to the same nucleus. In other words, $\mathbf{B_0}$ interacts with the electric quadrupole moment through the magnetic dipole as mediator.

The following mathematical Equations base on the assumptions, that the Zeeman interaction $\hat{H}_Z = -\gamma\hbar\hat{\mathbf{I}} \cdot \mathbf{B}_0$ is larger than the quadrupolar interaction $\hat{H}_Q$. Only in this case, $\mathbf{B_0}$ serves as quantization axis and the quadrupolar interaction can be treated as perturbation. It should be noted that if the interaction of the nucleus with the applied field is of similar order of magnitude compared to the interaction with a local field gradient, perturbation theory breaks down.[1]

[1] If $\hat{H}_Q \gg \hat{H}_Z$, the quantization axis is determined by the orientation of the electric field gradient and the related spectroscopy technique is termed *nuclear quadrupole resonance* (NQR).

To be specific, the strength of the interaction depends on the isotope dependent quadrupole moment eQ that is constant and known for a given nuclear species. It is closely related to the quadrupole coupling constant χ according to

$$\chi = \frac{e^2 q_{zz}^{\mathrm{PAF}} Q}{\hbar} \tag{2.33}$$

where q_{zz}^{PAF} is a principal value of the *electric field gradient tensor* $e\mathbf{q}$, expressed in its principal axis frame. q_{zz}^{PAF} describes the gradient of the z-component of the electric field in direction z and in contrast to eQ, it depends on the local environment of the nucleus. Indeed, it is very sensitive to the local symmetry and short-range structure of the nucleus, as well as to dynamics. Hence, it provides a multitude of information that can be exploited by suitable NMR experiments. The higher the symmetry of the environment, the smaller the electric field gradient. For example, for cubic symmetry the electric field gradient vanishes and there is no quadrupolar interaction.

The quadrupole moment eQ and the electric field gradient tensor $e\mathbf{q}$ are connected by (cf. Equations (2.20) and (2.10))

$$\hat{H}_Q = \frac{eQ}{6I(2I-1)\hbar} \hat{\mathbf{I}} \cdot e\mathbf{q} \cdot \hat{\mathbf{I}} \tag{2.34}$$

With θ as the angle between the principal z axis of $e\mathbf{q}$ and the direction of the applied field $\mathbf{B_0}$ one obtains

$$\hat{H}_Q = \frac{3\chi}{8I(2I-1)} \left(3\cos^2\theta - 1 + \frac{1}{2}\eta_Q \sin^2\theta \cos 2\phi\right) \left(3\hat{I}_z^2 - \hat{I}^2\right) \tag{2.35}$$

ϕ is an additional polar angle in order to exactly define the orientation of $e\mathbf{q}$ in the case of non-axial symmetry. The asymmetry parameter η_Q is defined as

$$\eta_Q = \frac{q_{xx}^{\mathrm{PAF}} - q_{yy}^{\mathrm{PAF}}}{q_{zz}^{\mathrm{PAF}}} \tag{2.36}$$

In general, the tensor $e\mathbf{q}$ is non-axial (i.e. $q_{xx}^{\mathrm{PAF}} \neq q_{yy}^{\mathrm{PAF}} \neq q_{zz}^{\mathrm{PAF}}$).

In this thesis, the quadrupolar nucleus ^{2}H plays an important role (cf. chapter 6.6 and 12.5). It is a spin 1 nucleus with axial symmetry in organic compounds (because the C-D bond is axially symmetric). This is equivalent to $q_{xx}^{\mathrm{PAF}} = q_{yy}^{\mathrm{PAF}} \neq q_{zz}^{\mathrm{PAF}}$ and simplifies the expression for $\hat{H}_Q$ in Equation (2.35), where $\left(3\cos^2\theta - 1 + \frac{1}{2}\eta \sin^2\theta \cos 2\phi\right)$ is reduced to $(3\cos^2\theta - 1)$.

The transition frequency for ^{2}H is found to be

$$\omega_Q = \omega_0 - \frac{3}{8}\left(\frac{2m-1}{I(2I-1)}\right)\chi\left(3\cos^2\theta - 1 - \frac{1}{2}\eta\sin^2\theta\cos 2\phi\right) \qquad (2.37)$$

where $\delta = 3e^2qQ/8\hbar = 3\chi/8$. For $m = 1/2$, $(2m-1)$ is zero, resulting in $\omega_Q = \omega_0$ for spin 1/2 nuclei. As can be seen from Equation (2.37), the Zeeman energy levels $-m$ and $+m$ are shifted by the same frequency, thus the transition frequency $m: +1 \rightarrow -1$ does not change. However, according to the quantum mechanical rule $\Delta m = \pm 1$, this transition is forbidden.

For ^{2}H ($I = 1, \eta = 0$ and $m = 0, -1$) one obtains

$$\omega_Q = \omega_0 \pm \delta(3\cos^2\theta - 1) \qquad (2.38)$$

According to a general rule, there are $2I$ transitions that must be considered. Hence, there are two transitions for ^{2}H. Comparing Equation (2.38) with Equation (2.32), it is obvious that a Pake pattern similar to Figure 2.2 is obtained for ^{2}H nuclei with axially symmetric $e\mathbf{q}$. One important difference is, that the splitting of the 'horns' is not equal to the dipolar coupling constant d, but equal to $3/4\chi$.

In Figure 2.4, a powder line shape for $I = 1$ and $\eta \neq 0$ is shown. The spectrum strongly deviates from the typical Pake pattern. It is important to mention that even though $\eta = 0$ for C-D bonds, molecular motion may lead to an electric field gradient tensor with averaged principal components $\bar{q}_{xx}^{\mathrm{PAF}}$, $\bar{q}_{yy}^{\mathrm{PAF}}$ and $\bar{q}_{zz}^{\mathrm{PAF}}$. Here, $\bar{\eta} \neq 0$ is possible and hence, ^{2}H NMR spectra as seen in Figure 2.4 may be observed for deuterons.

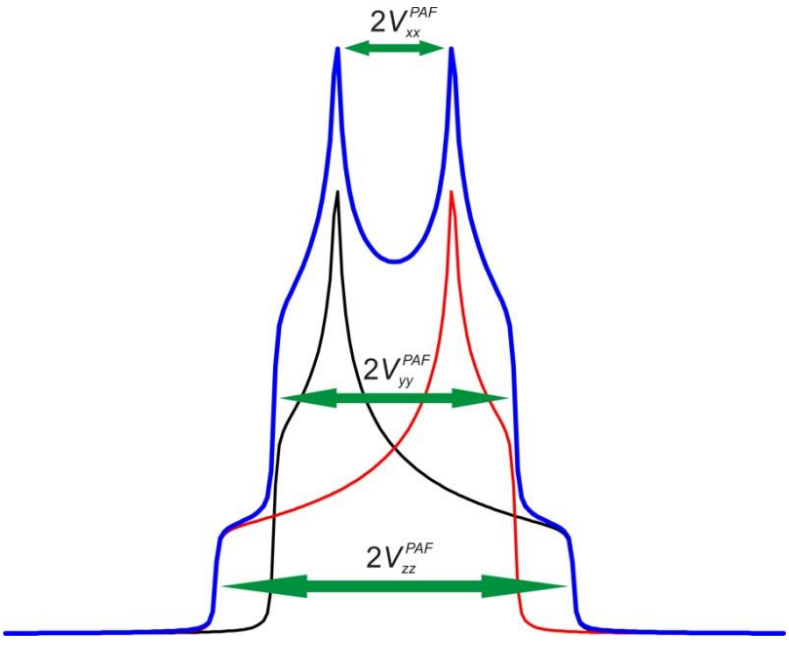

Figure 2.4: Calculated powder spectrum for $I = 1$ and $\eta \neq 0$. Notably, $eq_{\alpha\alpha}^{\mathrm{PAF}} = V_{\alpha\alpha}^{\mathrm{PAF}}$ with $\alpha = x, y, z$. The red and black subspectra arise from $m: +1 \rightarrow 0$ and $0 \rightarrow -1$ transitions. The overall spectrum is shown in blue. Figure is taken from ref. [16].

The size of the quadrupolar interaction has serious implications for NMR experiments, especially for nuclei with large quadrupole moments at sites of low symmetry (i.e. large electric field gradient). Radiofrequency pulses have frequencies around 100 kHz, corresponding to a $\pi/2$ pulse length of 2.5 µs. Even for ^{2}H nuclei with comparable small quadrupole moments (χ ≈ 165 kHz for C-D bonds), this frequency is not high enough to achieve uniform excitation of powder spectra, resulting in line shape distortions. For nuclei with quadrupole coupling constants in the range of several MHz, a second complication arises. The radiofrequency pulse interacts with the quadrupolar pattern, preventing a trivial nutation response of the resonance. One way to tackle this problem is the application of short pulses, i.e. pulse durations corresponding to $< \pi/2$. This circumvents hardware limitations that do not allow unrestricted high pulse power ('hard' pulses).

After a NMR excitation pulse, the dissipation of the pulse power requires some time in the order of µs for conventional pulses. This 'ring-down' prevents an immediate acquisition of the signal intensity after the last radiofrequency pulse. Thus, acquisition can start only after some 'dead time' and the beginning of the free induction decay (FID) is lost. Assuming that the phase of the signal is 0, i.e. maximal at the start of the FID, the signal is given by

$$S(t) = S_x(t) + iS_y(t) = S_0 e^{i\omega t} \tag{2.39}$$

Taking into account that the transverse magnetization decays over time, Equation (2.39) is modified to

$$S(t) = S_0 e^{i\omega t} e^{-\frac{t}{T_2}} \tag{2.40}$$

The decay is represented by an exponential decay with a time constant T_2, the spin-spin relaxation time. It can be shown that the line shape of an ideal resonance is Lorentzian and the full width at half maximum Δν is calculated according to

$$\Delta\nu = 1/(T_2\,\pi) \tag{2.41}$$

Even though a Pake pattern (cf. Figure 2.2) is not Lorentzian in shape, Equation (2.41) allows the estimation of T_2 for the signal intensity of a typical ^{2}H line shape ($\Delta\nu$ in the order of roughly 50 kHz) to be around 6 µs. The period even state of the art hardware needs to wait before signal acquisitation can start is at least 5 µs after the last pulse. Thus, a substantial amount of signal intensity would be lost in a conventional single-pulse experiment. This is not only an issue of sensitivity, but especially of line shape distortions (see Figure 2.5).

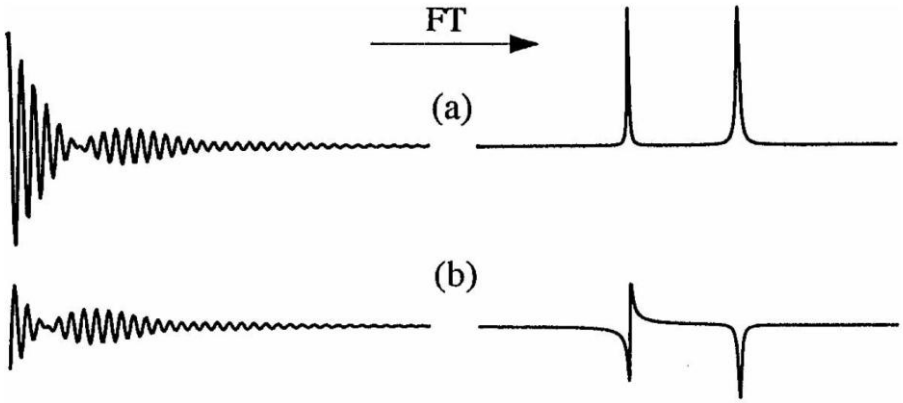

Figure 2.5: Spectral effects of a dead time at the beginning of the time signal. a) Reference spectrum with immediate acquisition and b) with dead time before acquisition. Figure is taken from ref. [11.]

Experimentally, this is circumvented by the *quadrupole echo sequence* where a spin echo is generated by two $\pi/2$ pulses, with the excitation pulse being separated more than the dead time from the refocusing pulse (Figure 2.6). Notably, any interaction *bilinear* in the observed spin operator, including homonuclear dipolar coupling, is refocused by this pulse sequence. In contrast, the *Hahn-echo* refocuses any interactions *linear* in the observed spin operators. It is obtained by applying a π pulse as refocusing pulse instead of a $\pi/2$ pulse. Chemical shift anisotropy and heteronuclear dipole-dipole coupling are bilinear interactions.

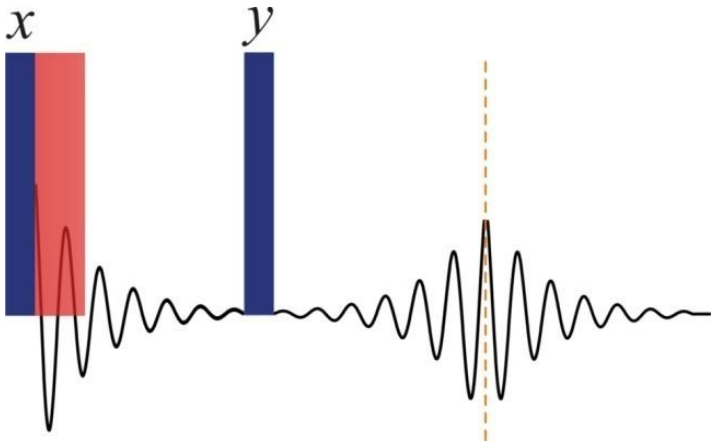

Figure 2.6: Quadrupole echo sequence used for recording broad quadrupolar powder patterns. $\pi/2$ pulses are shown in blue. Acquisition starts at the maximum height of the echo intensity (dashed line). The portion of the FID that would have been lost with a conventional single pulse experiment is marked in red. Figure taken from ref. [16].

The spectrum obtained by the quadrupole echo sequence is not necessarily identical to a hypothetic spectrum obtained by single pulse acquisition without dead time. If molecular motion in the range of the width of the powder spectrum is present in the respective part of the sample, the line shape is depending on the interpulse delay τ. This regime is called the

intermediate exchange region and renders deuterons a valuable spin probe. For computational models, it is often assumed that the deuterons in the sample jump between different, distinct sites whose spatial arrangement is model dependent. The time needed for such a jump is assumed to be zero, i.e. neglectable compared to the dwell time between two jumps. The rate and possible geometries of underlying motions may be extracted via matching of experimentally observed spectral line shapes with computed line shapes that result from a given model. As mentioned above, deuteron powder patterns span several kHz which is in the range of the (jump) frequency Ω of typical motions in organic compounds (at experimentally accessible temperatures). The reason for the τ-dependence of the powder line shape is that the signal intensity contribution of deuteron sites to the overall spectrum intensity is depending on their respective jump frequency. For static deuterons (rigid limit) and for deuterons jumping extremely fast (fast limit), the intensity contribution is equal. However, for deuterons in the intermediate exchange region, the intensity is reduced as specified by the reduction factor $R(\Omega)$:

$$R(\Omega) = \frac{I_\Omega}{I_{\mathrm{rfl}}} \tag{2.42}$$

Where I_Ω is the intensity of a deuteron with jump frequency Ω in the intermediate exchange region and I_{rfl} is the intensity of a deuteron in the rigid or fast limit.

Especially in ill-defined samples such as polymers, the molecular motion has to be described by a distribution of jump rates $P(\Omega)$. In order to calculate the signal intensity contribution of deuterons with specific Ω to the observed spectrum, it is necessary to weight the respective subsprectrum $j(\omega, \tau, \Omega)$ with $R(\Omega)$ and $P(\Omega)$. Subsequently, properly weighted subspectra correspond to the experimentally observed spectrum $J(\omega, \tau)$:

$$J(\omega, \tau) = \int_{-\infty}^{+\infty} j(\omega, \tau, \Omega) R(\Omega)\, P(\Omega)\, d\Omega \tag{2.43}$$

Notably, the *mean reduction factor* $\bar{R}$ is defined as

$$\bar{R} = \frac{\int_{-\infty}^{+\infty} P(\Omega) R(\Omega) d\Omega}{\int_{-\infty}^{+\infty} P(\Omega) d\Omega} \tag{2.44}$$

2.2 Mechanical Measurements

2.2.1 Tensile tests

In a stress-strain test a sample is subjected to uniaxial tension until failure. The stress σ is measured continuously as the specimen is being deformed at a constant rate. Since the response of a polymer to external forces is time dependent, the shape of the observed curve will depend on the strain rate and temperature.[17] As can be seen from Figure 2.7, the stress-strain behavior of polymers strongly depends on the class of polymer. From such a test, a variety of properties can be determined. However, the experimental raw data are reported as force-deformation curves. In order to obtain stress-strain curves, the transformation of scales is obtained with

$$\sigma = \frac{F}{A} \qquad \varepsilon = \frac{l - l_o}{l_o} \tag{2.45}$$

where A and F are the cross-sectional area and force respectively. l_o is the initial length before the deformation. Notably, a variety of definitions exists for the strain ε, but for very small deformations they are equivalent to the definition given in Equation (2.45). For example, the *true strain* (Hencky strain, natural strain) is defined as

$$\varepsilon_l = \ln\left(\frac{l}{l_o}\right) = \approx \underbrace{\frac{l - l_o}{l_o}}_{\varepsilon} - \left(\frac{l - l_o}{l_o}\right)^2/2 + \left(\frac{l - l_o}{l_o}\right)^3/3 - \cdots \tag{2.46}$$

where it is taken into account that the length of the sample changes during deformation. Note that the first term of this series expansion is equal to the definition of ε given in Equation (2.45).

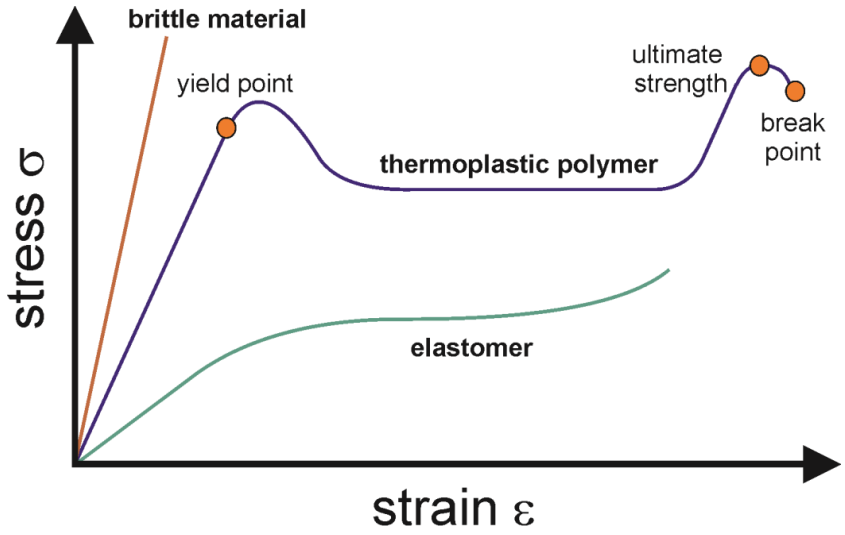

Figure 2.7: General types of stress-strain curves. Figure adapted from ref. [16]. Brittle materials, e.g. highly cross-linked epoxies, have high E-modulus and low elongation at break.

The *elastic modulus* E of the material is equal to the slope of the initial straight-line portion of the curve. In other words, E is the proportionality constant between the stress σ and the strain ε.

$$\sigma = E\varepsilon \tag{2.47}$$

Once the stress exceeds the *elastic limit* or yield point, the deformation will be permanent, i.e. non-reversible. The *tensile strength* or ultimate strength is the maximum stress that a material can withstand while being stretched before it breaks. To a first approximation, the tensile strength does not depend on the size of the test specimen (cf. Equation (2.45)).

The *Poisson's ratio* ν determines if the volume of the sample remains constant while being stretched. It is defined as

$$\nu = -\left(\frac{t-t_0}{t_0} \Big/ \frac{l-l_o}{l_o}\right) = -\left(\varepsilon_T \Big/ \varepsilon\right) \tag{2.48}$$

where t_0 is the original thickness of the specimen and t is its actual thickness after deformation. ε_T is the strain in the transverse direction, i.e. perpendicular to the applied force. If $\nu = 0.5$, the volume of the specimen remains constant while being stretched. This is the case for ideal, elastic rubbers. If plastic deformation occurs, the volume usually changes. In general, there is an increase in volume ΔV according to (first-order approximation for small values of ε_T and ε):

$$\Delta V \Big/ V_0 = (1 - 2\nu)\varepsilon \tag{2.49}$$

Toughness may be defined in several ways, one of which is in terms of the area under a stress-strain curve.[17] This procedure yields an indication of the ability of a material to absorb energy without fracturing. It is important to distinguish (tensile) strength from toughness. Both are not necessarily connected with each other, as can be seen from Figure 2.8. A polymer with high E-modulus may have a high tensile stress, but the area under the stress-strain curve may be small compared to a polymer with lower E-modulus but higher strain. Toughness is an important parameter as it is closely related to the significant parameter impact resistance. Strong polymers with low toughness are usually brittle and exhibit a low impact resistance. Cross-linked, non-modified epoxies belong to this class of polymers.

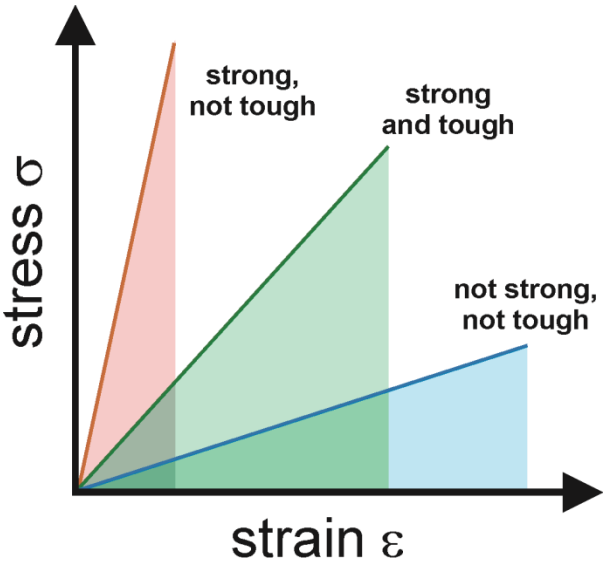

Figure 2.8: Schematic relationship between strength, toughness and strain. The area under the curves is a measure of the toughness of the respective polymer.

2.2.2 Dynamic Mechanical Analysis

In contrast to tensile tests, the applied stress in dynamic mechanical tests is periodic. Often, a sinusoidal stress is applied and the response of the material is measured. Generally, stress and strain are not in phase. There are many experimental setups to conduct a dynamic mechanical analysis (DMA), but they all have in common that the deformation of the sample material is relatively small. This kind of experiment is usually more sensitive to the chemical structure and morphology than a tensile test and especially suitable for studying glass and secondary transitions.

The following mathematical derivation is illustrated in terms of *shear modulus* G, but analogous notation holds for other experimental setups.[18] G is defined as the ratio of *shear stress* τ to *shear strain* γ:

$$\tau = \frac{F}{A} \qquad \gamma = \tan\theta \qquad \tau = G\gamma \tag{2.50}$$

where A is the area on which the force acts. For the definition of θ, see Figure 2.9 where the deformation of a solid experiencing a force parallel to one of its surfaces (while the opposite face is fixed) is shown. The angle θ is connected to the shear strain which in turn is proportional to the shear stress.

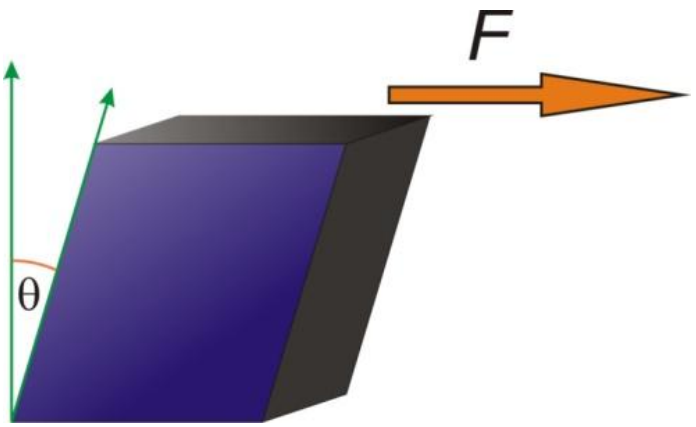

Figure 2.9: For small deformations, $\tan\theta$ is proportional to F/A. A is the surface area on which the force acts. Figure is taken from reference [16].

For a purely elastic material, i.e.

$$\frac{\mathrm{d}\tau}{\mathrm{d}t} = G' \frac{\mathrm{d}\gamma}{\mathrm{d}t} \tag{2.51}$$

the applied shear amplitude is maximal if the shear stress is maximal.

$$\tau(t) = G' \underbrace{\gamma_\mathrm{o} \sin(\omega t)}_{\gamma(t)} \tag{2.52}$$

However, polymers are generally viscoelastic. The viscous component can be described according to

$$\tau = \eta_S \frac{\mathrm{d}\gamma}{\mathrm{d}t} \tag{2.53}$$

where η_S is the shear viscosity. Importantly, in Equation (2.53) the stress is proportional to the strain rate (Newton's law), but in purely elastic materials it is the stress rate that is proportional to the strain rate (cf. Equation (2.51)). Using Equation (2.53) and $\gamma(t) = \gamma_\mathrm{o} \sin(\omega t)$, it follows

$$\tau(t) = \eta_S \, \gamma_\mathrm{o} \omega \cos(\omega t) \tag{2.54}$$

Obviously, for a purely viscous material, shear stress and shear strain are phase-shifted by 90°.

For polymer systems, the observed phase shift will be found between both extremes. Assuming that shear stress is a linear combination of both extremes it follows

$$\tau(t) = G' \gamma_\mathrm{o} \sin(\omega t) + \eta_S \, \gamma_\mathrm{o} \omega \cos(\omega t) = \gamma_\mathrm{o} |G^*| \sin(\omega t + \delta) \tag{2.55}$$

where

$$|G^*| = \sqrt{G'^2 + (\omega \, \eta_S)^2} = \sqrt{G^2 + G''^2} \tag{2.56}$$

δ is the phase shift between stress and strain. It can be shown that

$$\tan\delta = \frac{\sin\delta}{\cos\delta} = \frac{\frac{\tau_0}{\gamma_0}\sin\delta}{\frac{\tau_0}{\gamma_0}\cos\delta} = \frac{\omega \, \eta_S}{G'} = \frac{G''}{G'} \tag{2.57}$$

$|G^*|$ is the complex shear modulus, with G' as real part. As it is the elastic shear modulus (see Equation (2.51)), it is termed *storage modulus.* Accordingly, G'' is the *loss modulus* and reflects the energy dissipation term. The loss modulus G'' is directly proportional to the heat H dissipated per cycle as given by[17]

$$H = \pi G'' \gamma_0^2 \tag{2.58}$$

3 Literature

[1] H.-G. Woo, H. Li, Springer, **2011**.

[2] H. W. Spiess, *Macromolecules (Washington, DC, U. S.)* **2010**, *43*, 5479.

[3] J. Brandrup, E. H. Immergut, E. A. Grulke, A. Abe, D. R. Bloch, *Polymer Handbook*, 4th ed., John Wiley & Sons, **2005**.

[4] K. Schmidt-Rohr, Q. Chen, *Nat. Mater.* **2008**, *7*, 75.

[5] M. Munowitz, *Coherence and NMR*, Wiley-Intersience, New York, **1988**.

[6] A. Abragam, *The Principles of Nuclear Magnetism*, Oxford University Press, Oxford, **1993**.

[7] M. J. Duer, *Introduction to Solid-State NMR Spectroscopy*, Blackwell Science Ltd, Oxford, **2004**.

[8] P. J. Hore, *NMR: The Toolkit*, Oxford University Press, Oxford, **1995**.

[9] M. H. Levitt, *Spin Dynamics: Basics of Nuclear Magnetic Resonance*, Wiley & Sons, Chichester, **2007**.

[10] R. R. Ernst, G. B., W. A., *Principles of Nuclear Magnetic Resonance in One and Two Dimensions* Oxford University Press, Oxford, **1990**.

[11] K. Schmidt-Rohr, H. W. Spiess, *Multidimensional Solid-State NMR and Polymers*, Academic Press Inc., London, **1994**.

[12] S. P. Brown, H. W. Spiess, *Chem Rev* **2001**, *101*, 4125.

[13] D. D. Laws, H.-M. L. Bitter, A. Jerschow, *Angew. Chem., Int. Ed.* **2002**, *41*, 3096.

[14] H. W. Spiess, *J. Polym. Sci., Part A: Polym. Chem.* **2004**, *42*, 5031.

[15] C. M. Widdifield, R. W. Schurko, *Concepts Magn. Reson., Part A* **2009**, *34A*, 91.

[16] C. Kins, diploma thesis thesis, MPIP (Mainz), **2009**.

[17] L. E. Nielsen, R. F. Landel, *Mechanical Properties of Polymers and Composites*, CRC Press, **1994**.

[18] B. Tieke, *Makromolekulare Chemie: Eine Einführung*, Wiley-VCH Verlag GmbH & Co. KGaA, **1997**.

PART I

New Phosphonate Based Additives for Fortification in a Model Epoxy

4 Introduction

4.1 Strategies for Tuning Epoxy Properties

4.1.1 Mechanical Properties of Polymers[1-3]

In recent decades, polymers have become a class of materials that is as important as metals and other long-established substances. They exhibit versatile mechanical properties and find widespread use in both special and large-volume applications where typically relatively cheap raw materials are appreciated. The mechanical properties of polymers are governed by a complex interplay of molecular factors on the atomic scale (e.g. chemical structure, molecular weight, cross link density) and structural factors (e.g. phase separation, orientation, crystallinity) on the nano- to micrometer scale.

Polymer materials have to retain their features for a long time and it is crucial to exclude mechanical failure. This is a non-trivial undertaking as a multitude of environmental conditions and stresses have to be considered, including deformation through pressure and shear (amplitude and frequency dependent), moisture, heat, etc. The complexity is mainly due to the viscoelasticity of macromolecular systems. Viscous materials dissipate energy as heat that is lost, whereas in purely elastic polymers it is stored as potential energy. For example, rubbers (elastomers) are very elastic, but thermoplastic materials are highly viscous. Further research is necessary to develop a theoretical and experimental framework in order to plan and adapt concepts for fabricating high-performance polymers that suit certain purposes.

4.1.2 Monomers and Additives[4, 5]

Epoxies are typically synthesized from at least two components: the *resin* and the *hardener*. The resin comprises a monomer bearing at least two epoxide groups, while common hardeners are polyamines, polyanhydrides or polycarboxylic acids that are sufficiently nucleophilic to allow for ring-opening of the epoxy group. Notably, a variety of commercially available monomers facilitates the synthesis of polymers with a broad range of properties. Hence, epoxies have found tremendous application in industry.[6]

Typical characteristics include relatively high reactivity at room temperature and no need for removal of low-molecular weight reaction products. Small reaction shrinkage results in good adhesion to construction material. The chemical resistance towards chemicals is high and a

variety of commercially available monomers allows for control over the reaction process (e.g. viscosity and pot life).

Two main strategies have been developed in recent years to selectively tailor the properties of epoxies. One is to tune thermal and mechanical characteristics by proper choice of *monomers* as well as the application of *additives*.[7] The second major strategy to tailor properties is the incorporation of *fillers* into the polymer matrix.[8, 9] These materials comprise a variety of potential materials: Fibers[10] (e.g. carbon nanotubes), rubbers[11] (e.g. functionalized butadiene) and minerals[12, 13] (e.g. silicates, alumina, calcium carbonate) and have been investigated extensively due to their ability to improve toughness and fatigue properties.

Monomers

The industrially most important epoxy monomers are based on bisphenol A diglycidyl ether, that is prepared from bisphenol A and epichlorohydrin in the presence of alkali hydroxide. If the ratio of epichlorohydrin and bisphenol A is less than 2 to 1, solid and low-melting oligomeric epoxies are obtained, corresponding to $n > 1$ in Scheme 4.1a. Typically, n ranges from 0 to 25 in most commercial products.

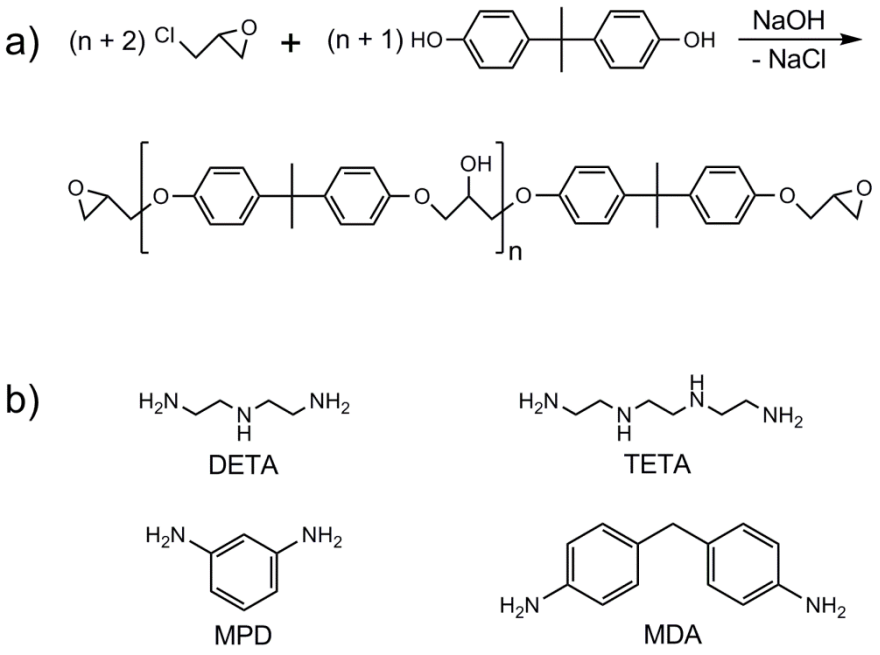

Scheme 4.1: a) Oligomeric diglycidyl ether of bisphenol A. The number of repeat units depends on the stoichiometry of the synthesis reaction. b) Typical aliphatic and aromatic amine hardeners. Aromatic amines cure more slowly than aliphatic amines (i.e. increased pot life) due to their weaker nucleophilicity and need elevated temperatures for cure.

Halogenated derivatives like tetrabromobisphenol A diglycidyl ether find application in flame-retardant epoxies but due to environmental concerns, it is necessary to find suitable replacements.

Novolac glycidyl ethers are the second, industrially important group of epoxy resins. The term novolac describes complex mixtures obtained by the reaction of phenol with formaldehyde under acidic conditions. Epichlorohydrin reacts with novolac to form hydrochloric acid and highly functionalized oligomers. Such monomers often provide increased chemical resistance compared to other bisphenol A epoxies.

Polyamines have the highest reactivity of all hardeners and can be divided in aliphatic and aromatic polyamines. The vast majority of amine hardeners comprises more than two active hydrogen atoms per molecule, so that cured epoxies are cross-linked polymers. Aliphatic polyamines are conveniently mixed with the epoxy monomer due to their low viscosity at room temperature. As they are generally low-molecular weight compounds, they have to be weighed accurately to assure the proper amine/ epoxy ratio before mixing with the resin. Important examples are diethylenetriamine (DETA) and triethylenetetramine (TETA). Tertiary aliphatic amines may act as room temperature hardeners initiating a strong exothermic cure that is accompanied by a high polymerization rate. Predominantly, they are used in catalytic amounts as accelerators in conjunction with polysulfides and anhydrides to quicken the cure process. As aliphatic amines are skin irritating and should be handled with care, oligomeric polyamine resin adducts have been developed, that are less volatile, less toxic and their reaction with epoxy rings is less exothermic. Moreover, their relatively high molecular weight tolerates larger weighing errors. Synthesis is conducted by adding an excessive amount of polyamine to an epoxy resin so that all epoxy groups are consumed and only amino functionalities are left. These oligomeric precursors can be isolated and stored before they are conveniently polymerized with any epoxy resin component to form the final polymer network.

In comparison, epoxies derived from aromatic polymers (e.g. *m*-phenylenediamine (MPD), 4,4'-methylenedianiline (MDA)) exhibit an enhanced thermal stability and higher stability towards chemicals. However, they are solid in the pure state and have to be dissolved in the epoxy resin in the heat before slow hardening occurs. At room temperature, the cure process stops at the so called *B-stage*. This is an intermediate stage in the reaction process in which the obtained material softens when heated and swells when in contact with certain

liquids. It consists primarily of linear polymer chains due to the large difference in reactivity of primary and secondary aromatic amines.

For the sake of completeness, the latent curing agents should be mentioned. This group comprises small molecules or salts that can be mixed and stably stored with epoxy resins at room temperature and polymerization does not start before treatment with UV light, heat, pressure etc.

Additives

The bulk properties of polymers are often adjusted via addition of a complex blend of compounds collectively known as additives. In this section, only a brief overview is given about additives used to manipulate mechanical properties of epoxies.

In case the viscosity of the monomer mixture is too high for appropriate processibility, air bubbles may remain in the solid epoxy. One way to tackle this problem is the addition of a degasser additive. Alternatively, *plasticizer* (e.g. dibutyl phtalate) can be added prior to cure. Notably, this is only an option if detrimental effects on the glass transition temperature or health issues, such as leaching into the environment, are not an issue. In this regard, *reactive diluters* are a better choice. They are low-viscosity epoxy resins, such as 1,4-butanediol diglycidyl ether, that are added along with conventional epoxy resins. In part, they are monofunctional, i.e. contain only one epoxy group, and act as polymer chain end. Of course, the amount of hardener has to be adjusted according to the amount of reactive diluter added. As they are covalently bound to the hardener during cure, leaching is not possible.

For some applications, the major drawback of epoxies is their brittle nature. *Flexibilizers* are additives with a flexible backbone, such as polysulfides or polypropyleneglycol diglycidyl ether that prevent, to some extent, embrittlement of the epoxy. Similar to reactive diluters, they are covalently bound to the polymer backbone during cure and typically do not leach.

4.1.3 Fillers

The incorporation of *fillers* into the polymer matrix is often accompanied by detrimental effects on other properties, especially stiffness and yield strength. The primary benefit of inorganic fillers is that both toughness and modulus can be enhanced if certain conditions are fulfilled.[14, 15] Additionally, they are usually low cost materials. They overcome the major deficiencies of epoxies (intrinsic brittleness and lacking damage tolerance) especially when the cross-link density is high. Important parameters for tailoring toughening agents are

- Modulus of the particle
- Size and volume fraction of the fillers (typically nm to µm scale)
- Surface modification (influences dispersion, matrix-particle adhesion)
- Mean distance between neighboring particles
- Aspect ratio of non-isotropic fillers

Nevertheless, a drawback of the filler approach is the processing limit as the viscosity of the monomer mixture increases upon addition of rigid reinforcements. This can be circumvented by using a different approach: Crystallizable solvents may form a homogeneous solution of low viscosity at the processing temperature, but potentially undergo phase separation and subsequent crystallization upon cooling. These crystals may even be visible to the eye and potentially exhibit a variety of morphologies that provide toughening and modulus enhancement.[16, 17]

The failure mechanisms in polymer matrix composites are manifold and complex. Important energy absorbing mechanisms are

- Crazing: formation of microcracks that are held together by polymer fibrils
- Shear yielding: localized plastic flow developing during severe deformation
- Crack deflection: tilting of the propagating crack around the second phase particles
- Crack pinning: bowing of the crack front in between the particles leads to an increased crack tip front
- Debonding: local detaching of the filler surface from the polymer matrix

In summary, the properties of modified epoxies are a result of a complex interplay of a multitude of factors. Moreover, the aforementioned mechanisms vary for a given system with experimental conditions (temperature, test method, age etc.). In practice, after the desired characteristics for a specific system are defined, a tailored modification strategy has to be developed by combining experience and trial and error.

4.1.4 Molecular Fortification

Jackson and Caldwell were among the first to conduct comprehensive studies on a new class of additives: antiplasticizer.[18-20] They were searching for plasticizers to increase both the flexibility and toughness in bisphenol polycarbonate.[21] However, many test compounds revealed increased tensile modulus and tensile strength while at the same time the glass

transition temperature of the polymers was reduced. Initial observations led to the conclusion that these additives are required to contain polar functionalities and should be thin, rigid, aromatic molecules in order to promote dipolar interactions with the polymer backbone. Later, a multitude of different polymer-antiplasticizer systems was discovered, including epoxies.[22-27] Non-reactive and non-charged additives have been used, suggesting that an interplay of *non-covalent* and *non-electrostatic* interactions on a molecular length scale among fortifier and polymer backbone mediated fortification. Therefore, antiplasticizers were also termed molecular fortifiers[28] and successfully applied to antiplasticize poly(vinyl chloride),[29] poly(phenylene ether)[30] and poly(styrene)[31] respectively, including meta-terphenyl as antiplasticizer for poly(carbonate),[32]. These are all unpolar compounds and disproved the theory that polar interactions are essential. Despite manifold applications, no commonly valid mechanism of fortification could be established.[33, 34] A recent description of antiplasticization in terms of an explicit molecular model supposes smaller-scale collective motions of the system upon antiplasticizer addition.[35] Note that the term antiplasticizer is commonly used to describe non-reactive low molecular weight diluents where the fortifier molecule is assumed to be uniformly distributed within the polymer matrix, distinguishing it from the crystallizable solvents.

In all cases, characteristic features upon fortification could be observed. Above a system-dependent weight limit (critical concentration), antiplasticizers act as plasticizers. Furthermore, the density of the fortified system is higher than predicted by a simple rule of mixture and the magnitude of the (often high temperature part) secondary loss transition (i.e. β-transition) is reduced. It is anticipated that nanoscopic voids exist in neat polymers (termed *free volume*) that can possibly be occupied by fortifier molecules or other additives, thereby facilitating increased density of the additive-polymer mixture.

Such filling of free volume was supported by gas permeability experiments on various polymers.[36, 37] The depression of the β-transition is verified by dielectric and dynamic mechanical measurements.[23-25, 27, 32, 36, 38, 39] It is an intuitive notion that, by occupying free volume, the energy required to displace polymer chains increases. Hence, the antiplasticizer eliminates the flexibility of the polymer chain resulting from the low temperature mechanical loss transition.[36] Similar to the mechanism of antiplasticization, the relaxation phenomena related to the β- and α-transition have not been put in a self-consistent

theoretical frame yet. Some descriptions connect the α-transition with the glass transition; involving collective molecular movements of a large number of structural units. In contrast, the β-transition comprises local, restricted motions of small polymer segments at lower temperature. Nevertheless, the distinction is not sharp and still under debate.[40-46]

5 Motivation

In early attempts, it was observed that the small phosphonate compound, dimethyl methylphosphonate (DMMP),[†] increases both mechanical *and* thermal properties when used as an additive in a model epoxy network.[28, 38] This has been considered rather unusual since antiplasticizer, similar to plasticizers, decrease the glass transition. Though dimethyl sulfoxide (DMSO) is a structurally very similar to DMMP, it was found to *decrease* T_g for the same model epoxy network, while notably, mechanical properties were improved. Both molecules differ markedly in their impact on thermal properties but show similar effects on mechanical properties of the epoxy and closer inspection of dynamic mechanical measurement data revealed that DMSO additionally suppresses the β-relaxation of the epoxy whereas DMMP has no effect. These findings clearly demonstrate that DMSO acts in accordance with common expectations for antiplasticizers, thus emphasizing the particular role of DMMP. Tentatively, it was suggested that the polar P=O double bond forms hydrogen bonds with the hydroxyl functionalities located on the polymer chains, thereby increasing the apparent cross-link density.

For a variety of reasons, solid state NMR is a versatile and suitable method to investigate amorphous solids such as polymers below T_g.[47-49] This initiated a solid-state NMR study on the DMMP and DMSO fortified epoxy system described above that also formed the basis of my diploma thesis (see Scheme 5.1).[50] NMR is a nondestructive method that allows for the selective study of specifically labeled sites. In addition, molecular dynamics can be observed over many time scales by exploiting a range of mostly anisotropic interactions of the nuclear spins with their surroundings. Multidimensional NMR spectroscopy is able to correlate different nuclei in close proximity and enhances the spectral resolution, whereas the distance between dipolar coupled nuclei can be measured inter- and intramolecular. Importantly, in contrast to many scattering techniques, there is no need for crystalline order to probe nanoscale structures. In summary, DMSO and DMMP were selectively isotope labeled to investigate local order and to unequivocally assign chemical shifts. In addition, temperature dependent measurements of anisotropic spin interactions allowed for the determination of fortifier dynamics. A “free molecule”-type behavior of DMSO in DMSO-

[†] Phosphor based compounds have also found tremendous interest for their application as fire retardant additives in polymers

fortified epoxies similar to common inclusion compounds such as carceplexes was revealed, pointing towards mere filling of free volume by the additive.[51] In contrast, the likely presence of two different phosphonate species clearly suggested a complex mechanism of fortification in the case of DMMP. Importantly, the tentative idea of H-bonding as substantial contribution to the effect of fortification could be excluded for both fortifiers. Only very faint signal intensity arising from ^{31}P-^{31}P dipolar coupled spin pairs was detected, excluding significant clustering of DMMP inside the polymer matrix.[34, 52, 53]

Nevertheless, it was not possible to fully define the origin of fortification in the context of my diploma thesis. In particular, the shift of the ^{31}P resonance of DMMP to over 10 ppm lower values during cure could not be explained. Computational density functional theory (DFT) calculations demonstrated that such a large change in isotropic chemical shift cannot be solely explained by aromatic ring currents of neighboring bisphenol A moieties.

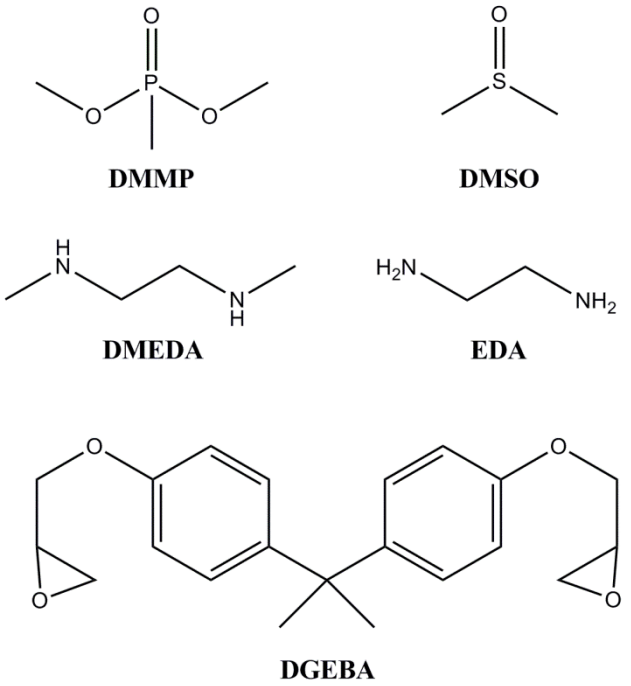

Scheme 5.1: Structures of fortifiers DMMP, DMSO and amine monomers dimethyl ethylenediamine (DMEDA) and ethylenediamine (EDA) as well as the epoxy resin bisphenol A diglycidyl ether (DGEBA).

6 Results and Discussion

6.1 Outline

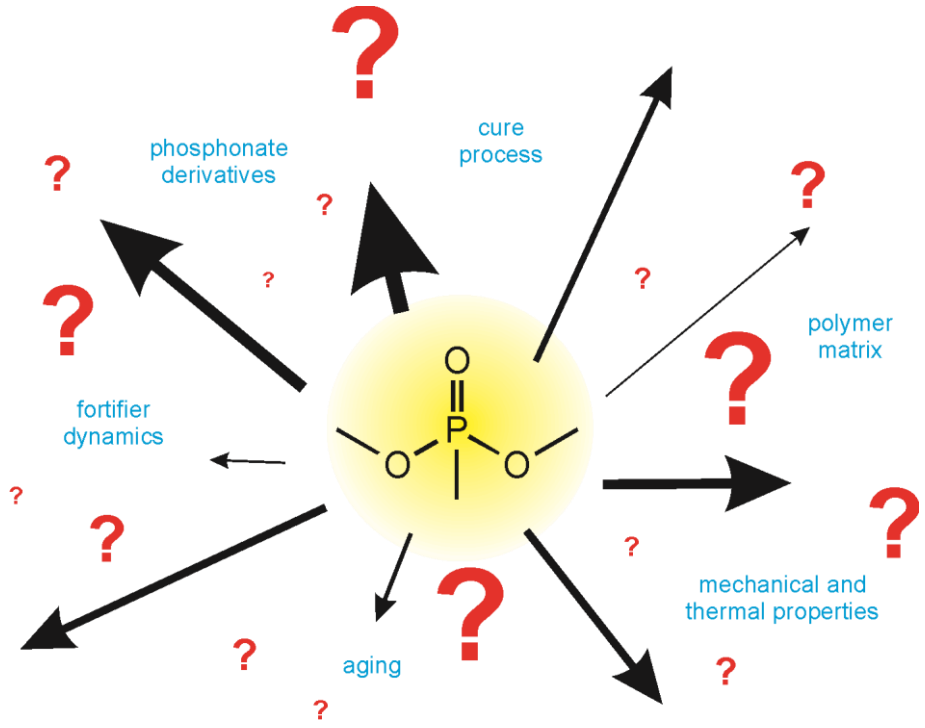

Figure 6.1: Various factors determine the overall performance of the resulting, fortified epoxy.

Phosphonates constitute the basis of a newly employed class of fortifiers, whose function is distinctly different from 'classic' fortifiers and literature data about the dealkylation reactivity with respect to amines is scarce. Hence, there had not been established a theoretical or experimental framework yet. Figure 6.1 illustrates the different directions that one can choose to put further effort into the characterization of these new materials. On the one hand, this offers a lot of freedom and exciting research. On the other hand, there are no guidelines for an established evaluation process of this new fortified system. From the data of DMMP fortified epoxy alone cannot be ascertained how

- phosphonates with different substituents influence the epoxy
- the cure process influences fortification
- thermal and mechanical characteristics are related to each other
- the epoxy's properties change with time
- the dynamics (mobility) of the additive depend on temperature

6.2 Reaction of Phosphonates

Dimethyl sulfate is a well-known methylating agent in organic synthesis. As its structure is similar to phosphonates (both are methyl esters), the literature was searched for similar applications of DMMP. Indeed, apart from its commercial use as flame retardant, DMMP can be used as mild methylating reagent.[54]

Aliphatic amine hardeners are known for their nucleophilicity (Scheme 5.1). In case DMMP is demethylated by EDA and DMEDA, there should be a period at the beginning of the cure when unreacted and reacted phosphonate are both present at the same time. Demethylation of DMMP yields methyl methylphosphonate that bears a negative charge. Hence, the electron density at the phosphorus atom is significantly increased, shifting the chemical shift to lower ppm values. Two distinct ^{31}P resonances should be observable by NMR. When the cure process of DMMP fortified epoxy is stopped after gelation (precure at 50°C for 3 h) the glass transition temperature is reduced to 70°C (fully cured: T_g = 99°C) and the corresponding $^{31}P\{^1H\}$ CP-MAS NMR spectrum (Figure 6.2) clearly displays two resonances at 22.7 and 33.1 ppm, with an intensity ratio of about 2:3. The signal at 22.7 ppm (MMP) is typically found for fully cured epoxies whereas the peak at 33.1 ppm is attributed to yet unreacted DMMP. This assignment is supported by the fact that the ^{31}P chemical shift of DMMP dissolved in DMSO-d_6 is very similar (34.0 ppm).

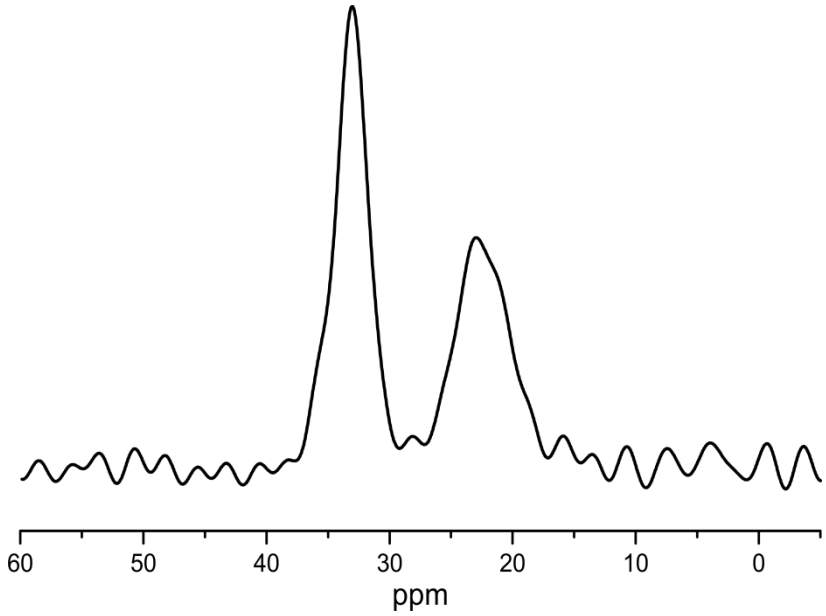

Figure 6.2: $^{31}P\{^1H\}$ CP-MAS spectrum of a precured (3 h at 50°C) DMMP fortified epoxy at 202.45 MHz and 25 kHz MAS using a Bruker DSX500 machine, a contact time of 250 µs coadding 256 transients; π/2-pulse length of 2.5 µs and a recycle delay of 5 s. The contact time was held short to ensure polarization transfer originating from the methyl group directly bound to phosphorus only. Under such conditions, the intensity of both resonances should be approximately proportional to the number of phosphorus spins. This leads to an estimated DMMP conversion of 40%.

Furthermore, a ^{31}P spectrum of epoxy fortified with methyl hydrogen methylphosphonate (MHMP), i.e. protonated MMP, shows a broad signal at around 22.7 ppm, thus indicating a similar phosphorus species compared to a DMMP fortified epoxy. Indeed, deprotonated MHMT and demethylated DMMP should have identical shifts as the chemical structure is identical (omitting different polymer environments that may play a role in the solid state). Notably, DMMP and DMSO fortified epoxies are transparent and appear to form a homogeneous phase (at least upon eye inspection); MHMP fortified epoxy does not. After addition of MHMP to the monomer mixture, a white, dispersed salt precipitates from the solution, preventing a uniform monomer distribution. Obviously, it is essential to avoid instantaneous salt formation. This illustrates that the phosphonate reactivity is a crucial parameter and apparently DMMP reacts slow enough to ensure homogeneous mixing of the monomer components and fast enough to ensure full conversion.

The methylation of amino functionalities leads to quaternary amino groups located on the backbone of the epoxy. In analogy to DMMP, this results in a considerable shift of the ^{15}N NMR resonance. As the natural abundance of ^{15}N is only 0.37%, epoxies were cured with ^{15}N-labeled ethylenediamine in order to identify the presence of such species with a sufficient signal-to-noise ratio. The $^{15}N\{^{1}H\}$ CP-MAS spectrum of DMMP fortified epoxy is shown in Figure 6.3. Additionally to a broad, intense peak at -353.4 ppm, two relatively small resonances (321.2 and -326.7 ppm) are observed, which are absent in the corresponding $^{15}N\{^{1}H\}$ CP-MAS spectra of either unfortified or DMSO fortified epoxy. Moreover, the $^{15}N\{^{1}H\}$ CP-MAS spectrum of a precured DMMP fortified epoxy shows the two additional resonances with weaker intensity, reflecting two different ammonium ions which bear either *one* or *two* methyl groups. The first corresponds to branching points in the polymer network and the respective ^{15}N chemical shift should be at higher ppm values. The formation of labeled nitrogen atoms bearing *three* methyl groups is statistically very unlikely.

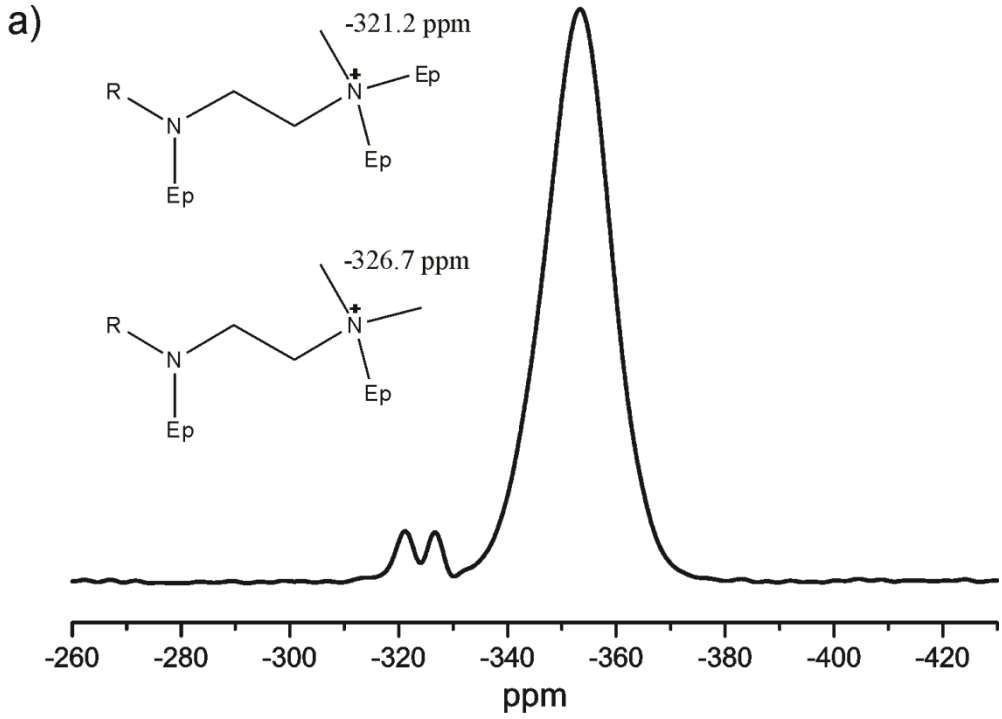

Figure 6.3: $^{15}N\{^{1}H\}$ CP-MAS spectrum of DMMP fortified epoxy cured with ^{15}N-labeled ethylene diamine. Schematic structures of the respective polymer backbone cutouts are given: *Ep* denotes the polymer backbone and *R* aliphatic residues. The spectra were acquired at 30.42 MHz using a Bruker Avance II 300 machine with a contact time of 3 ms, coadding 45056 transients. The experiments were carried out using a Bruker 4 mm double resonance MAS probe spinning at 10 kHz, π/2-pulse length of 4.0 µs and a recycle delay of 6 s.

In this work, the fortification concept of alkylation of amino functionalities is extended to a series of DMMP derivatives, thereby systematically exploring the effects of side group character and cure process on the resulting properties of the fortified epoxies (Figure 6.4). The fortifiers can be classified into four groups, depending on their structure. Schematic polymer residue cutouts are shown below the respective fortifiers. Charges within a red or blue circle represent pendant bulky residues (i.e. benzyl group) that prevent close contact of the respective negative and positive charge centers. A representative reaction scheme is shown in the upper left corner. It is important to note that in principal, in the presence of amines, **(6)** cannot only transfer a methyl group but may also suffer cleavage of the bridging glycol unit between both phosphonate moieties. However, as shown below, the reactivity of alkyl chains longer than methyl is heavily reduced.

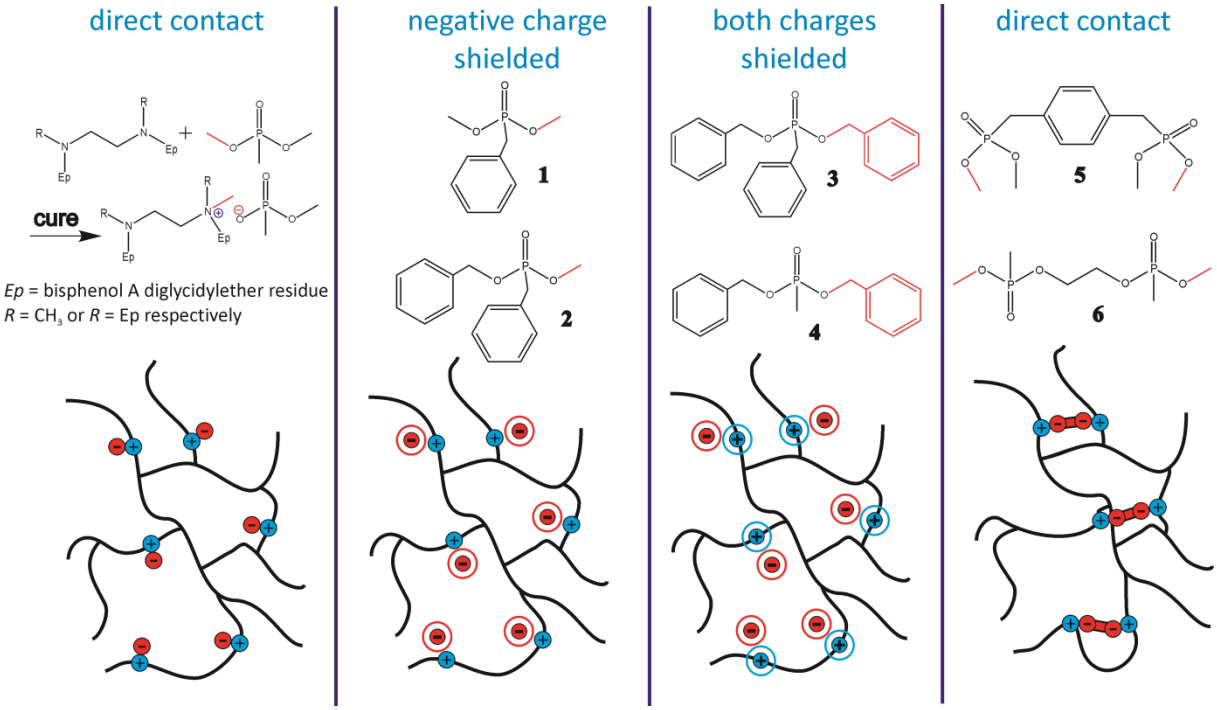

Figure 6.4: Basic concept to systematically evaluate effects of side groups on the epoxy's properties. The fortifiers classified in this work can be classified in four groups, depending on the presence of bulky residues.

This should provide a first impression of the potential of this kind of phosphonate-epoxy systems. It is known from DMMP fortified epoxy that a gradual loss of mechanical and thermal properties occurs within weeks if stored at room temperature.[55] This is an essential issue with respect to industrial applications that rely on long-term stability. In consequence, glass transition temperature and tensile tests were conducted for aged as well as freshly synthesized samples. In order to introduce bulky moieties into the epoxy, the benzyl group is a convenient choice since such compounds can be synthesized from commercially available precursors and show sufficient reactivity to allow for a transfer from the phosphonate to the amine functionality within reasonable cure conditions (i.e. not exceeding 84 h cure at 110°C).

In principle, alkylation of the epoxy backbone creates two charges that attract each other: a negative charge located on the phosphonate ion and a positive charge on the tetraalkyl ammonium ion. The force acting simultaneously on both charges can be estimated according to Coulomb's law if both moieties are approximated as point charges. It is proportional to $1/r^2$, where r is the separation distance. Increasing the distance between both charge centers, leads to a rapid decrease in electrostatic attraction. This may be achieved by introducing bulky side groups that "shield" either the negative (fortifier) or positive (backbone) charge, possibly tailoring the electrostatic interactions that are considered to

mediate the observable fortification. Bifunctional fortifiers bearing *two* phosphonate groups should be capable of connecting two positive charge centers, thereby increasing the apparent crosslink density. According to a rule of thumb this should further increase T_g while improving the mechanical properties of the epoxies. To be able to conduct sufficient tensile tests for adequate characterization, multiple grams of an additive have to be synthesized. For **(2)**, only 15 mol% fortified epoxy was prepared as the synthesis is too elaborate to synthesize the amount necessary to conduct tensile test measurements at various concentrations. For DMMP, values for tensile stress, E-modulus and glass transition temperature for concentrations other than 15 mol% have already been published.[38]

6.3 Identification of Suitable Cure Conditions

6.3.1 Reactivity of Phosphonate Based Fortifiers

$^{31}P\{^{1}H\}$ CP-MAS-NMR in the solid state is the method of choice for determining reaction processes of phosphonate based fortifiers. Measurements are non-invasive, rapid (several minutes) and no more than 20 mg of sample are required. Two well-separated resonances are visible: resonances centered at around 23 ppm and 33 ppm correspond to dealkylated fortifier and non-reacted fortifier, respectively, though exact chemical shifts depend on the specific fortifier (cf. Figure 6.2). It is assumed that after cure and subsequent cooling to room temperature, the dealkylation reaction is halted. In a cross-polarization (CP) experiment, polarization is first transferred from the abundant spins, in this case ^{1}H, to the dilute spins (^{31}P), and the signal from the dilute spins is then observed. Since the spin-lattice relaxation of proton spins is faster than in the case of other spin ½ nuclei, the CP experiment can be rapidly repeated. However, it is important to keep in mind that polarization transfer depends on a variety of parameters such as dipolar couplings between ^{31}P and ^{1}H and the contact time.[56-58] Thus, such spectra are often not quantitative. Nevertheless, in preliminary measurements, CP contact time was varied stepwise from 50 µs to 3 ms and no significant change in *relative* intensities between the resonances at 23 and 33 ppm was observed, rendering integration of the ^{31}P signal intensities a valid method for determining the relative degree of dealkylation. All spectra were recorded with 3 ms contact time to maximize intensity for a given number of scans.

DMMP possesses a beneficial reactivity as it reacts slow enough to ensure homogeneous mixing of the monomer components and at the same time fast enough to avoid prolonged curing of the epoxy. Phosphites are structurally related to phosphonates but the alkyl group directly bound to phosphorus is exchanged for hydrogen. Indeed, the reactivity of dimethyl phosphite **(7)** was found to be even higher than that of DMMP (Figure 6.5). However, phosphonates with a specific structure such as **(8)** may also exhibit an extraordinary dealkylation affinity. The high reactivity of **(7)** and **(8)** prevents homogeneous mixing with the amine monomers, especially EDA because DMEDA is sterically hindered. No stable, transparent solution can be obtained as salt precipitation occurs almost instantly and the mixture turns turbid. Most likely, **(7)** reacts faster than DMMP due to steric reasons. In the case of **(8)** however, high reactivity is attributed to the –I (electron withdrawing) effect of one phosphonate functionality on the neighboring phosphonate group and vice versa,

possibly stabilizing the formed negative charge after dealkylation. If the methoxy group in phosphonates is exchanged for an ethoxy substituent (cf. **(11)**), dealkylation is reduced tremendously. After a conventional cure process (3 h at 50°C, 16 h at 110°C), conversion of **(11)** does not exceed 10%. Attaching a strong electron withdrawing group directly to the phosphorus atom (cf. **(12)**) accelerates the reaction rate expectedly, but still conversion does not exceed approximately 50% after 16 hours at 110°C. This data suggests that steric hindrance is a serious drawback for dealkylation and has to be considered when designing new additives. Although the benzyl group is sterically more demanding than an ethyl group, its rather good reactivity likely results from a +M effect of the phenyl ring, stabilizing any positive charge that occurs during the transition state of the reaction. Exchanging the hydrogen in *para* position of the phenyl ring for methoxy or fluorine supports this hypothesis: a methoxy substituent adds to the +M effect rendering **(9)** more reactive than **(4)**, whereas an electronegative fluorine substituent weakens the +M effect of the phenyl ring, resulting in low reactivity.

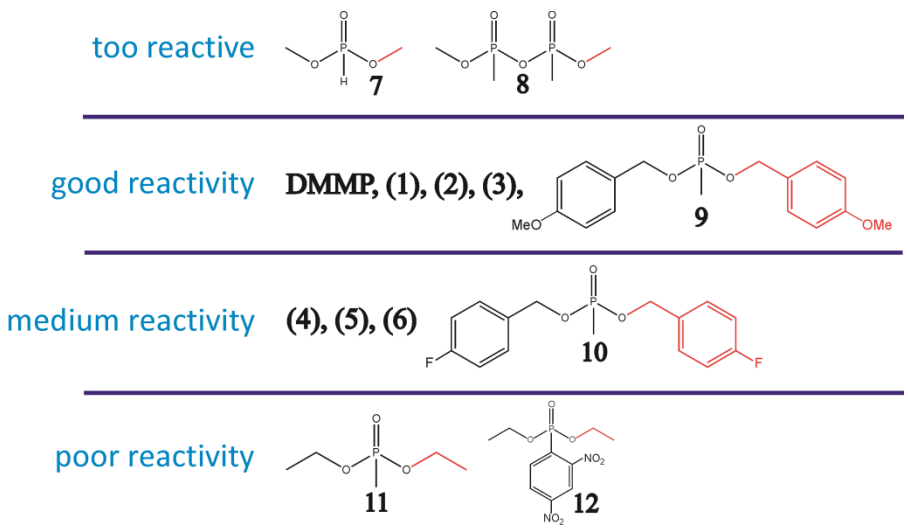

Figure 6.5: Classification of fortifiers according to their reactivity (required cure time with respect to nearly quantitative conversion) that does not necessarily coincide with the *initial* reaction rate data from Table 6.1. For structures **(1)** to **(6)** see Fig. 6.4.

Determining the conversion after 3 hours at 50°C should provide a more quantitative picture of initial reaction rates. A notable point is the high reactivity of **(2)** and **(3)**. One might expect the slowest reaction rate for **(3)** due to its three benzyl rings and the reaction rate of **(2)** to be comparable to **(4)** because both have two rings attached. This is not the case, suggesting that a benzyl group directly attached to phosphorus has a reaction accelerating effect, probably due to transition state stabilizing mesomeric effects. It cannot be excluded that for

similar reasons, **(4)** has a higher initial reaction rate than DMMP. Remarkably, epoxy fortified by **(4)** requires 84 hours at 110°C to react completely and DMMP only 16 hours. In conclusion, the reaction rate of **(4)** seems to slow down with advanced epoxy network formation. It may be speculated that the bulky side groups hamper appreciable diffusion to amino functionalities where debenzylation can occur. In contrast, DMMP is more mobile, even in a highly viscous matrix

Table 6.1. Degree of dealkylation after a 3 h cure at 50°C, determined by $^{31}P\{^{1}H\}$ CP-MAS NMR at 283.48 MHz and 25 kHz MAS using a BrukerDRX700 machine, a contact time of 3 ms coadding 256 transients; π/2-pulse length of 2.5 µs and a recycle delay of 5 s in a typical experiment. All epoxies are 15 mol% fortified.

Fortifier	Conversion (3 h at 50°C)
10	32%
DMMP	43%
3	48%
4	50%
1	58%
9	63%
2	76%

6.3.2 Reactivity Difference of Methyl and Benzyl Group

To address the exact difference in reactivity between methyl and benzyl group, ^{13}C labeled **(2)**, benzyl methyl-^{13}C benzylphosphonate **(13)**, was applied. Compared to unfortified epoxy (not shown), three additional ^{13}C resonances (marked with a "red roof" in Figure 6.6) appear in the ^{13}C MAS experiment of 15 mol% fortified epoxy. The two resonances around 53.5 ppm and 43.5 ppm are assigned to the quaternary ammonium cations and tertiary amines respectively. The anion intensity is located at approximately 52 ppm. The methylated nitrogen atoms are part of the polymer backbone. The spectrum in black is of dimethyl-^{13}C methylphosphonate **(15)** fortified epoxy and proves the peak assignment: The intensity of both methylated nitrogen moieties (with black hat) add up to the same intensity as of the methoxy group of demethylated **(15)**. This is expected, because for every methylated nitrogen, one demethylated DMMP anion remains. Due to their fortifier independent nature, the two resonances originating from methylated nitrogen moieties can be found at the same chemical shift (43.7 and 53.4 ppm) for both epoxies. The shifts of the ^{13}C-labeled methoxy group of debenzylated **(13)** and demethylated **(15)** differ by 0.6 ppm (51.6 and 52.2

ppm respectively). By comparison of signal intensity reflecting methyl groups transferred from **(13)** to the polymer backbone with the intensity of methyl groups remaining at debenzylated **(13)** directly affords the reactivity ratio between the benzyl and methyl group. It turns out that the *average* probability of demethylation for a given molecule of **(13)** is 80%, but only 20% for debenzylation. Reaction conditions such as viscosity constantly change during the hardening of the epoxy and may favor either demethylation or debenzylation at a given point in time. In summary, the methyl group has a higher reactivity than the benzyl group, suggesting that the superior initial reaction rate of **(3)** and **(1)** is due to the benzyl group directly attached to phosphorus.

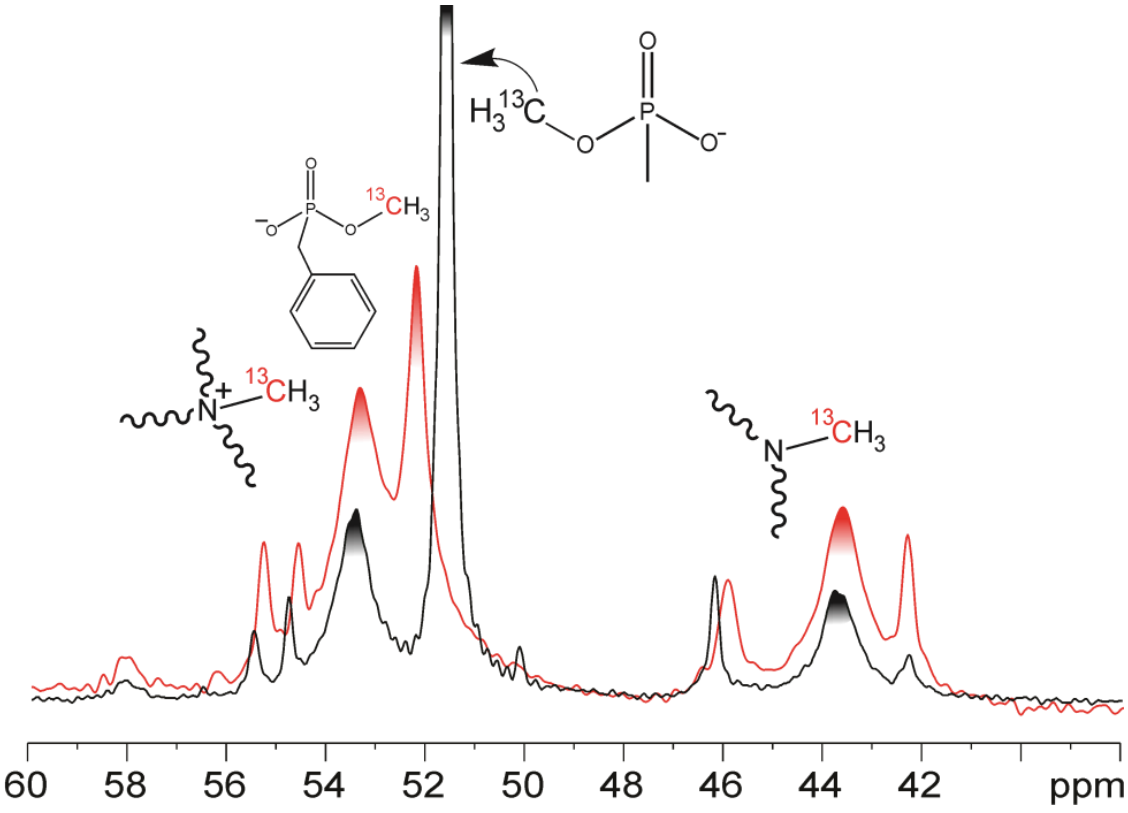

Figure 6.6: Aliphatic region of the ^{13}C single pulse spectra of epoxy fortified by 15 mol% **(13)** (red) and **(15)** (black) respectively. Peak assignment of important resonances is given by the structures depicted. All spectra were acquired at 125.76 MHz using a Bruker DSX 500 machine with a simple single pulse coadding 6144 transients. The experiments were carried out using a Bruker 2.5 mm double resonance MAS probe spinning at 25 kHz, a π/2-pulse length of 2.5 µs, and a recycle delay of 10 s. Using a recycle delay of 60 s did not change the *relative* resonance intensities. Thus, the spectrum should be quantitative. Temperature was set to 100°C to decrease line widths and increase resolution. Notably, the resonance of demethylated **(15)** has a relatively small line width compared with demethylated **(13)** due to the higher mobility of the smaller anion **(15).**

6.3.3 Clustering of Phosphonates

As reported earlier, possible clustering of fortifier molecules in DMMP-fortified epoxy was investigated via a ^{31}P DQ filtered experiment. A DQ signal in principle can only be produced if at least two ^{31}P spins (like or unlike) are coupled (see ref. [55] for experimental details). It was found that no significant DQ intensity was observable for aged epoxy and excluded ionic clustering of fortifier molecules.

To check if aging is related to the gradual breakup of initially formed ionic clusters that are no longer existent for aged epoxy, the experiment was repeated for freshly prepared DMMP fortified epoxy, just a few hours after synthesis. Recoupling times ranged from 2.4 ms up to 10 ms, but only a very faint signal was recorded. Even more importantly, intensity did not change considerably when the experiment was repeated weeks later after aging. Consequently, although confined local rearrangements within the epoxy cannot be excluded, major morphology changes appear unlikely.

6.3.4 Side Reactions

Fortifiers **(7)** and **(12)** are not listed in Table 3.1 as these molecules undergo side reactions during cure as evidenced by ^{31}P NMR. In Figure 6.7, the ^{31}P{^{1}H} CP-MAS heteronuclear correlation (HETCOR) spectrum of epoxy fortified with 15 mol% **(7)** is shown. The ^{31}P resonance at 5 ppm in the direct dimension (F_2) can be assigned to the demethylated **(7)** anion and correlates in the indirect dimension (F_1) strongly with its P-H proton at 6.5 ppm and rather weakly with the methoxy protons at around 3.5 ppm. However the broad resonance at 22 ppm is *not* unreacted **(7)** as the ^{31}P chemical shift of dimethyl phosphite dissolved in $CDCl_3$ is 11.0 ppm and this value should be similar in the solid state. A closer inspection reveals that this peak's correlation center is around 3 ppm in the indirect dimension and that no P-H correlation (expected at 6 ppm in F_1) is detected. Consequently, most likely the P-H bond is no longer present for this species. Judging from the one-dimensional ^{31}P{^{1}H} CP-MAS spectrum (not shown), the side product(s) portion is approx. 10%. Notably, epoxies fortified with diethyl or dibutyl phosphite respectively yield even more (approx. 40%) side products with intensity spreading from 37 to 15 ppm in the ^{31}P{^{1}H} CP-MAS spectrum. Thus, this seems to be a general issue of phosphites.

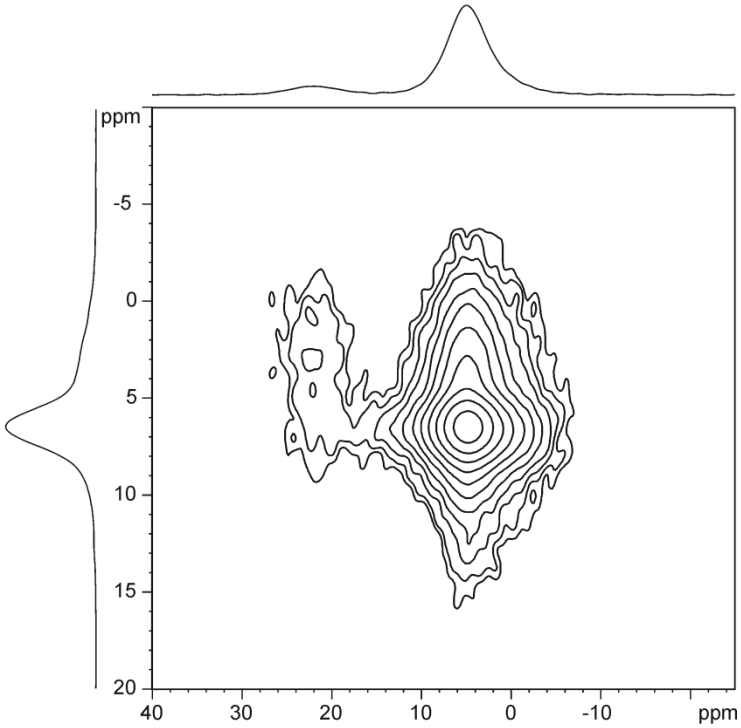

Figure 6.7: ^{1}H-^{31}P CP-HETCOR-MAS spectrum of dimethyl phosphite **(7)** fortified epoxy (cured 3 h at 50°C and 16 h at 110°C) recorded at 700.3 MHz and 25 kHz MAS using a Bruker Avance 700 machine with a commercially available Bruker 2.5 mm double resonance MAS probe, π/2-pulse lengths of 2.5 µs for both ^{1}H and ^{31}P and a short contact time of 500 µs. A total of 40 t_1 increments at steps of 50 µs and 4096 transients per increment have been added with a relaxation delay of 2 s.

The situation is similar for **(12)**. As soon as **(12)** is mixed with amine monomers, the solution turns red immediately and darkens gradually, pointing at the formation of strongly visible light absorbing byproducts. Interestingly, the ^{31}P{^{1}H} CP-MAS spectrum of epoxy fortified by 15 mol% **(12)** and cured for 3 hours at 50°C and 16 hours at 110°C shows no distinct byproduct intensity (Figure 6.8). The resonance at 1.5 ppm is assigned to monodemethylated **(12)** as it grows at expense of the resonance at 12.5 ppm (non-reacted **(12)**) in the course of the cure. Dissolving **(7)** and **(12)** in an approx. tenfold excess of EDA, stirring the solution for 16 hours at 110°C to mimic conditions during cure and conducting a subsequent ^{31}P liquid state NMR analysis of the reaction products in D_2O confirms that the major reaction pathway is the monodealkylation for both **(7)** and **(12)**. The appearance of multiple ^{31}P resonances with low intensity points towards the formation of a complex mixture of side products but their overall intensity is comparable low.

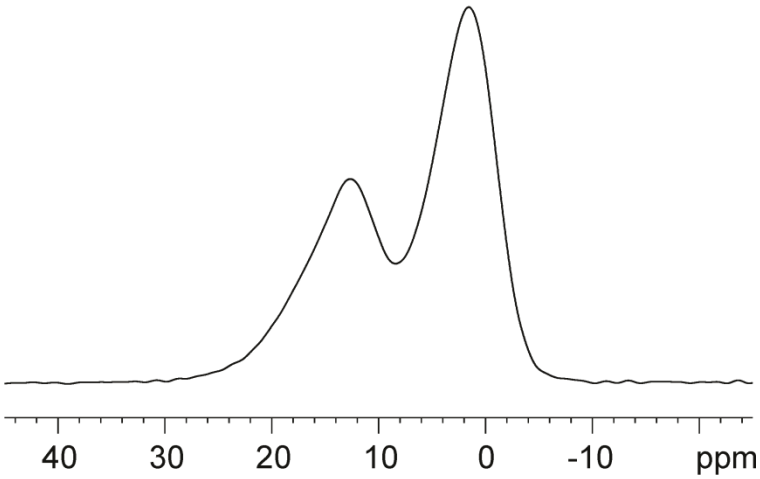

Figure 6.8: $^{31}P\{^{1}H\}$ CP-MAS spectrum of epoxy fortified by 15 mol% **(12)** at 283.5 MHz, 2 ms contact time and 25 kHz MAS using a Bruker Avance 700 machine with a commercially available Bruker 2.5 mm double resonance MAS probe.

6.4 Thermal and Mechanical Properties

Triethylphosphine oxide (TEPO) is structurally similar to DMMP, but completely unreactive (Figure 6.9 a); hence no charge formation occurs during cure. Thus, it is a valuable compound in order to assess the effect of charge formation. In our model epoxy, TEPO acts in part as plasticizer as can be seen from the low tensile stress (50.9 MPa), as well as T_g (52°C). However, E-modulus (2.7 GPa) is slightly higher than of unfortified epoxy (2.5 GPa). In addition, the DMTA scan of TEPO fortified epoxy exhibits a reduction of the high-temperature part of the β-relaxation, which is typical for non-reactive fortifiers such as DMSO.[38] So a definite classification (fortifier or plasticizer) cannot be made. The important point is that epoxy fortified with the reactive pendant DMMP shows, despite its structural similarity with TEPO, very different characteristics. First, there is no reduction in the β-relaxation transition compared to unfortified epoxy. Second, T_g, tensile stress and E-modulus are simultaneously increased for phosphonate fortified epoxies, clearly demonstrating the central significance of charge formation.

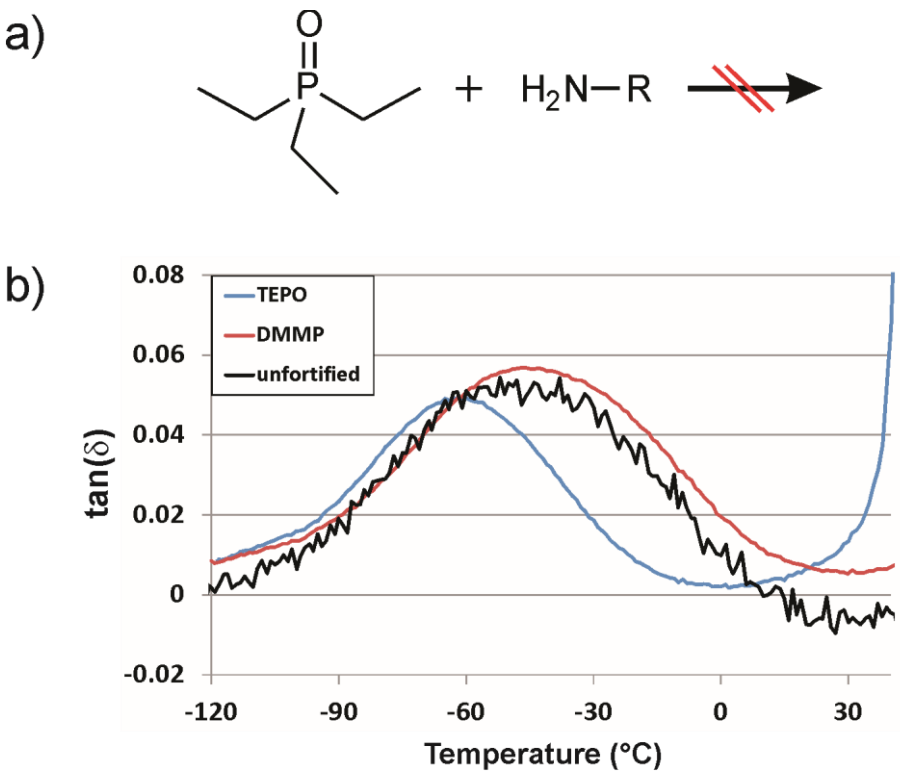

Figure 6.9: a) TEPO is not a phosphonate ester, consequently it cannot react with amines. b) Dynamic mechanical thermal analysis (DMTA) data of TEPO fortified epoxy (15 mol%), compared with DMMP and unfortified epoxy in the temperature region of -120°C to +40°C. DMTA data was collected on an Ares LS from Rheometric Scientific by shearing a single cantilever beam from -120 to +150°C at a maximum strain of $\varepsilon = 10^{-4}$, constant frequency of 1 Hz and temperature ramp rate of 2 K/min. DMTA scans were conducted by Andreas Hanewald.

Figure 6.11 lists the mechanical and thermal properties of epoxies fortified by the additives listed in Figure 6.4. The data was extracted from conventional tensile tests (see experimental section). Two representative tensile test curves are plotted in Figure 6.10. Clearly, DMMP fortified epoxy increases tensile stress and E-modulus. Notably, the stress-strain curve is markedly different from the schematic stress-strain curve for thermoplastic polymers shown in Figure 2.7. Instead, it rather resembles the shape of a typical brittle material and hence, the materials fracture before necking can occur.

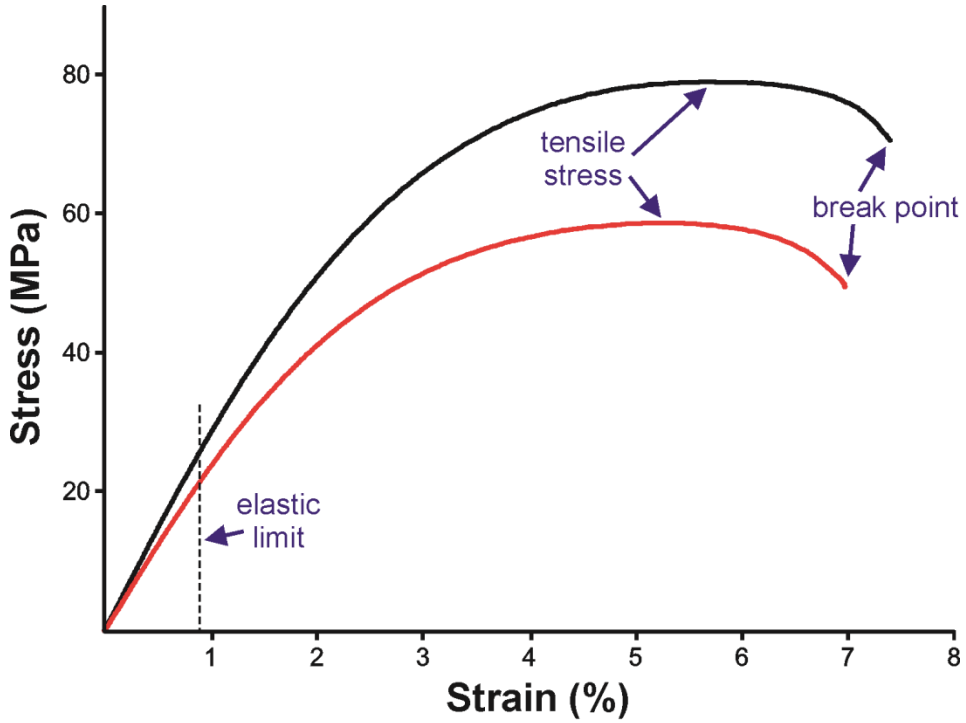

Figure 6.10: Tensile tests for unfortified (red) epoxy and epoxy fortified by 15 mol% DMMP (black). The E-modulus is extracted from the slope of the stress-strain curve within the elastic limit. Tensile stress is the maximal stress. The materials fracture before considerable necking can occur. This is common for highly cross-linked, brittle materials.

As can be seen, mechanical properties are enhanced by all additives. Tensile stress as well as E-modulus gradually increase with increasing fortifier concentration. For DMMP, values for tensile stress, E-modulus and glass transition temperature for concentrations other than 15 mol% have already been published.[38] In contrast, T_g does not necessarily rise with increasing fortifier addition (cf. Figure 6.11c), even though all additives lead to a higher T_g compared to unfortified epoxy (except for **(4)** at 20 mol%). As mentioned above, for **(2)** only 15 mol% fortified epoxy was prepared as the synthesis is too elaborate to synthesize the amount necessary to conduct tensile test measurements at various concentrations. Importantly, epoxy fortified with 20 mol% **(5)** is opaque after cure, although a transparent solution is obtained during mixing of monomers, indicating that the solubility of **(5)** decreases considerably with proceeding network formation. This results in inconclusive DSC data regarding the determination of the glass transition temperature, so that no T_g is given. For this reason, the respective mechanical data at 20 mol% for **(5)** should be interpreted with caution. In addition, the rather unexpected and sudden decrease in tensile stress for 20 mol% **(5)** fortified epoxy can be most likely attributed to the inhomogeneous structure.

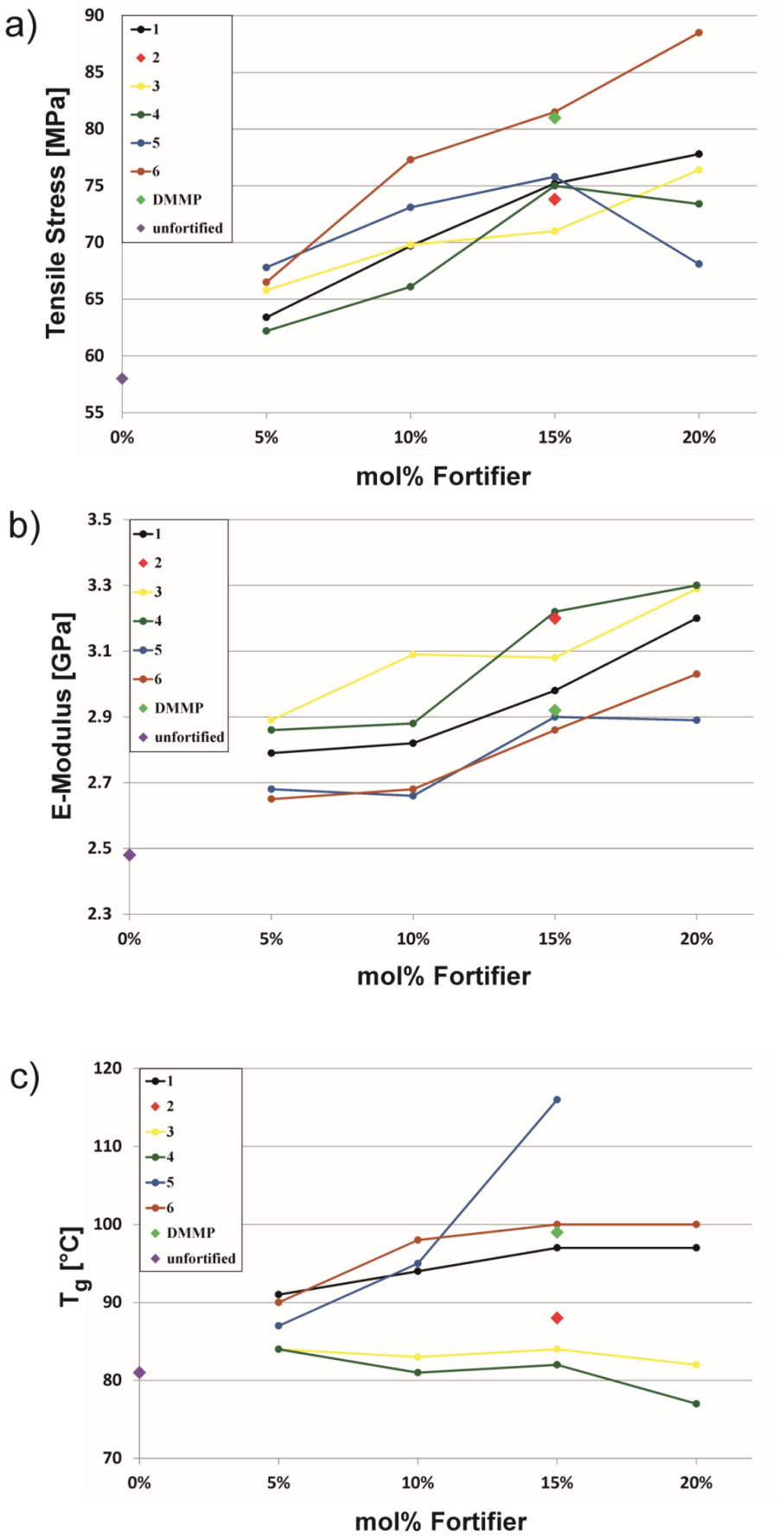

Figure 6.11: a) Tensile stress increases with increasing fortifier concentration. In general, values exceed those for unfortified epoxy considerably. b) Similar to the tensile stress, E-modulus rises for all fortified epoxies. c) The glass transition does not necessarily rise with increasing fortifier concentration.

Tensile stress, E-modulus and T_g for 15 mol% fortified epoxies are plotted in Figure 6.12, since a concentration of 15 mol% is a good compromise between fortifier consumption and properties enhancement. Corresponding epoxies with bifunctional fortifiers **(5)** and especially **(6)** exhibit superior high tensile stresses. Comparing **(2)** and **(4)**, it appears that only the *number* of benzyl groups is governing the tensile stress, but not the *position*. Using **(3)** as fortifier (who bears most benzyl groups) results in an epoxy with the lowest tensile stress besides the unfortified epoxy. Interestingly, the E-modulus increases with increasing number of benzyl groups. Epoxies fortified with **(2)**, **(3)** and **(4)** yield ≈ 25% higher absolute E-modulus than unfortified epoxy.

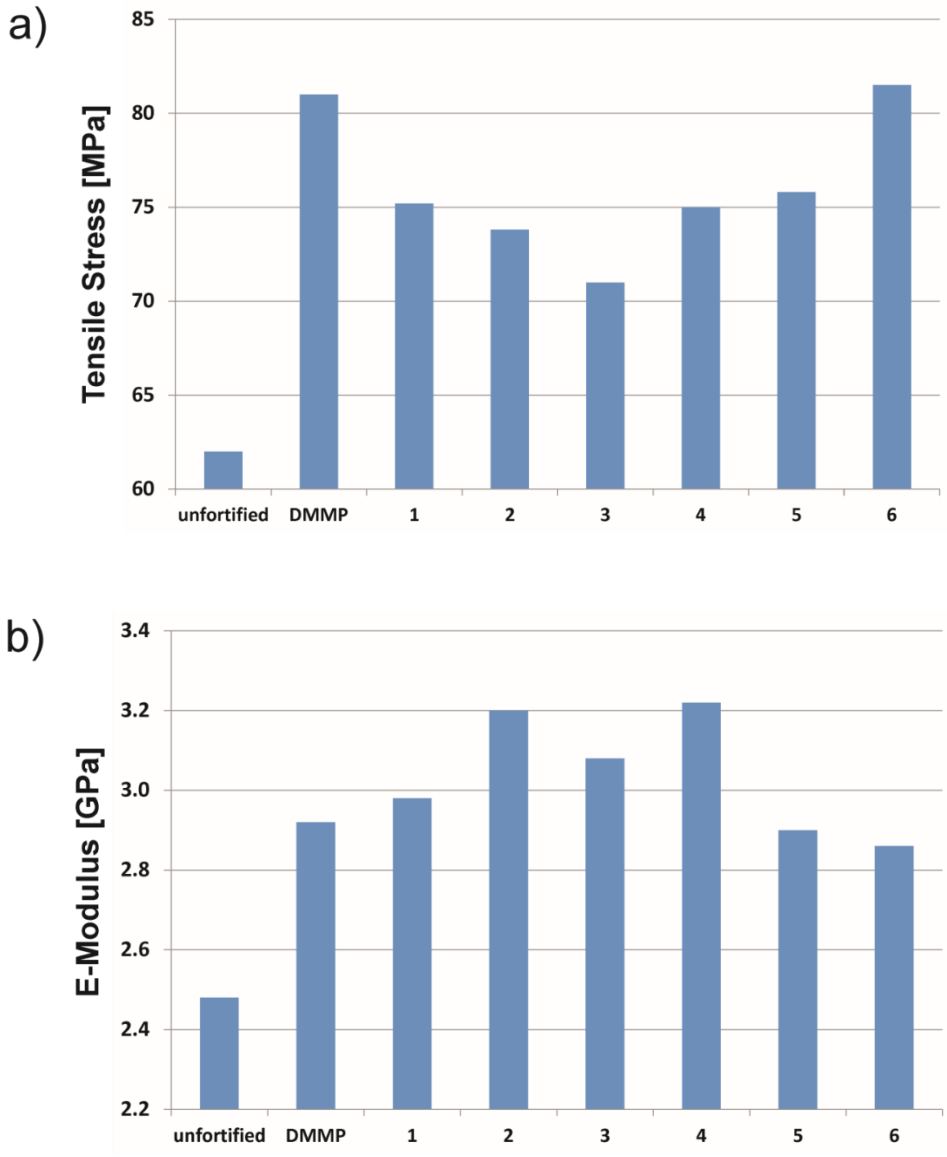

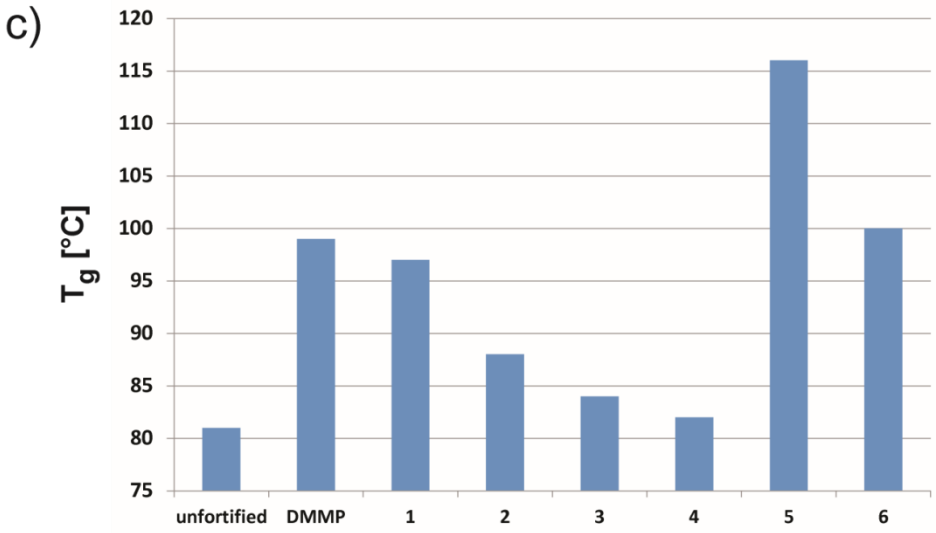

Figure 6.12: a) Tensile stress is sensitive to the number of benzyl groups of the fortifier. **(3)** is sterically the most demanding fortifier and exhibits rather poor performance. b) The dependence of E-modulus on fortifier type. Contrary to a), bulky side groups enhance the E-modulus. c) Compared to tensile stress and E-modulus, the glass transition of **(2)**, **(3)** and **(4)** fortified epoxy is rather close to unfortified epoxy.

In summary, epoxies modified by bifunctional fortifiers exhibit thermal and mechanical properties similar to DMMP fortified epoxies. This may not come unexpectedly, since **(5)** and **(6)** are capable of strong electrostatic interactions similar to DMMP (cf. Figure 6.4). However, there is no apparent effect of two phosphonate functionalities attached to one molecule on the E-modulus. Although all fortifiers considered enhance mechanical properties, a more detailed inspection reveals that bulky side groups are desirable for increasing E-modulus although they are not of value for tensile stress enhancement. Considering the effect on thermal properties (T_g), the more sterically hindered the additive, the more T_g approaches the value of unfortified epoxy. This may be explained by the unpolar, bulky side groups coming to the fore and acting like local plasticizers while the influence of static interactions decreases. Nevertheless, unfortified epoxy has the lowest T_g.

6.5 Effect of Aging on Thermal and Mechanical Properties

If mechanical properties change with time, one expects an increase in tensile stress and E-modulus due to slow crystallization processes occurring after synthesis. Degradation reactions should not play a significant role as all polymer plaques have been stored in a dark spot at room temperature. However, a gradual decrease in T_g and mechanical properties within weeks could be identified. In Figure 6.13, T_g is plotted versus the age in days for one specific fortifier and plaque. Notably, curves differ for different plaques (batches) with identical fortifier, but differences are small. DSC measurements of different parts for a given

plaque may also differ in the range of 1 – 3°C, even though they were conducted at the same day. This reflects the inhomogeneous nature of the polymer thermosets, where the time scale of the aging process differs spatially.

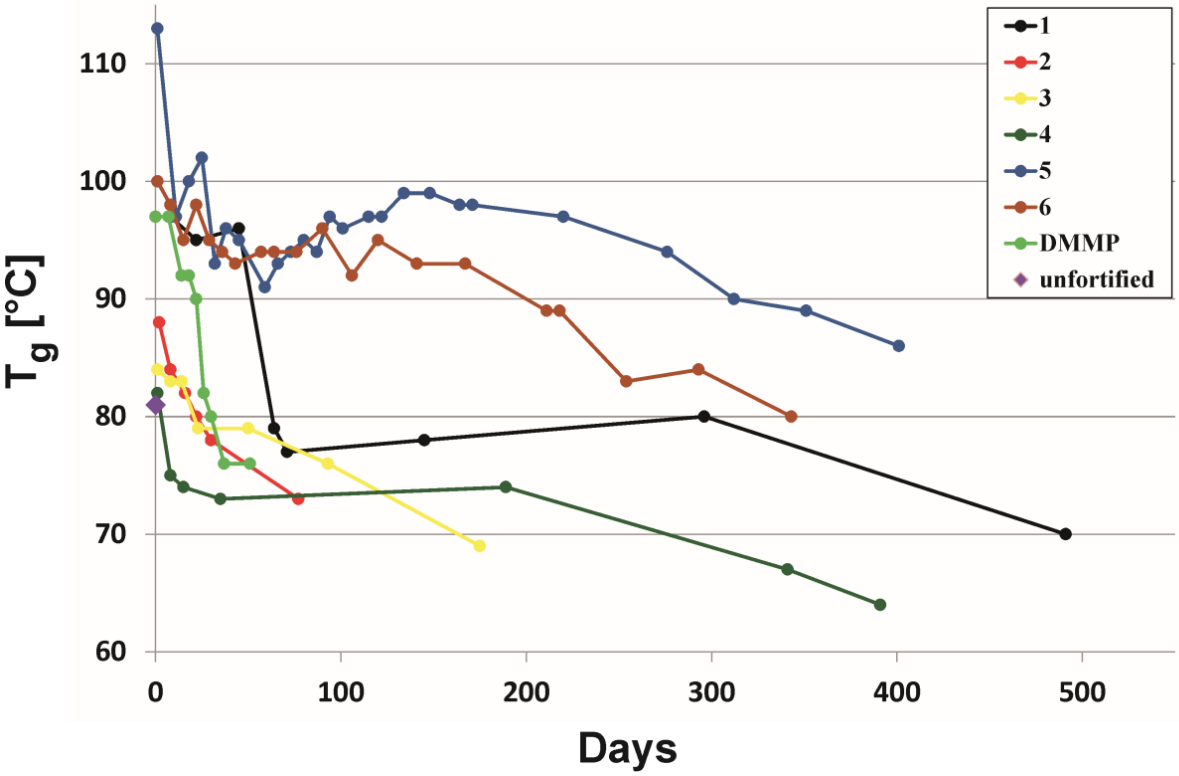

Figure 6.13: Change in glass transition for different fortifiers over time. Note the substantially increased T_g for bifunctional fortifiers and its subsequent approach to the level of unfortified epoxy at about 80°C.

It is necessary to distinguish between monofunctional and bifunctional phosphonates. For monofunctional fortifiers, there is an initial sharp drop in T_g within days, followed by a plateau at around 80°C which extends over almost one year. It may be called the 'unfortified state', as this is also the glass transition region of the unfortified epoxy. After approximately 300 days, a further slow but steady decrease below 70°C is detected. This refers to a "plasticized state" as from now on the fortifier behaves like a plasticizer. For bifunctional fortifiers, data looks similar due to the fact that T_g decreases within days after epoxy synthesis, too. Nevertheless the plateau where T_g remains constant over an extended period of time, is 20°C higher than the value found for monofunctional fortifiers. After a few months, the glass transition approaches values near 80°C. The glass transition of over 1 year old *unfortified* epoxy is about 74°C and data suggests that this is the equilibrium temperature, i.e. no further change of T_g with time is observable.

To check if mechanical properties are similarly depressed upon aging, epoxy plaques containing 15 mol% additive were stored for several months prior to tensile tests. Before testing, it was ensured that T_g had dropped below 80°C to ensure significant aging. Notably, all aged samples exhibit an E-modulus similar to fresh samples, i.e. reflecting clear enhancement compared to unfortified epoxy. However, tensile stress is significantly reduced, ranging now from approx. 50 to 60 MPa with epoxies containing bifunctional fortifiers **(5)** and **(6)** as well as DMMP at the lower end. Summarized, tensile stress and T_g of aged samples fall below the values of unfortified epoxy, whereas E-modulus stays high. In accordance with the results of the tensile tests of fresh samples, this stresses that one has to distinguish between E-modulus and tensile strength when referring to mechanical properties.

Though the molecular details of the aging observed are not fully understood, the absence of significant changes in the corresponding ^{13}C or ^{31}P MAS NMR spectra upon aging suggests that the aging is likely related to (small) local rearrangements of certain polymer segments within the polymer matrix rather than further chemical modification or significant morphological changes. In principal, a thorough relaxation spectroscopy study (dielectric spectroscopy and dynamic mechanical analysis) on aged compounds should provide further insights into this issue. DMMP fortified epoxy stored at -20°C in argon atmosphere for 8 weeks kept its T_g above 95°C, while at the same time a sample of the same original plaque stored at room temperature had a T_g of 83°C. Thus, the internal processes leading to the phenomenon of aging are most likely thermally induced rearrangements of the fortifier and/ or epoxy backbone. This would mean that freshly synthesized fortified epoxies are initially in a perturbed state and far from equilibrium, otherwise no gradual change of properties would be observed. One might suggest that bifunctional fortifiers delay such local rearrangements through their ability to connect different polymer backbone moieties, thereby possibly hampering cooperative motion that facilitates relaxation.

If this is valid, curing of the monomer mixture at elevated temperatures and longer than the period necessary to ensure full conversion should enhance molecular motion and thus speed up the aging process. In Figure 6.14a, the gain in tensile stress for a specific fortified epoxy *compared* to unfortified epoxy (cured 3 h at 50°C and 16 h at 110°C) is marked by a horizontal, black bar. The loss, or alternatively the gain, upon applying elevated

temperatures is shown in red or green, respectively. Indeed, when epoxies were cured 3 hours at 50°C and 24 hours at 110°C, followed by additional 24 hours at 150°C, tensile stress potentially changed markedly. Epoxies fortified with DMMP or **(1)** as small fortifiers loose a significant portion of their initially gained tensile stress. Even though bifunctional fortifiers do not enhance the tensile stress considerably compared to DMMP (see Figure 6.14a), they are superior with respect to retaining fortification at elevated cure processes. Epoxies with sterically more demanding fortifiers or bifunctional fortifiers remain unchanged or even increase tensile stress. Probably, in this regard, sterically demanding and bifunctional fortifiers owe their superior performance to their reduced mobility within the epoxy, even hampering the mobility of the polymer backbone well above T_g. Nevertheless, even after high temperature treatment *absolute* values tensile stress and T_g of these voluminous antiplasticizers are still not distinctly better than those of DMMP.

E-modulus does not change significantly after applying a cure at elevated temperatures (see Figure 6.14b). This is in accordance with the finding that E-modulus does not change upon long storage at room temperature either. This points out that once again, one has to distinguish between tensile stress and E-modulus when discussing mechanical properties. Figure 6.14c is similar to 6.14a in that the biggest loss in T_g is found for the smaller fortifiers. However, T_g for epoxies fortified with **(2)** till **(4)** is already low without high temperature cure, so that the small decrease in T_g may just reflect that these epoxies are already near their equilibrium.

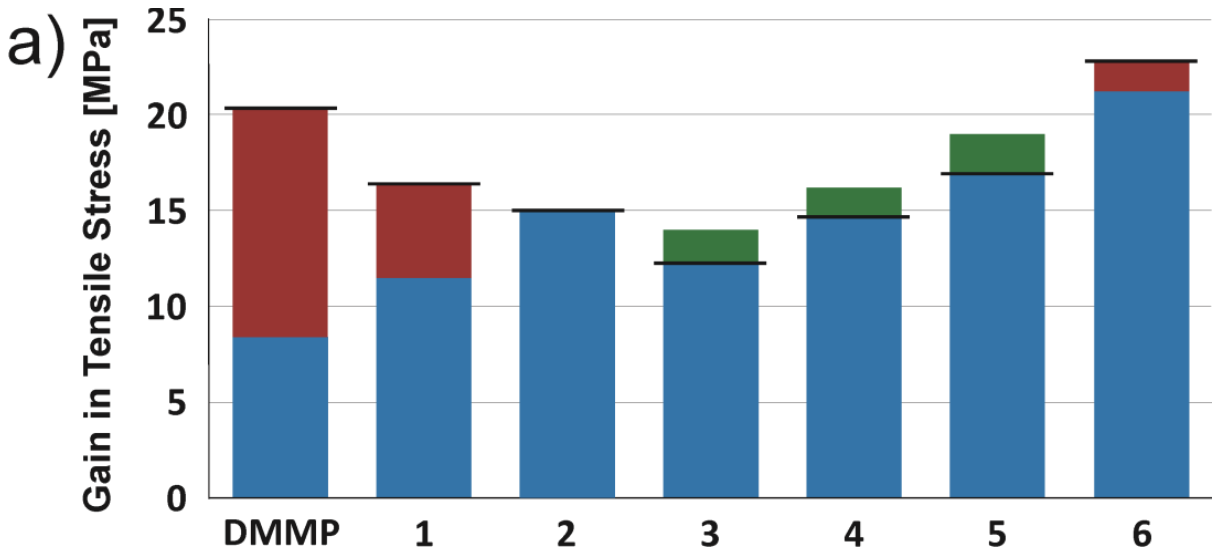

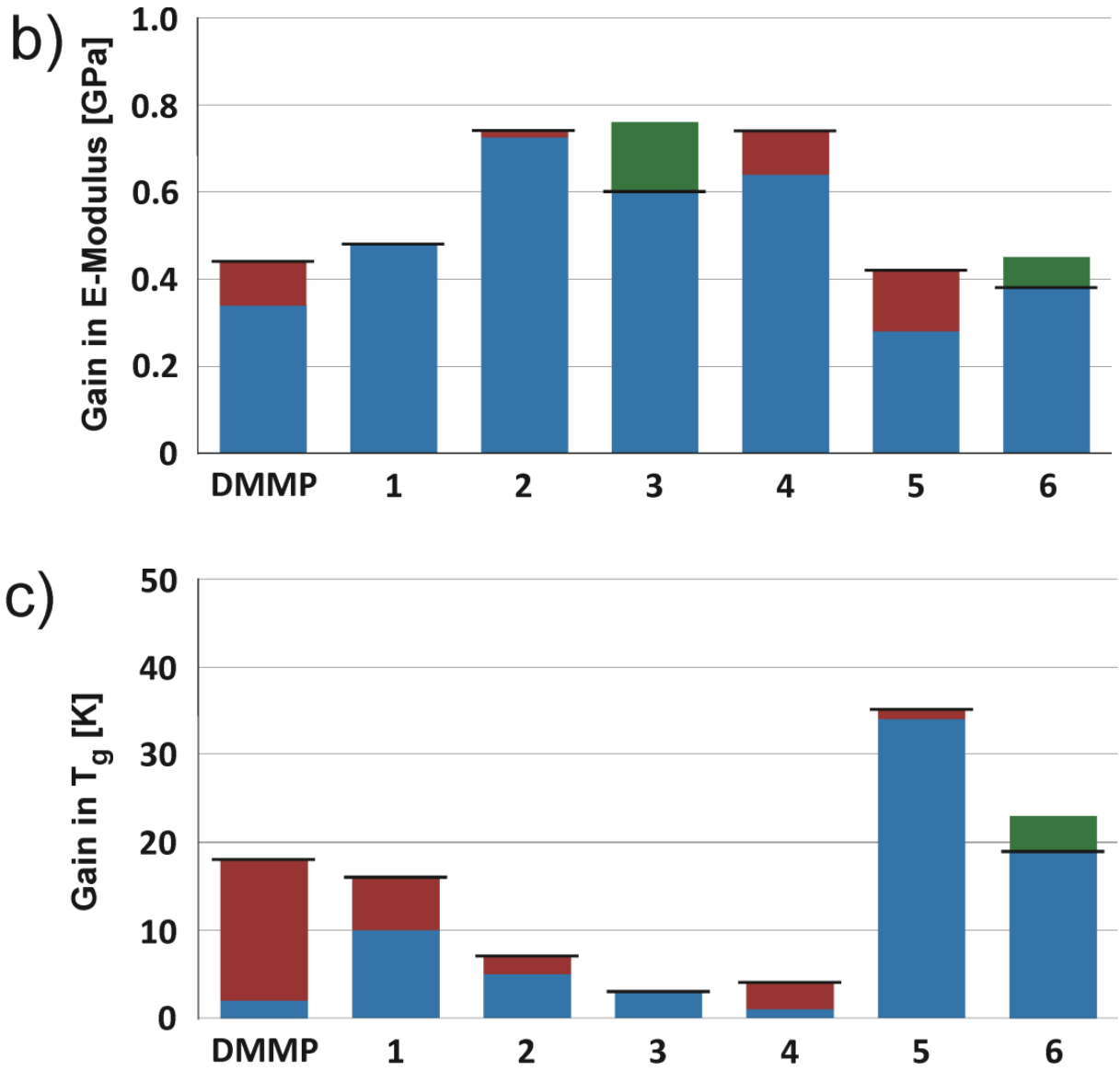

Figure 6.14: The absolute gain in a) tensile stress, b) E-modulus, c) T_g for a specific fortified epoxy compared to unfortified epoxy is marked by a horizontal, black bar. The loss or gain upon applying elevated cure temperatures (cure process: 3 h at 50°C, 24 h at 110°C and 24 hours at 150°C) is shown in red or green respectively. For example, DMMP fortified epoxy has a 20.3 MPa higher tensile stress (79.1 MPa absolute) than unfortified epoxy (58.8 MPa). Applying the extended cure, tensile stress is reduced to 67.2 MPa, i.e. the gain in tensile stress compared to unfortified epoxy is just 8.4 MPa.

Mechanical and T_g data for fortifiers listed in Figure 6.4 can be found in Figure 6.15. **(11)** clearly acts as a plasticizer, mainly due to its low reactivity.

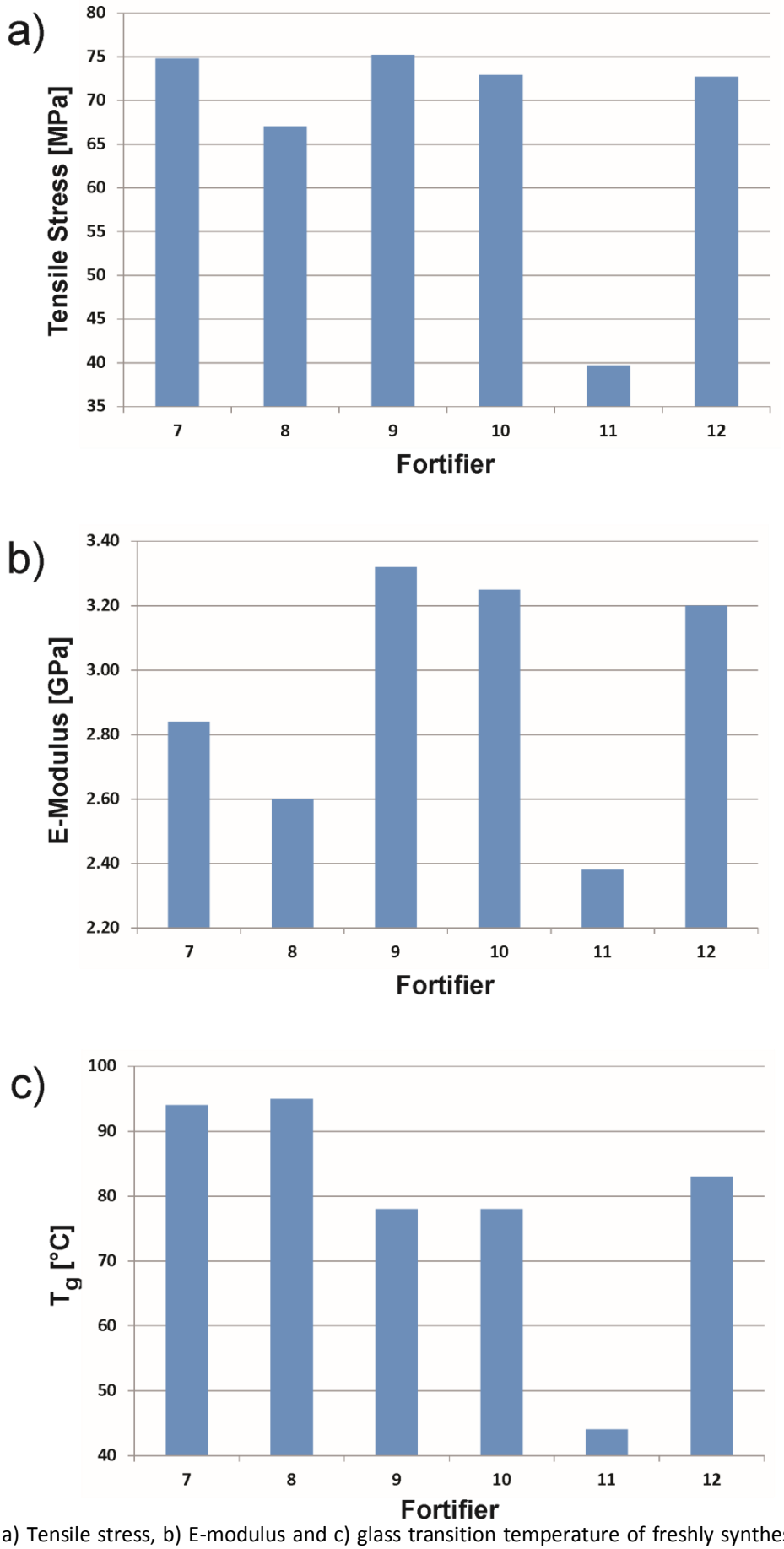

Figure 6.15: a) Tensile stress, b) E-modulus and c) glass transition temperature of freshly synthesized epoxies modified with additives **(7)** to **(12)**. Performance of epoxy modified by **(11)** illustrates the necessity for charge formation to achieve fortification.

6.6 Fortifier Dynamics

6.6.1 Deuteron NMR

As mentioned above, it is believed that aging is related to the local rearrangements of local polymer segments. These arrangements may possibly be induced or supported by additive dynamics. Therefore, solid state NMR was applied to gain insight into the factors determining additive mobility.

The ^{2}H nucleus is very sensitive to molecular reorientations of the C-D bond with respect to the applied magnetic field. Depending on the rate and geometry of the motion, the interaction of the nuclear quadrupole moment with the electric field gradient around the ^{2}H nucleus will be partially averaged.[59] This results in characteristic line shapes that may be compared with computed line shapes resulting from a given model. For the extreme case of rapid isotropic Brownian motion (as commonly found in liquids), a single line with distinct chemical shift is obtained. In contrast, in the static limit one observes a so-called *Pake pattern* with a splitting of the 'horns' equal to 3/4 χ. χ is the quadrupole coupling constant and proportional to the zz-component of the electric field gradient tensor in the principal axis frame (see chapter 2.1.5). Fortunately, C-D bonds in methyl groups are well-defined systems with axial symmetry and $\chi_{\text{eff}} = {}^1/_3\,\chi$ around 55 KHz. This is important, because the line shape is only sensitive to molecular motion that is present on a time scale in the order of the width of the spectrum. χ_{eff} is the effective quadrupole coupling constant already accounting for the fast rotational motion of the methyl group. Fortifier dynamics in DMMP and DMSO fortified epoxies have already been examined by variable temperature deuteron NMR.[50] In case of DMMP it was found that, unlike DMSO, the line shapes cannot be reproduced with a single type of motion and that the Pake pattern breaks down at roughly 10°C for aged epoxy. For freshly synthesized epoxy, the change in line shape with temperature stays the same, but the onset is 15°C higher, reflecting the lower glass transition temperature of aged epoxy.

Diethyl methyl-d_3 phosphonate **(14)** fortified epoxy was applied to a variable temperature ^{2}H solid state NMR analysis. Specifically, the solid echo sequence was used to avoid the receiver dead time problem.[60] Obtained data gives insight into the dynamics of a compound being structurally similar to DMMP, but not influenced by electrostatic motions. As mentioned above, if 15 mol% diethyl methyl phosphonate **(11)** fortified epoxy is cured for 3 hours at 50°C and 16 hours at 110°C, only 10% of all fortifier molecules react with nitrogen

functionalities. Thus, to a first approximation, the spectrum is governed by unreacted **(11)**. As mentioned above, **(11)** should be termed plasticizer, as mechanical and thermal data (T_g: 44°C, tensile stress: 39.7 MPa, E-modulus: 2.4 GPa) are below those of unfortified epoxy. Figure 6.16 compares two spectra of epoxy plasticized with **(14)** (at -3°C and +7°C) with previously recorded spectra of dimethyl methyl-d_3 phosphonate at about 15°C higher temperatures (+7°C and +20°C respectively). Spectra of the full temperature range (230 K – 350 K) are shown in Figure 6.17. For spectra of DMMP-d_3 please see ref. [50]. Apparently, the geometry of the motion is similar for both additives, as can be seen from the very similar line shapes. The only notable difference is the temperature offset of about 15°C: Demethylated DMMP-d_3 exhibits the same ^{2}H line shape (i.e. same motional geometry and jump rate) at constantly higher temperatures.

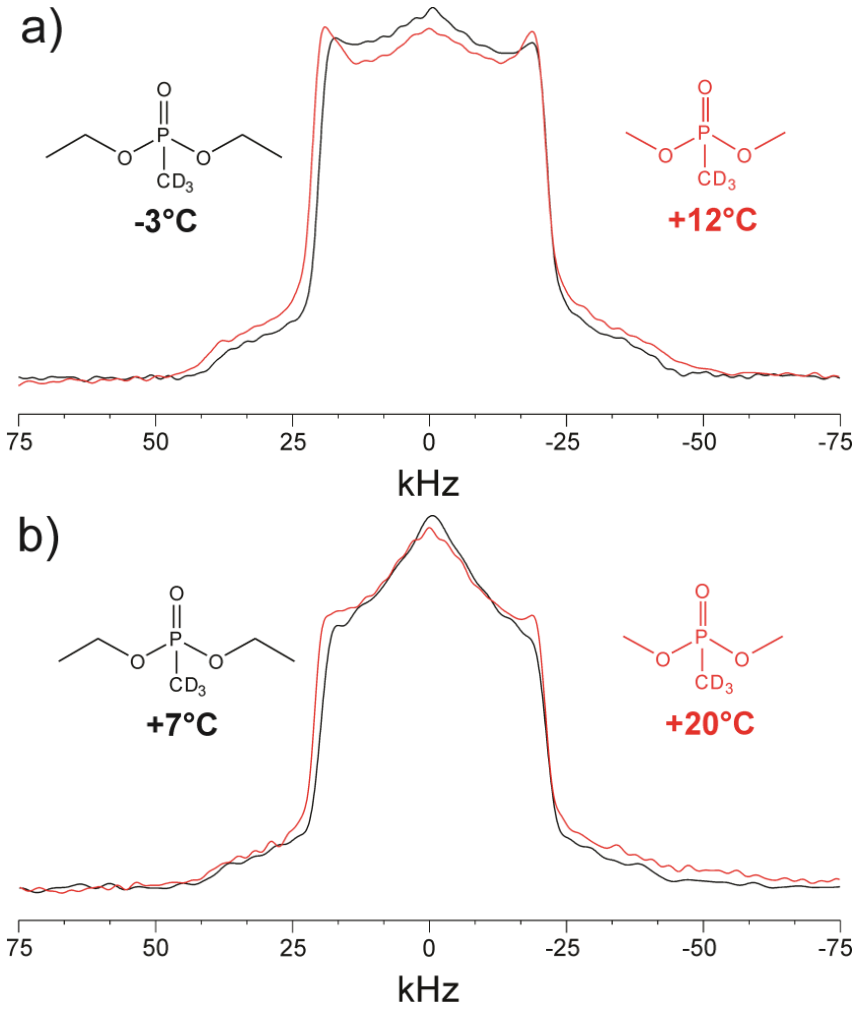

Figure 6.16: Variable temperature ^{2}H solid echo measurements at 76.8 MHz. Typically 20k scans were taken at a relaxation delay of 1 s using an echo delay of 20 µs and a π/2-pulse width of 6 µs. a) Diethyl methyl-d_3 phosphonate **(14)** (black) plasticized epoxy at -3°C and dimethyl methyl-d_3 phosphonate (red) fortified epoxy at +12°C and b) a comparison of epoxy with **(14)** at +7°C (black) and with DMMP-d_3 at +20°C (red). Obviously, the change in line shape with increasing temperature is the same for both phosphonates. However, the onset of a specific jump rate is at an around 15°C lower temperature for epoxy plasticized with **(14)** than for epoxy with DMMP-d_3.

The glass transition temperature of epoxy plasticized by **(14)** is lower than for DMMP fortified epoxy, so this tendency is no surprise. Note that a similar motional mode for both molecules is observed, even though only the addition of DMMP-d_3 results in a quantitative formation of charges due to alkylation of amines in the epoxy backbone. Importantly, DMSO fortified epoxy exhibits a 14°C higher T_g (58°C) than epoxy fortified by **(14)** (T_g = 44°C) despite the fact that the fortifier dynamics of DMSO are much higher at a given temperature.[55] Thus, fortifier dynamics are not only a function of the epoxy's resulting glass transition temperature but also depending on the size/ steric of the additive.

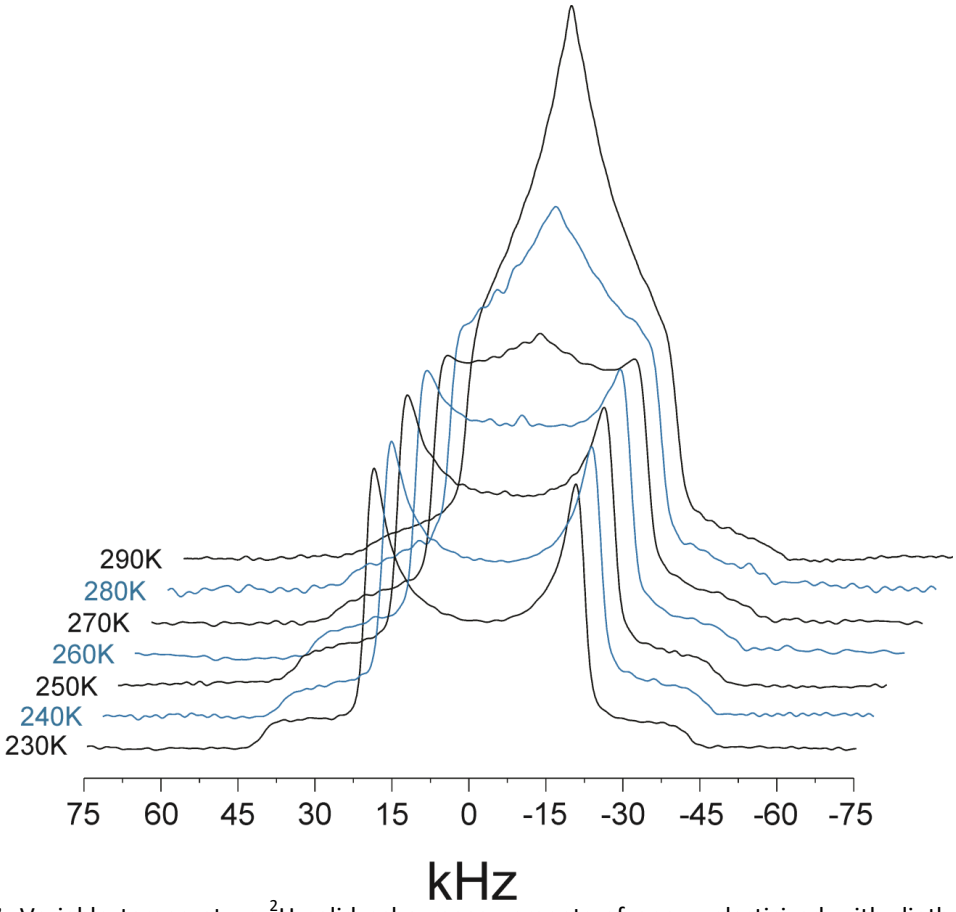

Figure 6.17: Variable temperature ^{2}H solid echo measurements of epoxy plasticized with diethyl methyl-d_3 phosphonate at 76.8 MHz. Typically 20k scans were taken at a relaxation delay of 1 s using an echo delay of 20 µs and a π/2-pulse width of 6 µs. Spectra above 290 K exhibit a simple narrowing of the resonance and are featureless.

6.6.2 ^{31}P Chemical Shift Anisotropy

Synthesis of ^{2}H labeled substances is potentially elaborate and expensive. Moreover, to obtain valuable information about the dynamics of the molecule as a whole, i.e. to exclude superimposed motion of side chain moieties, the position of the spin label has to be specific and well-chosen. For example, in the case of DMMP, the methyl group

directly attached to phosphorus was chosen for deuteration, whereas the methoxy group is not appropriate.

^{31}P is an alternative favorable spin probe to monitor dynamics due to its beneficial properties. With a natural abundance of 100% and a spin 1/2, the NMR intensity is high and spectra are relatively easy to interpret due to missing quadrupolar interactions. The ^{31}P chemical shift anisotropy (CSA) pattern arises from the typically non-spherical electron distribution around the nucleus. Hence, the size of the shielding will depend on the orientation of the molecule within the applied magnetic field. For the phosphonate based fortifiers, heteronuclear dipole-dipole couplings can be removed by applying ^{1}H dipolar decoupling sequences during acquisition. Consequently, only shielding effects contribute to the powder pattern, which can be measured directly from a simple one-dimensional experiment. In general, these patterns span several thousand hertz, depending on the magnetic field strength. To increase the ^{31}P signal-to-noise ratio for the epoxy systems, spectra were recorded with slow spinning samples (ν_R = 2 kHz). Only if the rate of the sample spinning rate ν_R is fast in comparison to the anisotropy of the interaction being spun out, a powder pattern is reduced to a single line at the isotropic chemical shift. Otherwise, a set of spinning sidebands is produced, in addition to the line at the isotropic chemical shift. These are sharp lines, set at the spinning speed apart and radiate out from the line at the isotropic chemical shift. By calculating the expected spectrum for different anisotropy and asymmetry values, experimental patterns can be fitted until reasonable agreement is obtained. Similar to the line shape analysis of variable temperature ^{2}H spectra, enhanced molecular motion, e.g. rotation, results in a (partial) averaging of anisotropic interactions. Thus, with increasing temperature, spinning side band patterns will narrow and finally collapse into one single line at the position of the isotropic chemical shift.[61, 62] CSA parameters obtained from epoxies with additives triethylphosphine oxide (TEPO), DMMP, **(3)**, as well as bifunctional fortifiers **(5)** and **(6)** are listed in Table 6.2.[63] Judging from a single spectrum, it is hardly feasible to ascertain whether or not the rigid limit is reached. Thus, values listed in Table 6.2 are taken from samples cooled down up to 200 K, where the CSA patterns hardly change any further and the rigid limit should be reached. To extract detailed information about the geometry of additive motion, it is necessary to first calculate the orientation of the principal axes system with respect to a molecule-fixed set of axes. However, these

calculations require quantum mechanical calculations, which are not easy, especially for an undefined environment such as a polymeric system. Fortunately, the orientation can be omitted in this study because i) due to their similar structure, the orientation of the PAS with respect to the phosphonate scaffold should be similar for all fortifiers and ii) the absolute values of the chemical shift tensors are very similar, except for TEPO, thus allowing to define a randomly chosen threshold condition with associated temperature T_{SMA}, after which the CSA pattern is considered to be 'substantially motionally averaged'. This condition was chosen to be a 10 ppm overall reduction of the spectrum width ($|\delta_{xx}| + |\delta_{zz}|$). For example, the (averaged) CS tensor values of DMMP at 280 K are δ_{xx} = 89.8 ppm and δ_{zz} = -51.1. This corresponds to a reduction of ($|\delta_{xx}| + |\delta_{zz}|$) of 11.2 ppm. Significant narrowing of the CSA pattern does not occur unless the frequency of the motion is in the range of the total width of the spectra, i.e. 25,000 Hz in the case of the phosphonate additives, allowing for an estimation of the fortifier dynamics.

Table 6.2: CSA parameters according to the standard convention.[63] Nine different elements are necessary to define the shielding tensor. Transformation to the principal axis system (PAS) will diagonalize the matrix to give three principal components (σ_{xx}, σ_{yy}, σ_{zz}). The remaining three variables determine the orientation of the PAS in a molecule-fixed set of axes. To a good approximation $\delta_{\alpha\alpha} \cong \sigma_{\alpha\alpha,\mathrm{ref}} - \sigma_{\alpha\alpha}$ with $\sigma_{\alpha\alpha,\mathrm{ref}}$ as shielding value for an arbitrary reference compound and $\alpha = x, y, z$ respectively.

Additive	δ_{xx}	δ_{yy}	δ_{zz}	T_{SMA} (K)	$(T_g - T_{\mathrm{SMA}})$
TEPO	113.3	101.8	-49.4	240	85
DMMP	95.0	28.4	-57.1	280	92
(3)	97.5	28.1	-72.5	340	17
(5)	97.1	29.3	-70.6	320	69
(6)	97.5	28.9	-63.7	300	73

Figure 6.18 shows the development of the line shape with increasing temperature exemplified with DMMP fortified epoxy. Spectra for the other additives look very similar but the temperature region of T_{SMA} varies. Admittedly, T_{SMA} is a rough measure of mobility and data provides only a tendency rather than a definite temperature with assignable motional rate. Nevertheless, it corroborates the ^{2}H solid echo measurements. TEPO has a higher mobility than DMMP due to lacking salt formation and thus lower T_g of the epoxy. On the other side, applying **(3)** as additive leads to an epoxy with lower T_g than DMMP but owing to its bulky benzyl groups, mobility is substantially reduced (T_{SMA} = 360 K). Furthermore, **(6)**

fortified epoxy has a higher T_g than epoxy fortified by **(3)**, but its flexible glycol moiety allows for enhanced reorientation with increasing temperature (T_{SMA} = 320 K). This also shows that fortifier dynamics are not directly related to T_g. Importantly, the dynamics of side groups are not accessible by this method. Indeed, it is likely that substantial rotation/ dangling of the benzyl groups of **(3)** is already present prior to 360 K, resulting in a comparable low T_g of the epoxy, although rotation of the additive as a whole is not significant yet. Above 400 K, all CSA patterns finally collapse into one single phosphorus resonance, irrespective of the specific kind of fortifier.

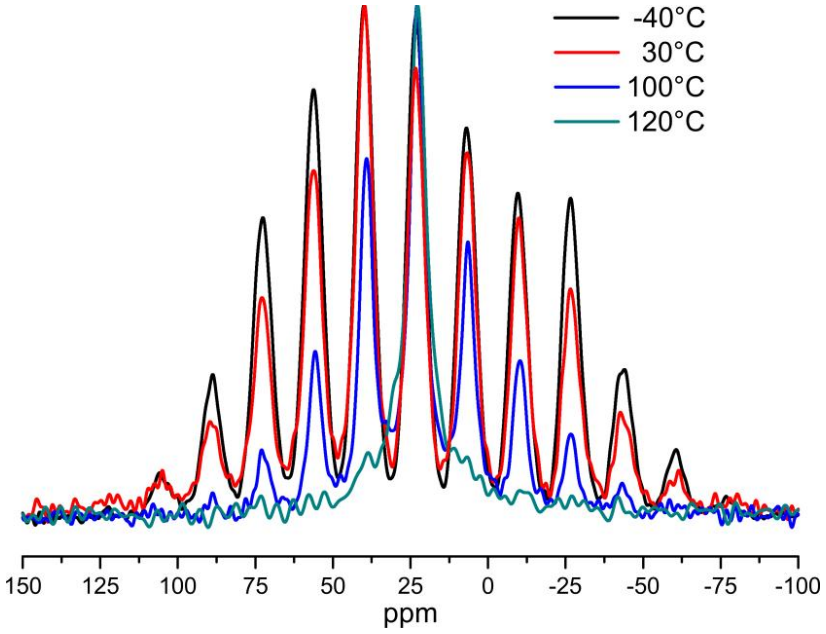

Figure 6.18: Comparison of $^{31}P\{^{1}H\}$ CP-MAS spectra of DMMP fortified epoxy at a spinning frequency of 2 kHz and 122 MHz. 256 scans were taken with a relaxation delay of 5 s. Spin lock period was 2000 µs with a ramp on phosphorus covering 20% of the maximal pulse power. Figure is taken from ref. [50]

7 Summary

Phosphonates constitute a new class of molecular fortifiers through their reactivity with respect to amines. In the course of the cure process, charges on both fortifier and polymer backbone are formed, resulting in unique epoxy properties: T_g, E-modulus and tensile stress are enhanced simultaneously, distinguishing phosphonates from conventional non-reactive fortifiers. In order to explore their impact on thermal and mechanical properties, a variety of phosphonate derivatives was prepared. It was found that the molecular fortifier structure governs the resulting epoxy's properties as well as the time scale of aging processes. In this respect, bifunctional fortifiers proved to be superior to monofunctional ones.

Especially bulky fortifiers exhibited comparable low tensile stress and T_g. The E-modulus however is not affected by aging and is particularly enhanced by bulky fortifiers. Relating to our concept depicted in Figure 6.4, the position of the benzyl group within the phosphonate structure is not as important as anticipated. T_g is somewhat higher for **(1)** and **(2)** compared with **(4)**, but E-modulus and tensile stress do not profit from a close proximity of both charge centers.

Alkyl substituents longer than methyl hardly reacted, although benzyl groups as especially sterically demanding residues were transferred only slightly slower than methyl groups to the polymer backbone. This is attributed to transition state stabilizing, mesomeric effects which can be further tuned by appropriate benzyl ring substituents. Probably for similar reasons, benzyl groups directly attached to phosphorus further enhance phosphonate reactivity. Data obtained from additives TEPO and diethyl methyl phosphonate clearly validated the necessity of salt formation within the epoxy to enhance properties.

Aging is considered to originate from the slow but steady relaxation of the polymer backbone into its equilibrium conformation. Consequently, charge formation during cure induces a non-equilibrium conformation; with the fortifier - attached to the polymer backbone through electrostatic interactions - possibly acting as "barbed hook" and reducing the mobility of adjacent chains. For small fortifiers (**(1)** and DMMP), this process can be appreciably accelerated by a cure temperature above 110°C (e.g. 24 hours at 150°C), allowing for a faster relaxation through high thermal mobility of polymer segments. In contrast, potential cross-linking agents **(5)** and **(6)** prolonged the aging process significantly. Aged epoxies showed no distinct change in $^{13}C\{^1H\}$ or $^{31}P\{^1H\}$ CP-MAS spectra, indicating that changes such as crystallization or phase separation can be excluded.

Fortifier dynamics were investigated by ^{2}H and ^{31}P solid state NMR and found to be dependent on both steric factors and electrostatic interactions.

Although the E-modulus is not affected by aging of the epoxies, further research is necessary to develop additives where epoxies retain the enhanced tensile strength and glass transition temperature after cure. Bifunctional phosphonates demonstrated that simple structural modifications can have a significant impact on aging kinetics. In general, all small molecules prone to dealkylation by amines should act as fortifier. However, reactivity must be adjusted to prevent too high or low reactivity. Another approach is the modification of the amine monomers and/ or epoxy component and elucidation of the ensuing effects on fortified epoxy properties. Further work has to be done in this direction to examine the full potential of this new approach to fortification.

8 Experimental Section

8.1.1 Network Fabrication

Epoxies were prepared as previously described.[50] Fortifier concentration is given as a mole percentage (mol%) of the total monomers used, including the fortifier itself. For fortifiers **(1)** to **(6)**, care was taken to reduce cure periods to the minimal amount of time, but to ensure conversion of phosphonates in excess of 97%. Fortifiers attributed to the category "good reactivity" (Figure 6.5) fully reacted after 3 hours at 50°C and 16 hours at 110°C cure. Those with 'medium reactivity', i.e. **(4)**, **(5), (6)** and **(10),** required a substantially longer cure process: 3 hours at 50°C and 84 hours at 110°C. Solid Fortifiers were added to the epoxy monomer Epon 825™, which was preheated to 50°C, to dissolve the powder and obtain a clear solution before mixing with monomers dimethyl ethylenediamine and ethylenediamine. Occasionally, prior to putting the mixture into the oven, sonication of the mixture for a couple of seconds was necessary to remove air bubbles.

8.1.2 Materials

Ethylenediamine was purchased from Acros; dimethyl ethylene-diamine, diethyl phosphite, dimethyl phosphite, dibutyl phosphite, diethyl methylphosphonate and triethylphosphine oxide was obtained from Sigma-Aldrich while DMMP was delivered from Alfa Aesar. All compounds were used as-obtained without further purification.

8.1.3 Synthesis

Dimethyl Benzylphosphonate

(1)

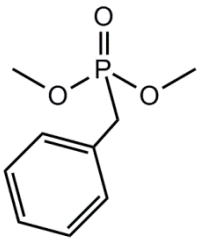

In a typical procedure, a mixture of benzyl bromide (11.89 ml, 0.100 mol) and trimethyl phosphite (22.90 ml, 0.200 mol) was heated to 110°C for 4 h. Dimethyl methylphosphonate as main side product is distilled off at 14 mbar and 130°C oil bath temperature. Subsequently, product (**1)** is obtained by applying a higher vacuum of 0.05 mbar (yield: 13.20 g, 0.066 mol, 66%) as colorless liquid.

^{1}H NMR (250 MHz, CD_2Cl_2): δ_H = 3.15 (d, *J* = 21.6 Hz, 2 H), 3.65 (d, J = 10.8 Hz, 6 H), 7.39 – 7.22 (m, 5 H).

^{31}P NMR (250 MHz, $CDCl_3$): δ_P = 29.28 (s)

Benzyl Methyl Benzylphosphonate

(2)

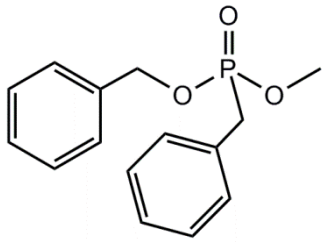

A mixture of dibenzyl benzylphosphonate (11.00 g; 31.23 mol), *N,N*-dimethylethylamine (around 10 ml) and DMSO (around 7 ml) is refluxed for 3 days under vigorous stirring. After removal of DMSO under vacuum (0.05 mbar) for the most part, a high viscous brown gel was obtained which was diluted with 30 ml acetonitrile.

Methyl iodide (0.100 mol) was added dropwise via syringe to the stirring crude mixture at room temperature. Then, the solution was left to stir for half an hour at 50°C followed by removal of acetonitrile under reduced pressure. Care was taken to avoid temperatures over 80°C to prevent decomposition of the product. Crude **(2)** was dissolved in water and extracted with ethyl acetate. Purification was conducted by silica gel chromatography (R_f ≈ 0.6, ethyl acetate) to afford 5.44 g (19.68 mmol; 63%) of a transparent liquid.

^{1}H NMR (250 MHz, MeOD): δ_H = 3.27 (d, *J* = 20.0 Hz, 2 H), 3.63 (d, *J* = 7.9 Hz, 3 H), 5.00 (m, 2 H), 7.39 – 7.25 (m, 5 H).

^{31}P NMR (250 MHz, $CDCl_3$): δ_P = 28.72 (s)

Dibenzyl Benzylphosphonate

(3)

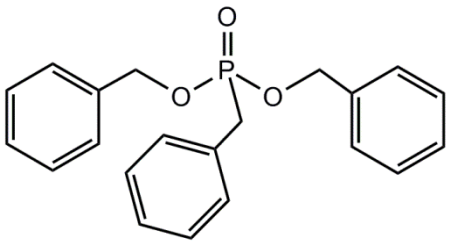

In a typical procedure, benzyl alcohol (62.1 ml, 0.600 mol) was added dropwise via syringe to a stirring solution of phosphorus trichloride (17.45 ml, 0,200 mol) and triethylamine (86.50 ml, 0.621 mol) in 100 ml dry dichloromethane at -78°C under an argon atmosphere. The reaction mixture was stirred for one hour at -78°C, then overnight at room temperature. After filtering the salts, the solvent was removed under reduced pressure, and the crude oil (52 g) was used without further purification (^{1}H NMR suggests approximately 25% byproducts). After adding benzyl bromide (3.48 ml, 0.027 mol) and stirring for 1 h at 100°C, the reaction mixture was then applied to a silica gel column (diethyl ether, R_f = 0.8) and the desired product isolated yielding 24.66 g (0.070 mol, 35%) of a pale yellow oil that crystallizes on standing.

^{1}H NMR (250 MHz, CD_2Cl_2): δ_H = 3.22 (d, *J* = 21.7 Hz, 2 H), 4.96 (d, *J* = 8.2, 4 H), 7.44 – 7.24 (m, 15 H).

^{31}P NMR (250 MHz, $CDCl_3$): δ_P = 27.93 (s)

Dibenzyl Methylphosphonate

(4)

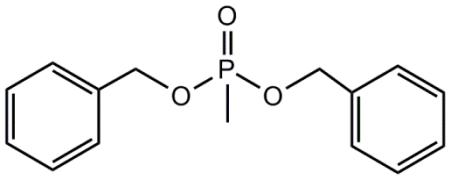

In a typical procedure, benzyl alcohol (10.35 ml, 0.100 mol) was added dropwise via syringe to a solution of methylphosphonic dichloride (6.65 g, 0.050 mol) and *N*,*N*-diisopropylethylamine (17.40 ml, 0.100 mol) in 80 ml toluene at 0°C under argon and stirred overnight at ambient temperature. The suspension is filtered to remove the amine salt and the filtrate is distilled at 0.05 mbar and 180°C oil bath temperature. According to ^{1}H NMR, the condensate contains about 5% impurities. Crude **(4)** is mixed with 150 ml ethyl acetate and byproducts are extracted with 150 ml 0.03 M aqueous NaOH solution. 10.22 g pure **(2)** (0.037 mol, 74%) is obtained after removal of ethyl acetate by distillation in vacuo at ambient temperature.

^{1}H NMR (250 MHz, MeOD): δ_H = 1.52 (d, *J* = 17.6 Hz, 3 H), 5.00 (m, 10 H), 7.43 – 7.29 (m, 10 H).

^{31}P NMR (250 MHz, $CDCl_3$): δ_P = 32.18 (s)

Tetramethyl 1,4-Phenylenebis(methylene)diphosphonate

(5) 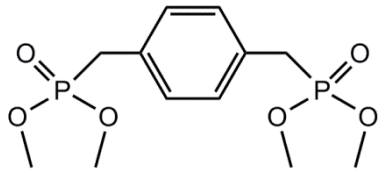

In a typical procedure, a solution of 1,4-bis(bromomethyl)benzene (26.39 g, 0.100 mol) in 23.60 ml trimethyl phosphite (24.83 g, 0.200 mol) was refluxed for 4 h. Notably, 1,4-bis(bromomethyl)benzene dissolves only slowly even at elevated temperatures. Dimethyl methylphosphonate as main side product is distilled off at 14 mbar and 130°C oil bath temperature. The obtained pale yellow powder (29.64 g, 0.092 mol, 92%) was purified by recrystallization from THF.

^{1}H NMR (250 MHz, $CDCl_3$): δ_H = 3.11 (d, J = 20.2 Hz, 4 H), 3.64 (d, *J* = 10.8 Hz, 12 H), 7.24 – 7.20 (m, 4 H).

^{31}P NMR (250 MHz, $CDCl_3$): δ_P = 29.14 (s)

Ethane-1,2-diyl Dimethyl Bis(methylphosphonate)

(6) 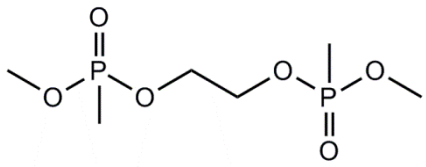

In a typical procedure, diisopropyl azodicarboxylate (44.30 ml, 0.225 mol) was added dropwise via syringe to a stirring solution of methyl hydrogen methylphosphonate[55] (16.5 g, 0.150 mol), triphenylphosphine (59.00 g, 0.225 mol) and ethylene glycol (4.19 ml, 0.075 mol) in 500 ml dry THF under argon at room temperature. The solution was left to stir under argon for the night. The crude reaction mixture was subjected to silica gel chromatography using ethyl acetate ($R_f \approx 0$) to remove all byproducts, followed by 1:3 methanol/CH_2Cl_2 to release 15.26 g **(6)** (0.062 mol, 83%) as colorless liquid.

^{1}H NMR (250 MHz, MeOD): δ_H = 1.59 (d, *J* = 17.7 Hz, 6 H), 3.78 (d, *J* = 11.2 Hz, 6 H), 4.33 – 4.16 (m, 4 H).

^{31}P NMR (250 MHz, $CDCl_3$): δ_P = 33.25 (s)

Dimethyl Dimethyldiphosphonate

(8) 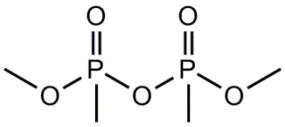

Oxalyl chloride (20.31 g, 0.160 mol) was added via syringe to a stirring solution of dimethyl methylphosphonate (17.34 ml, 0.160 mol) in CH_2Cl_2 and the mixture was refluxed for 8 h. Removal of solvent was performed under reduced pressure was followed by distillation at 30 mbar and 90°C oil bath temperature to afford the product methyl methylphosphonochloridate as colorless liquid (16.19 g, 0.126 mol, 79%).

Distilled water (1.134 ml, 0.063 mol) was added dropwise via syringe to a stirring solution of methyl methylphosphonochloridate (16.19 g, 0.126 mol) and *N*,*N*-diisopropylethylamine (21.95 ml, 0.126 mol) in 100 ml dry CH_2Cl_2. After the solvent was removed under reduced pressure, 100 ml diethyl ether was added and the resulting suspension was stirred vigorously for a couple of seconds. The reaction mixture was filtered and the solvent of the filtrate was removed under reduced pressure. Distillation of the crude product at 0.01 mbar and 120°C oil bath temperature yielded 7.77 g **(8)** (0.039 mol, 61%) as colorless liquid.

^{1}H NMR (250 MHz, CD_2Cl_2): δ_H = 1.63 – 1.56 (m, 6 H), 3.76 – 3.72 (m, 6 H).

^{31}P NMR (250 MHz, $CDCl_3$): δ_P = 24.69 (d, *J* = 22.2 Hz)

Bis(4-methoxybenzyl) Methylphosphonate

(9) 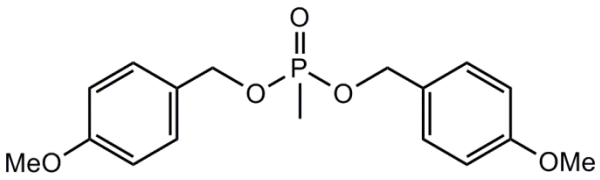

4-Methoxybenzyl alcohol (24.83 ml, 0.200 mol) was added dropwise via syringe to a solution of methylphosphonic dichloride (13.29 g, 0.100 mol) and *N*,*N*-diisopropylethylamine (34.84 ml, 0.200 mol) in 150 ml toluene at 0°C under argon and stirred overnight at ambient temperature. The suspension is filtered to remove the amine salt and the filtrate was subjected to silica gel chromatography using ethyl acetate ($R_f \approx 0$) to afford 18.16 g (0.054 mol; 54%) of a transparent liquid.

^{1}H NMR (250 MHz, CD_2Cl_2): δ_H = 1.42 (d, J = 17.5 Hz, 3 H), 3.80 (s, 6 H), 5.03 – 4.83 (m, 4 H), 6.96 – 6.83 (m, 4 H), 7.38 – 7.23 (m, 4 H).

^{31}P NMR (250 MHz, $CDCl_3$): δ_P = 32.03 (s)

Bis(4-fluorobenzyl) Methylphosphonate

(10)

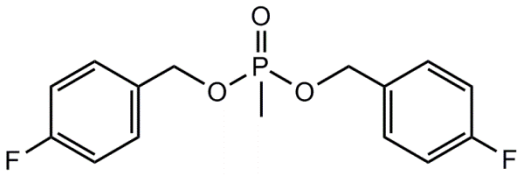

4-Fluorobenzyl alcohol (21.82 ml, 0.200 mol) was added dropwise via syringe to a solution of methylphosphonic dichloride (13.29 g, 0.100 mol) and *N*,*N*-diisopropylethylamine (34.84 ml, 0.200 mol) in 150 ml toluene at 0°C under argon and stirred overnight at ambient temperature. The suspension is filtered to remove the amine salt and the filtrate was then applied to a silica gel column (ethyl acetate, R_f = 0.6) and the desired product isolated yielding 42.46 g (0.136 mol, 68%) of a pale yellow liquid.

^{1}H NMR (250 MHz, MeOD): δ_H = 1.54 (d, *J* = 17.6, 3 H), 5.11 – 4.91 (m, 4 H), 7.17 – 7.02 (m, 4 H), 7.47 – 7.32 (m, 4 H).

^{31}P NMR (250 MHz, $CDCl_3$): δ_P = 32.41 (s)

Diethyl 2,4-Dinitrophenylphosphonate

(12)

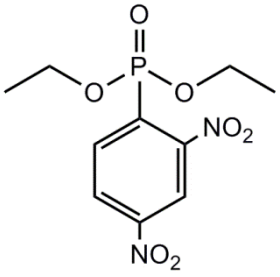

Triethyl phosphite (18.85 ml; 0.110 mol) was added via syringe to a stirring solution of 1-Flouro-2,4-dinitrophenylphosphonate (DNFB) (18.61 g; 0.100 mol) in 50 ml dry benzene under argon. The color turns red immediately and darkens gradually upon triethyl phosphite addition. After 4 h, around 50% of DNFB is converted into **(12)** and excess triethyl phosphite

formed triethyl phosphate as main byproduct. Thus, around 8 ml additional triethyl phosphite was added and the solution was stirred under argon for 2 days at room temperature. The solvent was removed under reduced pressure. The product was purified by silica gel chromatography (diethyl ether, R_f = 0.7) yielding 21.90 g **(12)** (0.72 mol; 72%) as pale yellow powder.

^{1}H NMR (250 MHz, CD_2Cl_2): δ_H = 1.35 (td, J = 0.6 Hz, 7.1 Hz, 6 H), 4.37 – 4.09 (m, 4H), 8.31 (ddd, *J* = 10.9 Hz, 8.4 Hz, 0.3 Hz, 1 H), 8.54 (ddd, *J* = 8.4 Hz, 2.2 Hz, 2.2 Hz, 1 H), 8.68 (ddd, *J* = 4.3 Hz, 2.2 Hz, 0.3 Hz, 1 H).

^{31}P NMR (250 MHz, $CDCl_3$): δ_P = 8.72 (s)

Benzyl Methyl-*^{13}C* Benzylphosphonate

(13)

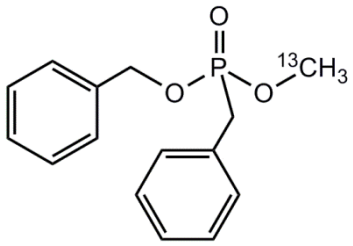

Synthesis was conducted in analogy to **(2)**, but instead, methyl-*^{13}C* iodide was used.

^{1}H NMR (250 MHz, MeOD): δ_H = 3.27 (d, *J* = 20.0 Hz, 2 H), 3.63 (dd, *J* = 7.9 Hz, 145.1 Hz, 3 H), 5.00 (m, 2 H), 7.39 – 7.25 (m, 5 H).

^{31}P NMR (250 MHz, $CDCl_3$): δ_P = 28.72 (d. *J* = 7.0 Hz)

Diethyl Methyl-*d_3* Phosphonate

(14)

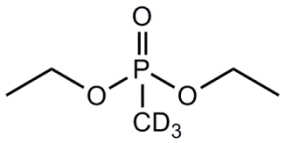

A mixture of triethyl phosphite (4.15 g; 0.025 mol) and methyl-*d_3* iodide (14.5 g; 0.100 mol) is stirred and refluxed for 1 h. **(14)** is obtained quantitatively by distillation at 0.05 mbar and 50°C oil bath temperature as transparent liquid.

^{1}H NMR (250 MHz, CD_2Cl_2): δ_H = 1.27 (td, *J* = 7.1 Hz, 0.4 Hz, 6 H), 4.01 (m, 4 H).

Dimethyl-*[13]C* Methylphosphonate

(15) 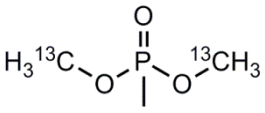

Methanol-*[13]C* (2.18 g; 0.066 mol) was added dropwise via syringe to a stirring solution of methylphosphonic dichloride (3.99 g, 0,030 mol) and *N*,*N*-diisopropylethylamine (86.50 ml, 0.060 mol) in 30 ml dry toluene at 0°C under an argon atmosphere. The suspension was warmed to room temperature and stirred overnight. After removal of the precipitated amine salt, distillation at 10 mbar and 80°C oil bath temperature yielded 2.65 g (0.021, 70%) **(13)** as a transparent liquid.

^{1}H NMR (250 MHz, MeOD): δ_H = 1.53 (d, *J* = 17.5 Hz, 3 H), 3.75 (dd, *J* = 11.1 Hz, 148.0 Hz, 6 H)

8.1.4 Thermal and Mechanical Analysis

Differential scanning calorimetry (DSC) was utilized to monitor changes in T_g upon aging. Samples of approximately 5 mg were taken from the epoxy plaques and analyzed at a heating rate of 10 K/min, i.e. they were not rasped to a powder.

Tensile properties were measured at room temperature using an Instron 6022 testing machine using DIN 53504 Type S2 specimen dimensions. A crosshead speed of 1 mm/min was employed and the average value of 3 specimens (2 mm thick) was taken for each sample. Due to the inevitable fact that multiple grams of fortifier are needed to fabricate a epoxy plaque large enough in size to obtain 3 specimens, only 1 epoxy plaque was prepared for each fortifier concentration and cure process. Thus, the error in mechanical and thermal data is estimated to be +/- 5%. All Tensile measurements were conducted the day after cure to exclude aging. For example, tensile stress for 15 mol% DMMP epoxy is reduced by approx. 1 MPa per day within the first week. Dynamic mechanical thermal analysis (DMTA) data was collected on an Ares LS from Rheometric Scientific by shearing a single cantilever beam from -120 to +150 °C at a maximum strain of $\varepsilon = 10^{-4}$, constant frequency of 1 Hz and temperature ramp rate of 2 K/min.

8.1.5 Line Shape Analysis

^{13}C and ^{31}P line shape analysis was conducted with the program DMFit.[64] All ^{2}H NMR line shape simulations were conducted using the NMR-WEBLAB.[65]

9 Literature

[1] L. E. Nielsen, R. F. Landel, *Mechanical Properties of Polymers and Nanocomposites*, CRC Press, **1994**.

[2] I. M. Ward, J. Sweeney, *An introduction to the mechanical properties of solid polymers*, Wiley, **2004**.

[3] H. H. Kausch, *Intrinsic molecular mobility and toughness of polymers I*, Springer, **2005**.

[4] R. Vieweg, Editors, et al., *Plastics Handbook, Vol. 11: Polyacetals, Epoxy Resins, Fluorine-Containing Polymerization Products, Silicones, Etc. Preparation, Properties, fabrication, and Use*, **1971**.

[5] G. Odian, *Principles of Polymerization*, Wiley InterScience, **2004**.

[6] *Market Report: World Epoxy Resin Market*, Acmite Market Intelligence, **2010**.

[7] M. A. I. Ash, *Handbook of Plastic and Rubber Additives, Second Edition*, Synapse Information Resources, Incorporated, **2005**.

[8] J. Jancar, J. F. Douglas, F. W. Starr, S. K. Kumar, P. Cassagnau, A. J. Lesser, S. S. Sternstein, M. J. Buehler, *Polymer* **2010**, *51*, 3321.

[9] I. Srivastava, N. Koratkar, *JOM* **2010**, *62*, 50.

[10] B. Fiedler, F. H. Gojny, M. H. G. Wichmann, M. C. M. Nolte, K. Schulte, *Compos. Sci. Technol.* **2006**, *66*, 3115.

[11] M. E. Frigione, L. Mascia, D. Acierno, *Eur. Polym. J.* **1995**, *31*, 1021.

[12] J. Spanoudakis, R. J. Young, *J. Mater. Sci.* **1984**, *19*, 473.

[13] H. H. Kausch, P. Beguelin, M. Fischer, *Mech. Compos. Mater.* **2000**, *36*, 177.

[14] Z. Bartczak, A. S. Argon, R. E. Cohen, M. Weinberg, *Polymer* **1999**, *40*, 2347.

[15] Y. S. Thio, A. S. Argon, R. E. Cohen, M. Weinberg, *Polymer* **2002**, *43*, 3661.

[16] O. S. Yordem, A. J. Lesser, *J. Polym. Sci., Part B: Polym. Phys.*, *48*, 840.

[17] J. Yoon, A. J. Lesser, T. J. McCarthy, *Macromolecules* **2009**, *42*, 8827.

[18] W. J. Jackson, Jr., J. R. Caldwell, *Adv. Chem. Ser.* **1965**, *No. 48*, 185.

[19] W. J. Jackson, Jr., J. R. Caldwell, *J. Appl. Polym. Sci.* **1967**, *11*, 211.

[20] W. J. Jackson, Jr., J. R. Caldwell, *J. Appl. Polym. Sci.* **1967**, *11*, 227.

[21] M. Rahman, C. S. Brazel, *Prog. Polym. Sci.* **2004**, *29*, 1223.

[22] J. Mijovic, *J. Appl. Polym. Sci.* **1990**, *40*, 845.

[23] N. Hata, J. Kumanotani, *J. Appl. Polym. Sci.* **1977**, *21*, 1257.

[24] N. Hata, R. Yamauchi, J. Kumanotani, *J. Appl. Polym. Sci.* **1973**, *17*, 2173.

[25] A. S. Zerda, A. J. Lesser, *J. Appl. Polym. Sci.* **2002**, *84*, 302.

[26] A. S. Zerda, A. J. Lesser, *Polym. Eng. Sci.* **2004**, *44*, 2125.

[27] J. Daly, A. Britten, A. Garton, P. D. McLean, *J. Appl. Polym. Sci.* **1984**, *29*, 1403.

[28] K. J. Calzia, A. Forcum, A. J. Lesser, *J. Appl. Polym. Sci.* **2006**, *102*, 4606.

[29] S. J. Guerrero, *Macromolecules* **1989**, *22*, 3480.

[30] A. Nanasawa, S. Takayama, K. Takeda, *J. Appl. Polym. Sci.* **1997**, *66*, 2269.

[31] S. L. Anderson, E. A. Grulke, P. T. DeLassus, P. B. Smith, C. W. Kocher, B. G. Landes, *Macromolecules* **1995**, *28*, 2944.

[32] M. Ueda, *Polym. Eng. Sci.* **2004**, *44*, 1877.

[33] L. Heux, F. Laupretre, J. L. Halary, L. Monnerie, *Polymer* **1998**, *39*, 1269.

[34] B. J. Cauley, C. Cipriani, K. Ellis, A. K. Roy, A. A. Jones, P. T. Inglefield, B. J. McKinley, R. P. Kambour, *Macromolecules* **1991**, *24*, 403.

[35] R. A. Riggleman, J. F. Douglas, J. J. de Pablo, *J. Chem. Phys.* **2007**, *126*, 234903/1.

[36] L. M. Robeson, *Polym. Eng. Sci.* **1969**, *9*, 277.

[37] Y. Maeda, D. R. Paul, *J. Polym. Sci., Part B: Polym. Phys.* **1987**, *25*, 1005.

[38] A. J. Lesser, K. Calzia, M. Junk, *Polym. Eng. Sci.* **2007**, *47*, 1569.

[39] L. M. Robeson, J. A. Faucher, *J. Polym. Sci., Part B* **1969**, *7*, 35.

[40] R. Zorn, *J. Phys.: Condens. Matter* **2003**, *15*, R1025.

[41] J. Perez, J. Y. Cavaille, L. David, *J. Mol. Struct.* **1999**, *479*, 183.

[42] K. L. Ngai, M. Paluch, *J. Chem. Phys.* **2004**, *120*, 857.

[43] G. P. Johari, M. Goldstein, *J. Chem. Phys.* **1970**, *53*, 2372.

[44] G. P. Johari, M. Goldstein, *J. Chem. Phys.* **1971**, *55*, 4245.

[45] K. L. Ngai, R. W. Rendell, A. K. Rajagopal, S. Teitler, *Ann. N. Y. Acad. Sci.* **1986**, *484*, 150.

[46] K. L. Ngai, R. W. Rendell, A. F. Yee, D. J. Plazek, *Macromolecules* **1991**, *24*, 61.

[47] S. P. Brown, H. W. Spiess, *Chem Rev* **2001**, *101*, 4125.

[48] D. D. Laws, H.-M. L. Bitter, A. Jerschow, *Angew. Chem., Int. Ed.* **2002**, *41*, 3096.

[49] H. W. Spiess, *J. Polym. Sci., Part A: Polym. Chem.* **2004**, *42*, 5031.

[50] C. Kins, diploma thesis thesis, MPIP (Mainz), **2009**.

[51] S. K. Kurdistani, T. A. Robbins, D. J. Cram, *J. Chem. Soc., Chem. Commun.* **1995**, 1259.

[52] Y. Liu, M. M. Turnbull, A. A. Jones, P. T. Inglefield, R. P. Kambour, *Solid State Nucl. Magn. Reson.* **1993**, *2*, 289.

[53] P. Bergquist, Y. Zhu, A. A. Jones, P. T. Inglefield, *Macromolecules* **1999**, *32*, 7925.

[54] P. Sutter, C. D. Weis, *Phosphorus Sulfur* **1978**, *4*, 335.

[55] C. F. Kins, D. Dudenko, D. Sebastiani, G. Brunklaus, *Macromolecules* **2010**, *43*, 7200.

[56] A. Pines, M. G. Gibby, J. S. Waugh, *J. Chem. Phys.* **1973**, *59*, 569.

[57] S. R. Hartmann, E. L. Hahn, *Phys. Rev.* **1962**, *128*, 2042.

[58] D. Rovnyak, *Concepts Magn. Reson., Part A* **2008**, *32A*, 254.

[59] K. Schmidt-Rohr, H. W. Spiess, *Multidimensional Solid-State NMR and Polymers*, Academic Press Inc., London, **1994**.

[60] J. G. Powles, J. H. Strange, *Proc. Phys. Soc., London* **1963**, *82*, 6.

[61] J. Herzfeld, A. E. Berger, *J. Chem. Phys.* **1980**, *73*, 6021.

[62] M. J. Duer, *Introduction to Solid-State NMR Spectroscopy*, Blackwell Science Ltd, Oxford, **2004**.

[63] J. Mason, *Solid State Nucl. Magn. Reson.* **1993**, *2*, 285.

[64] D. Massiot, F. Fayon, M. Capron, I. King, S. Le Calve, B. Alonso, J.-O. Durand, B. Bujoli, Z. Gan, G. Hoatson, *Magn. Reson. Chem.* **2002**, *40*, 70.

[65] V. Macho, L. Brombacher, H. W. Spiess, *Appl. Magn. Reson.* **2001**, *20*, 405.

PART II

Structure and Anisotropy of Morphology in Multiblock Copolyimides for Fuel Cell Applications

10 Introduction

10.1 Fuel Cells

10.1.1 Need for Alternative Energy Sources

Energy prices have risen disproportionately in the last decades for a variety of reasons. World population is growing constantly, especially in Asia, which is accompanied by a strong economic growth in these emerging markets leading to increased energy consumption. As prices depend on supply and demand, it is also the limited fossil fuel resources that drive up prices. For example, as oil reservoirs mature, the oil production as well as the cost of new oil discoveries gets more expensive. Producing oil from unconventional resources such as oil sands or attempts to draw oil out of the bedrock of the sea is elaborate and time-consuming. Furthermore, these processes are typically accompanied by severe long-term environmental impacts. Most important, carbon dioxide (CO_2) produced from the burning of fossil fuels is a greenhouse gas, i.e. it absorbs thermal radiation from the planetary surface that is scattered in all directions. This leads to a rise of the average surface temperature which is believed to be the origin of climate change.[1] Despite several attempts in the chemical industry to use carbon dioxide as precursor to chemicals in industrial processes, the total amount used is relatively low compared to the emission through combustion processes.[2, 3] Another approach is to avoid the production of carbon dioxide by using renewable energies from natural sources. The United States have the highest oil consumption where the transport sector accounts for almost 30% of the US greenhouse gas emissions.[4] Hence, it is especially the motor vehicle industry that is, among others, under pressure to pursue technologies that are capable of reducing CO_2 emissions. An over 150 years old technology rendering the zero-emission car possible, is the fuel cell. In combination with sources of renewable energy that allow for the environmentally friendly production of hydrogen, it is a very promising technology and hopefully only a few years away from commercial exploitation.

10.1.2 Basic Principles

It is a very simple chemical reaction that describes the principle of a fuel cell. Chemical energy is converted through the oxidation of a fuel, often H_2, into electricity. The most crucial point is that the oxidation of H_2 and reduction of the oxidant, such as O_2, occur separated (see Figure 10.1). These reactions can be summarized as follows:

Anode: $2H_2 \rightarrow 4H^+ + 4e^-$ (10.1)

Cathode: $O_2 + 4e^- + 4H^+ \rightarrow 2H_2O$ (10.2)

$$2H_2 + O_2 \rightarrow 2H_2O \quad (10.3)$$

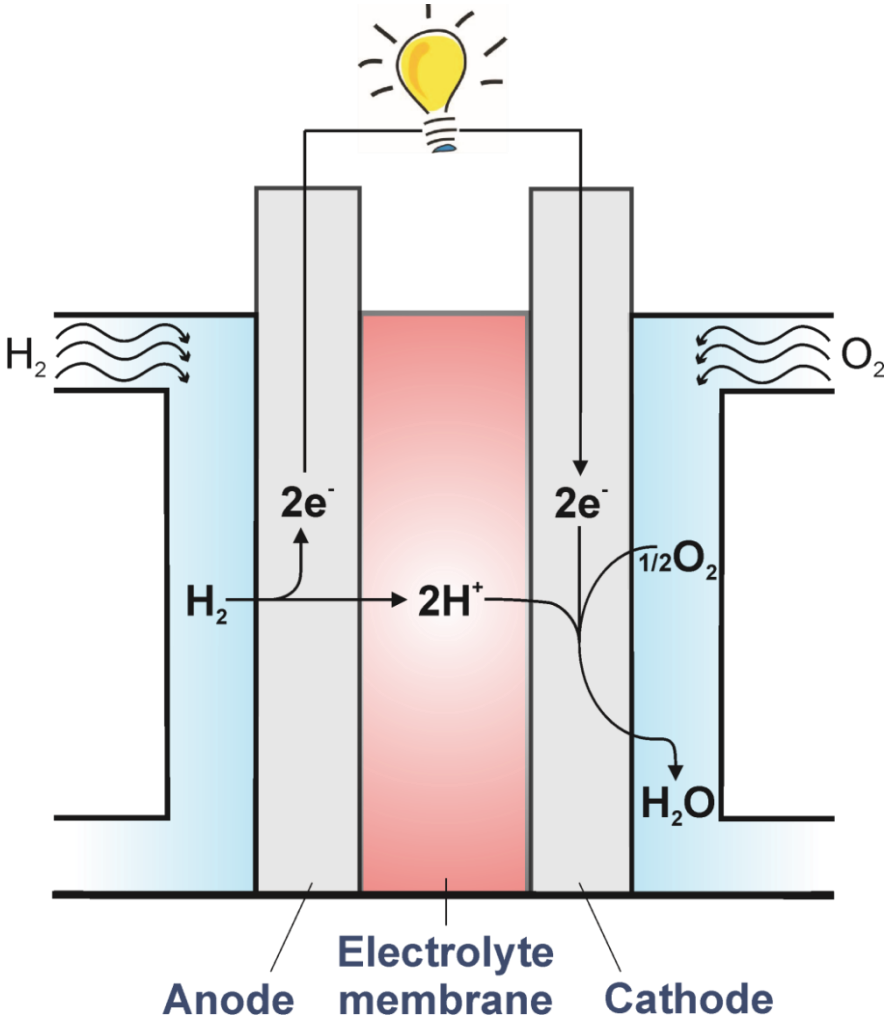

Figure 10.1: Electrode reactions and charge flow for a basic construction of a fuel cell. The electrodes are porous so that the gas can penetrate them.

The electrons flow through an electrical circuit whereas the protons pass through the electrolyte membrane. To increase the reaction rates, highly active metal catalysts dispersed over a porous carbon support are used at preferentially high temperatures. The water producing reaction takes place at the so-called *three-phase contact* of oxygen, electrode and electrolyte only. Increasing the temperature desorbs carbon monoxide (CO) occupying platinum catalyst sites at the anode. This is particularly necessary when the fuel stems from fossil fuel reforming processes (*steam reforming,* see Equation (10.4)). Unfortunately, proton exchange-membrane (PEM) fuel cells do not operate above 100°C, rendering it necessary to use sophisticated, expensive catalysts such as platinum to avoid slow reaction rates.

The advantages of fuel cells are[5]

- **Efficiency**

  Small fuel cells are more efficient than combustion engines, no matter their size.
- **Simplicity**

  No moving parts and a few basic components only.
- **Low emissions**

  A requirement for achieving smog free cities. Strictly speaking, this is only true if hydrogen is produced without carbon dioxide emissions.
- **Silence**

  Particularly important for local power generation and inner-city motorways.

Despite of these advantages the storage and transportation of hydrogen is still one of the main drawbacks. Raw primary fuel is obtained according to

$$CH_4 + H_2O \rightarrow CO + 3H_2 \qquad \text{(endothermic)} \qquad (10.4)$$

$$CO + H_2O \rightarrow CO_2 + H_2 \qquad \text{(exothermic)} \qquad (10.5)$$

It should also be mentioned that fuel cell processing, i.e. the conversion of the primary fuel into pure enough fuel gas required for optimized fuel cell operation, is elaborate and expensive. Reactions (10.4) and (10.5) describe the *steam reforming* process, which is practiced industrially on a large scale,[6] and the *water-gas shift reaction* respectively. Due to the high temperature, where endothermic processes such as steam reforming are favored, the concentration of carbon monoxide in the raw produced gas is still about 15% and has to be reduced to about 10 ppm to circumvent catalyst poisoning.[5] Hence, it is desirable that in the near future hydrogen will be generated by solar cell driven electrolysis of water.

The maximum efficiency of heat engines (e.g. combustion engines, steam/ gas turbines) is given by the Carnot limit

$$\eta = 1 - {}^{T_1}/_{T_2} = W/Q_2 \qquad (10.6)$$

with T_1 the temperature of the cold reservoir and T_2 the temperature of the hot reservoir. W is the work done by the system and Q_2 the heat put into the system.

Similar, for fuel cells we can define

$$\eta = {\Delta G}/{\Delta H} \tag{10.7}$$

with $\Delta G = -237.2\ \mathrm{kJ/mol}$ as the produced electrical energy and $\Delta H = -285.8\ \mathrm{kJ/mol}$ is the heat produced by burning the fuel without fuel cell. These thermodynamic values refer to $T = 25°\mathrm{C}$ and if the product water is condensed to a liquid. The difference $\Delta H - \Delta G = -48.6\ \mathrm{kJ/mol}$ is equal to $T\Delta S$ and will be released to the environment. As $T\Delta S$ is negative at any temperature, the absolute value of ΔG decreases according to

$$\Delta G = \Delta H - T\Delta S \tag{10.8}$$

with increasing temperature (and becomes negative for $T \rightarrow \infty$). This means that η drops for hydrogen fuel cells operating at high temperatures.

Per definition, the electrical work produced is the product of charge and voltage E. The charge moved per one mole of H_2 is 2 mole electrons, resulting in

$$E = -{\Delta G}/{2F} \tag{10.9}$$

with F being the Faraday constant that is the magnitude of electric charge per mole of electrons. With $\Delta G = -237.2\ \mathrm{kJ/mol}$ one obtains $E = 1{,}23\ \mathrm{V}$.[‡]

However, in reality it is found that the actual voltage is considerably smaller, even if no electrons flow (i.e. the open circuit voltage). In addition, the voltage decreases further with increasing current density before the voltage breaks down for very high currents. This behavior is explained by assuming different losses (i.e. irreversible processes) taking place in a working fuel cell.[5] These losses can be summarized as

- **Activation losses**

  Caused by the need to drive the electron transfer at the surface of the electrode.
- **Fuel crossover and internal currents**

  Arises from the gas crossover and electron conduction through the electrolyte.
- **Ohmic losses**

  Mainly due to simple electrical resistance of the electrodes and electrolyte; proportional to the electric current.
- **Concentration losses**

  If the fuel reacts, the concentration very close at the electrode surface will decrease and it takes time until new fuel is delivered, depending on the gas supply system.

[‡] To achieve higher voltages, it is common to connect cells in series (i.e. to stack using so called bipolar plates)

Nevertheless, it turns out that at higher temperature these losses are reduced and thus, a cell may be more efficient even though the theoretical maximum voltage is lower. When drawing a useful current, the voltage is only about 0.7 V.

The heat produced during fuel cell operation can be converted into work using a heat engine, which in turn is subject to the Carnot limit. As described above, it is beneficial to operate fuel cells at high temperature T_H even though the theoretical efficiency decreases for reasons mentioned above. It can be shown that a hypothetical heat engine working between this specific elevated temperature T_H and ambient temperature is capable of producing exactly the amount of electric work that is theoretically lost in the fuel cell due to the increased temperature, keeping in mind that the efficiency of a heat engine according to Equation (10.6) is increasing with increasing temperature. Thus, the combination of both fuel cell and heat engine (i.e. using the waste heat of the fuel cell and putting it into a heat engine) is a perfect thermodynamic engine since both are complementary to each other.[7]

The highest temperature T_C where spontaneous combustion occurs is defined by $\Delta G = 0$. A heat engine working between this limit T_C and ambient temperature has an efficiency that is equal to the efficiency of a fuel cell working at ambient temperature. This illustrates that at both extremes (ambient temperature and T_C) the efficiency of heat engine and fuel cell have to be zero respectively. In the intermediate temperature region, the efficiencies of both energy converters add up to a total efficiency that is constant (Figure 10.2).

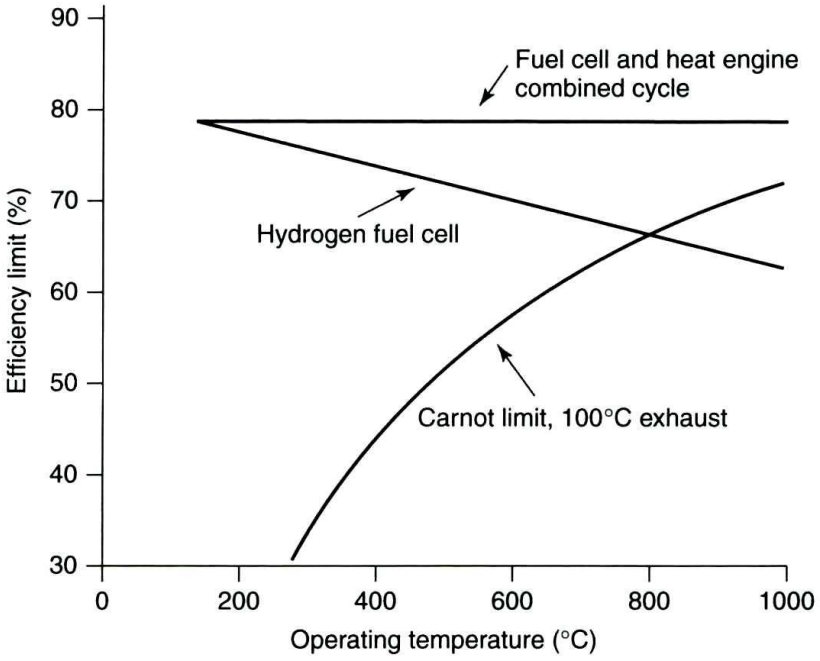

Figure 10.2: Efficiency limits for a hydrogen fuel cell, heat engine and a system of both combined. The maximum efficiency of a fuel cell operated at 100°C is 79%. Figure taken from ref. [5]

10.1.3 Polymer Electrolyte Membranes

The breakthrough for the commercial use of polymer electrolyte fuel cells is ascribed to the invention of Nafion by Walter Grot et al. (DuPont, USA).[8, 9] It is a copolymer based on the monomers tetrafluoroethylene and perfluorovinyl ether (see Figure 10.3) and boosted interest in the fuel cell membrane technology. The perfluorsulfonic acid group is unmatched for applications that demand high membrane stability and ionic conductivity. However, the synthesis of the functional groups presents a challenge. Polymerization is started with radical initiatiors such as perfluoropoeroxides.[10]

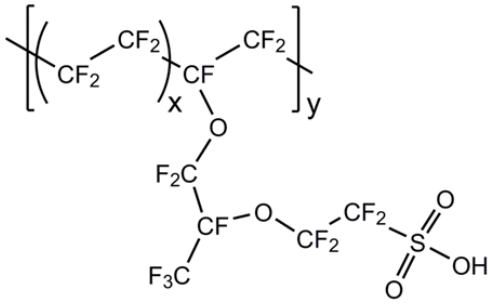

Figure 10.3: Structure of Nafion. x varies between 5 and 10 and y is about 1000.

As can be seen from Figure 10.4, although the most important property of an electrolyte membrane is the proton conductivity, there are several crucial factors also governing the overall performance of the fuel cell. None of them can be omitted when evaluating new membrane materials.

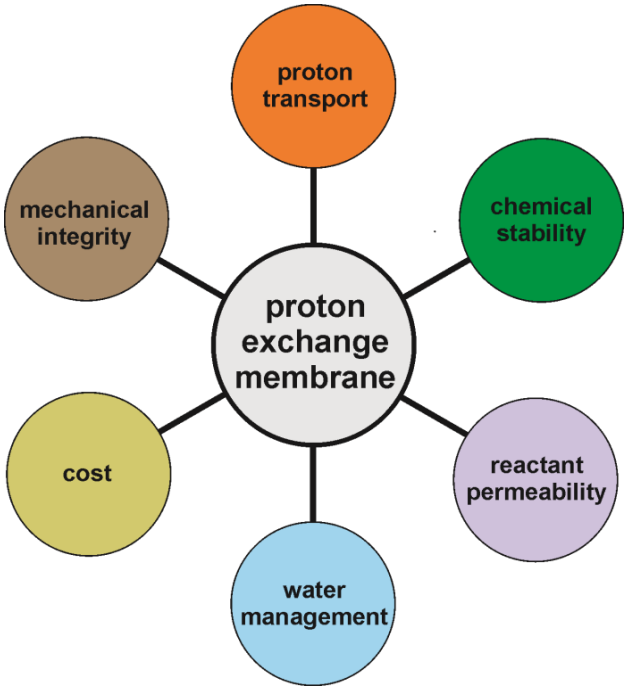

Figure 10.4: Requirements for fuel cell membranes. Figure reproduced from ref. [11]

The good performance of Nafion is closely related to its phase-separated morphology on the nm-scale. The sulfonic acid rich domains form an aqueous network inside the membrane. Under ambient conditions, the SO_3H groups dissociate and become hydrated whereas the hydrophobic polymer phase forms the mechanically stable matrix. Two basic proton transport mechanisms have been proposed: A sequential, concerted mechanism of local excess protons hopping along a hydrogen bond network termed *Grotthus mechanism*[12] and the *vehicle mechanism*, which relies on the physical transport of a vehicle (e.g. water) to shuttle protons. Notably, the real mechanism seems to be more complicated.[13] In general, the higher the degree of hydration, the higher the conductivity of the membrane. For this reason, it is desirable to improve membrane water uptake, which can be enhanced by increasing the ion exchange capacity (IEC), i.e. the number of acidic protons per gram polymer. However, this comes at the expense of mechanical stability. For similar reasons, to avoid rupture and cracks it is not advisable to reduce the membrane thickness below 20 µm. Several strategies have been developed to replace water as proton conducting group in order to operate polymer electrolyte membranes above 100°C (the boiling point of water), comprising imidazole[14] and phosphoric acid based systems.[15]

The hydrophilic-hydrophobic microphase-separated structures have been extensively studied by numerous techniques, including small-angle X-ray scattering (SAXS),[16-20] transmission electron microscopy (TEM)[21-24] and atomic force microscopy (AFM)[25-28]. The famous cluster network model, referred to as Gierke model, based on spherical ionic clusters surrounded by a hydrophobic matrix (“inverse micelles”), has been refuted by Schmidt-Rohr et al.[20, 29] SAXS and small-angle neutron scattering (SANS) techniques are able to determine the distance between the centers of the micelles by investigation of the position of the ionomer or Bragg peak in the diffractograms. On the other hand, determination of the domain size is challenging.[30] On the basis of a careful SAXS data analysis, Schmidt-Rohr et al. proposed a parallel water-channel model, consisting of cylindrical inverted micelles with diameters between 1.8 - 3.5 nm and an average diameter of 2.4 nm at 20 vol% water content. The crystalline regions account for approx. 10 vol%, creating physical crosslinks parallel to the water channels and are considered to be crucial for mechanical properties. The crosslinks are about 2 - 5 nm in thickness and supposed to be approximately cylindrical. Microscopy studies allow for a direct visualization of ionomer membranes but have the disadvantage that these measurements have to be conducted in vacuum (TEM) or are

limited to surface characterization (AFM), providing an incomplete picture of the real morphology.

Although perfluorosulfonic acid membranes have been the benchmark for almost five decades, their industrial application is limited due to several drawbacks, such as low conductivity at low relative humidity ($<$ 50 %RH) or high temperatures ($T >$ 100°C), high price and fuel gas crossover.[20, 31] Lots of efforts have been put into the development of alternative PEMs with particular focus on sulfonated aromatic structures such as sulfonated poly(aryl ether sulfone)s, sulfonated poly(aryl ether)s, sulfonated poly(ether ketone)s and sulfonated polyimides (SPIs).[32, 33] In general, aromatic polymers are inexpensive, easy to modify (e.g. sulfonation) and have good film forming abilities as well as high chemical resistance. Still, for similar ion content, these aromatic polymer membranes nearly always exhibit lower proton conductivity compared to Nafion and, even more crucial, their lifetime is severely limited.[34] The IEC for Nafion is 0.91 meq/g and below the polymers investigated in this thesis. This illustrates that more research is required to overcome the obstacles mentioned above, establishing a competitive hydrogen-carbon based membrane.

11 Motivation and Outline

11.1 Block Copolymers

The IEC is the most important factor influencing both membrane stability and proton conductivity. However, membrane stability and proton conductivity are competing material properties. This is caused by the fact that the higher the degree of sulfonation, and thereby proton conductivity, the larger the brittleness of the membrane in its dry state. In the swollen state, excessive water uptake leads to reduced mechanical strength.[35] To counterbalance the effect of high IEC for obtaining high performance polymers, it is essential to choose appropriate monomers. 1,4,5,8-naphthalene tetracarboxylic dianhydride (NTDA, see Scheme 11.1) is one of the most commonly used dianhydride components, owing to its commercial availability, price and the fact that NTDA can form six-membered imide rings with a higher water stability than the corresponding five-membered moieties.[36] SPI membranes based on 4,4'-binaphthyl-1,1',8,8'-tetracarboxylic dianhydride (BTDA) have been reported to exhibit superior resistance to hydrolysis compared to NTDA-based ones.[22, 37, 38] Sulfonated BTDA is one of the few applied sulfonated dianhydrides in PEMs and was used to enhance microphase separation in sulfonated block copolymers.[39, 40] In general, hydrolysis of the SPI backbone is believed to occur in proximity of sulfonated diamines rather than nonsulfonated ones.[41]

Commercially available 2,2'-benzidinedisulfonic acid (BDSA)[42] is one of the simplest amine building blocks, however the resulting membranes showed poor hydrolytic stability in contrast to more elaborate building blocks based on 2,2' or 3,3'-bis(4-sulfophenoxy)benzidine (BSPOB)[43, 44] and 2,2'-bis(4-aminophenoxy)biphenyl-5,5'-disulfonic acid (*o*BAPBDS).[45] Besides improved polymer backbone stability, these monomers are not prone to ether cleavage as has been found for the aliphatic side chains in 2,2'- or 3,3'-bis(3-sulfopropoxy)benzidine (BSPB).[41] The water stability trends mentioned above can be explained with the basicity of the sulfonated diamine: the electron withdrawing sulfonic acid groups should be located at pendant side chains far from the nitrogen atom forming the imide group. Additionally, it is beneficial to incorporate ether moieties to increase the electron density and hence, inhibit a nucleophilic attack of water at the carbonyl group of the imide group. For this reason, 4,4'-oxydianiline-2,2'-disulfonic acid (ODADS)[46] performs better than BDSA although the resulting membranes are less stable than BSPOB or *o*BAPBDS.

The aim of this investigation is to elucidate the morphology and its anisotropy for a given block copolyimide and optimization of the chemical structure and long-term stability. NTDA,[24, 47, 48] 2,2-bis(4-aminophenyl)hexafluoropropane (BAHF)[27, 35, 49, 50] and ODADS[38, 40, 46, 51] were chosen as dianhydride, diamine and sulfonated diamine, respectively, since these building blocks have proven to exhibit good performance and are readily available. It is noted that post-sulfonation reactions, i.e. treatment of the polymer with sulfonating agents, are undesired due to a lack of control over the degree of functionalization. Moreover, they potentially lead to degradation and side reactions.[34]

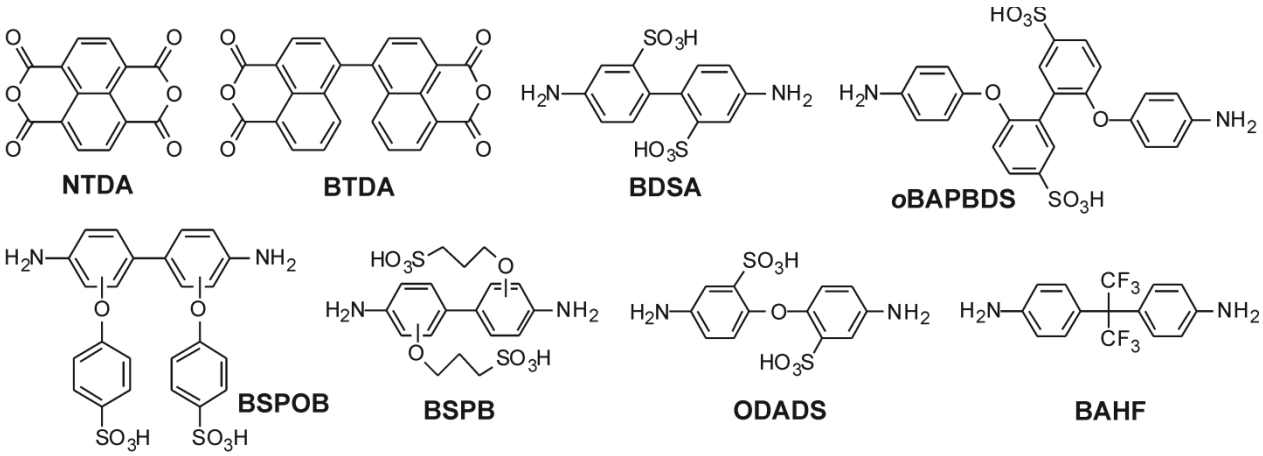

Scheme 11.1: Chemical structure of various dianhydrides and diamines. In this work, NTDA, ODADS and BAHF were used to form block copolymers.

It is widely accepted that in most cases block copolymers show better fuel cell performance than their random counterparts, especially at low relative humidity.[32] In principal, it should therefore be possible to control the specific self-organization by varying the relative volumes and chain lengths of the hydrophilic and hydrophobic blocks. Furthermore, the procedure of film preparation is crucial and complex, providing an additional handle to impact conductivity performance.[52] Recent studies have shown that anisotropic membrane swelling and different levels of conductivity in through-plane and in-plane directions point towards anisotropic structures.[35, 40, 47, 50] Notably, through-plane conductivity measurements are not straightforward, mainly due to impedance contributions from the large interfacial region between the polymer membrane and the electrodes. Thus, care has to be taken if conductivity values are compared to those measured through-plane. [23, 33, 50, 53]

11.2 Characterization Methods

In this thesis, the aim is to characterize the relationships between water diffusion coefficients obtained via ^{1}H pulsed-field-gradient (PFG) NMR diffusometry, the alignment of the proton conducting channels using ^{2}H NMR spectroscopy on the basis of adsorbed $^{2}H_2O$, relative humidity and block copolymer length. In contrast to most other techniques, PFG NMR is a noninvasive technique and thus does not rely on complex theoretical models or assumptions.[54-58] To assess the proton transport anisotropy, ^{1}H PFG NMR experiments were employed to different membrane orientations with respect to the applied magnetic field gradient. It is important to note that the proton conductivity and water diffusion coefficients do not necessarily correlate with each other, although they both depend on the mobility of water molecules. The mobility of water is not only a function of the local environment, but also of the percolation of ionic domains, which provides diffusion pathways through the membrane. Conductivity is a macroscopic effect, whereas the length scale probed by ^{1}H PFG NMR is on the order of a few hundred nanometers, depending on the experimental setup. Orientational anisotropy in a variety of systems has previously been elucidated with success by ^{2}H NMR spectroscopy.[59-63] Considerable work related to the combination of ^{1}H PFG NMR and ^{2}H NMR has been reported in recent years by Madsen and coworkers.[64-66] ^{2}H NMR experiments take advantage of the fact that the electric field gradients for the ^{2}H nucleus are not completely averaged to zero through the non-isotropic molecular reorientation of the deuterated water molecule.[67] This manifests itself in a characteristic splitting of the isotropic chemical shift related to the specific orientational anisotropy. In case of PEM membranes, it is morphology induced partial ordering of absorbed D_2O molecules that allows for the determination of the symmetry axis of diffusion.[68-70] For example, in membranes with parallel hydrophilic channels, the symmetry axis coincides with the channel direction. In a hypothetical membrane, where the morphology is composed of stacked lamellar layers, the symmetry axis is perpendicular to the layer plane. Thus, once the symmetry axis is found, additional information is desirable for determining the predominant nature of the morphology (e.g. lamellar layers, cylindrical channels, spheres etc.) which can be achieved using TEM or AFM. This specific combination of methods, including NMR and scanning probe techniques, provides a direct connection between orientation and transport, setting up a foundation for the rational design and evaluation of the next generation PEMs.

12 Results and Discussion

12.1 Synthesis and Characterization

Multiblock co-SPIs derived from NTDA, ODADS and BAHF were synthesized by a two-pot method as described in Scheme 12.1. Anhydride end-capped sulfonated oligomers (hydrophilic) and amine end-capped hydrophobic oligomers were synthesized separately in two flasks. Subsequently, the hydrophobic solution was carefully poured into the hydrophilic solution and both mixed thoroughly. Care was taken to conduct this transfer quantitatively in order to obtain multiblock copolymers with high molecular weights. The reaction mixture was kept at 180°C for at least 22 hours to ensure full conversion and imidization. Random copolyimide **(r)** and fully sulfonated polyimide **(f)** (i.e. polyimide derived from ODADS and NTDA only) were prepared in a similar fashion by a one-step procedure. A series of block-sulfonated copolyimides with different block lengths was synthesized. The length of the hydrophilic (x) and hydrophobic (y) segments was controlled by varying the ratio of NTDA to diamines and is equal (x = y) for all multiblock copolymers. In this thesis, x = y = 5, 10, 20 and 50. The corresponding polyimides are termed **(5)**, **(10)**, **(20)**, and **(50)**, and their molecular weights and IEC are listed in Table 12.1. To be able to assess the effect of varying block lengths on morphology and proton conductivity, the IEC was held constant for all copolymers. BAHF was chosen as nonsulfonated diamine, due to the good solubility of the resulting hydrophobic oligomers in *m*-cresol.

All the prepared polymers showed relatively high molecular weight and were readily soluble in DMF or DMSO, except block copolyimide **(50)** with the highest block length. It is reasonable to conclude that the long hydrophobic segments in multiblock copolyimide inhibit dissolution in polar aprotic solvents since all hydrophobic oligomers were also insoluble in DMF or DMSO, irrespective of chain length. Thus, membranes of **(50)** were cast from a transparent solution in *m*-cresol. All multiblock co-SPI membranes and the random copolyimide membrane were transparent, flexible, tough and ductile, except membrane **(50)**. Although no reliable molecular weight data is given for **(50)** due to solubility problems in DMF, the resulting film is as flexible and ductile as the other membranes, suggesting high molecular weight.

Absolute molecular weight values for the hydrophilic oligomers were three times higher than expected (Table 12.1, e.g. M_n = 11.000 g/mol for the sample with theoretically 5 repeat

units; the calculated value is around 3.400 g/mol). This difference might originate from the formation of a significant amount of aggregates in the GPC eluent DMF, although the film dissolves to give optically clear solutions in DMF.[71] Indeed, dynamic light scattering experiments of polyimide **(f)** in DMF (data not shown) revealed significant aggregates through the presence of polymer particles with hydrodynamic radii exceeding 100 nm. However, this does not prove the presence of aggregates in the GPC column, as such aggregates can break up during the gel permeation experiment through shearing forces in the column. However, conventional gel permeation chromatography never affords absolute values. Molecular masses are usually referenced relative to a standard with a known molecular weight. The molecular weight of hydrophilic (sulfonated) oligomers was approximately proportional to the calculated number of repeat units, proving good control over the block length. Hydrophobic oligomers were not soluble in DMF, hence no GPC data is given.

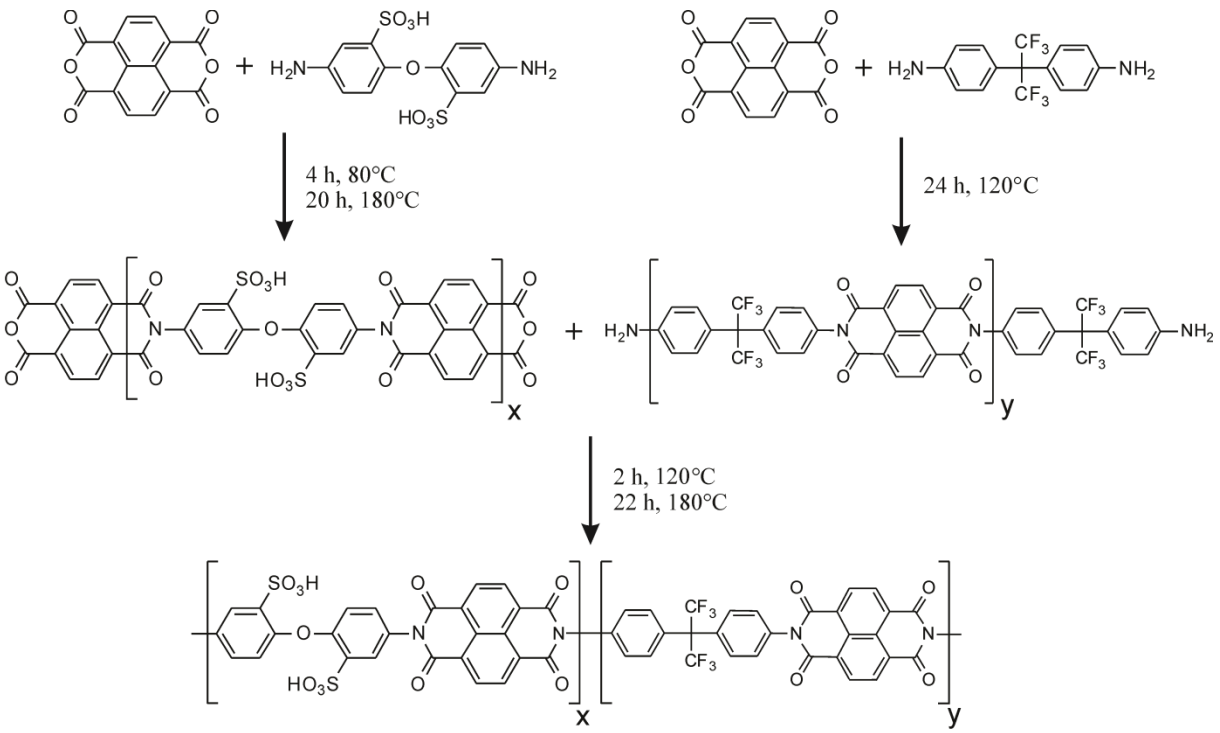

Scheme 12.1: Reaction pathway for synthesis of multiblock co-SPIs.

Attempts to obtain nonsulfonated oligomers resulting from the reaction of NTDA with ODA did not prove successful as they did not form a clear solution in *m*-cresol. Instead, the reaction mixture was opaque and addition of the hydrophilic oligomers resulted in multiblock copolyimides with low molecular weights. The obtained films were opaque and

brittle. This is in accordance with previous reports, where hydrophobic blocks derived from NTDA and other nonsulfonated diamines with aryl ether linkages did not form a clear solution either.[49, 50] Notably, it was possible to obtain random copolyimide derived from the polycondensation of NTDA, ODADS and ODA with high molecular weight that is soluble in *m*-cresol.

The IECs and molecular weights of the copolyimides are listed in Table 12.1, together with random co-SPIs and fully sulfonated SPI **(f)** for comparison. The calculated IEC for all polymers except **(f)** is 1.73 meq/ g. Experimental values obtained by conventional titration were only slightly lower and additional ^{1}H NMR data of proton exchanged membranes showed no residual TEA signal intensity, pointing towards quantitative substitution of TEA.

Table 12.1: Molecular weight and IEC of sulfonated polyimides. **(50)** is opaque and not soluble in DMF.

code	x:y	M_n (kg/mol)[a]	M_n (kg/mol)[b]	M_w (kg/mol)[b]	M_w/M_n[b]	IEC (meq/g)[c]
r	-	-	93	269	2.9	1.64
5	5:5	11	94	305	3.2	1.66
10	10:10	23	90	274	3.0	1.67
20	20:20	37	67	321	4.8	1.70
50	50:50	81	-	-	-	1.71
f	-	-	45	128	2.8	3.21

[a] refers to sulfonated oligomers.
[b] refers to sulfonated multiblock copolymers.
[c] obtained by titration. Theoretical value is 1.73 meq/g, except for **(f)** (3.37 meq/g)

Water uptake, and thereby level of hydration, is a crucial factor determining the membrane's properties. As already mentioned, proton conductivity increases with increasing water content and density of acidic protons.[72] However, mechanical strength decreases with increasing IEC, limiting the practicable amount of water uptake.[35] Block copolymers are believed to be potentially superior to their random counterparts in maintaining membrane stability at a higher level for a given water uptake.[32] Table 12.2 lists the water uptake for block copolyimides and the corresponding random polyimide. Water uptake was lowest for random copolyimide and increased steadily with increasing segment length. Membrane **(5)** has the lowest swelling of all membranes and water uptake (WU) is marginally higher than for **(r)**, whereas WU rises tremendously for **(10)**. This suggests that a block length of 10 is necessary to induce significant microphase separation. All membranes in this study exhibited anisotropic membrane swelling with larger through-plane swelling Δt

than in-plane swelling Δl, i.e. $\Delta_t/\Delta_l = \Delta_{t/l}$ is larger than 1. This finding has been attributed to polymer chain alignment in the plane direction of the membrane, which is further supported by the rigid structure of aromatic polyimides.[40, 50]

Table 12.2: Water uptake and anisotropy of membrane swelling.

code	WU (%)	λ^a	Δt	Δl	$\Delta_{t/l}$
r	40	12.8	0.21	0.14	1.5
5	41	13.1	0.21	0.08	2.6
10	57	18.3	0.30	0.17	1.8
20	58	18.6	0.55	0.13	4.2
50	69	22.2	0.54	0.19	2.8

[a] λ refers to the number of water molecules sorbed per sulfonic acid group.

Thermal stability of the membranes in their protonated form was investigated by TGA. All polymers exhibited the typical three-step degradation process. The first weight loss up to 280°C was due to the loss of absorbed water and the second weight loss up to 500°C ascribed to desulfonation of the polymer backbone. Above this temperature, the polymer backbone started to decompose (formation of CO_2) and evaporated. Furthermore, the data obtained for random and block copolyimides was very similar, suggesting that the morphology does not have a high impact on thermal stability.[39, 40] As expected for sulfonated polyimides, no glass transition temperature was detected up to 200°C by DSC measurements. It is worth to mention that DSC and TGA measurements are only of limited explanatory value for fuel cell membranes, since highly reactive radicals are formed at the electrodes that are not present in conventional DSC or TGA experiments. [73] Thus, to obtain reliable data, real fuel cell tests have to be conducted that mimic the oxidative conditions at the cathode (O_2), the reducing conditions at the anode (H_2) in combination with an aqueous acidic environment and an active catalyst located at the electrode.

12.2 Morphology

Figure 12.1 shows the TEM bright field images of samples **(r)**, **(20)** and **(50)**. As can be clearly seen, spherical clusters are uniformly dispersed throughout the membranes, pointing towards a channel like morphology rather than a layer-like structure. The domain size increases proportional to increasing block length. For **(r)** it is only approx. 5 nm, whereas for **(20)** the average domain size doubles in size to about 10 nm. Sample **(50)** exhibits the largest

microphase-separated structures with roughly 30 nm in size. This is related to the increasing block length, facilitating the clustering of larger hydrophilic and hydrophobic domains. Importantly, TEM images are taken under high vacuum conditions and may not represent the actual morphology in ambient conditions accurately. For this reason, AFM images recorded under ambient conditions in tapping mode have been recorded (cf. Figure 12.1a,c,e). They basically confirm the information obtained by TEM, although the domain size appears to be somewhat larger than in TEM; namely the microphase separation increases with increasing block length. Most likely, the apparent increase in domain size for AFM images is due to the water induced swelling of hydrophilic domains. Water from the air is absorbed and incorporated into the hydrophilic channels, extending their diameter.

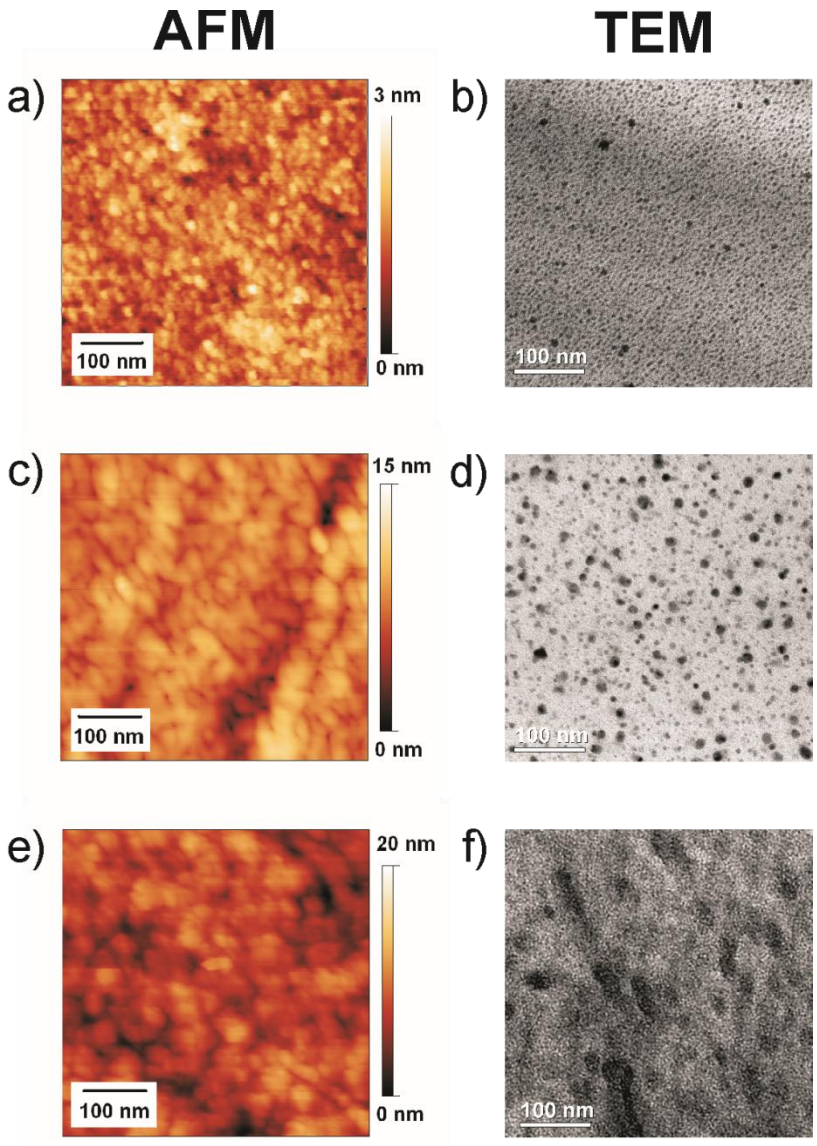

Figure 12.1: AFM and TEM images of (a,b) **(r)**, (c,d) block co-SPI **(5)** and (e,f) block co-SPI **(50)**. TEM and AFM measurements were conducted by Ingo Lieberwirth and Esha Sengupta respectively.

Figure 12.2 shows a conventional bright field TEM image and its corresponding electron energy loss (EELS) spectrum. Besides the observation of phase separation on the nanometer scale (cf. Figure 12.1), there is also a superordinate spherical morphology on the micrometer scale. According to the sulfur map, hydrophobic clusters of roughly 1 µm in diameter are embedded in a matrix of mainly ionic character. This explains the opaque appearance of membrane **(50)**, because visible light is easily scattered on these density inhomogeneities whose size are in the order of the visible light's wavelength. No distinct morphology on the micrometer scale can be found for the other membranes. Accordingly, these membranes appear transparent to the eye. The opaqueness of **(50)** is not related to the formation of large crystallites in the membrane since all solid-state $^{13}C\{^{1}H\}$ CP-MAS spectra are virtually identical for all membranes (data not shown). A significant narrowing of the ^{13}C resonances would be expected for increased crystalline regions.

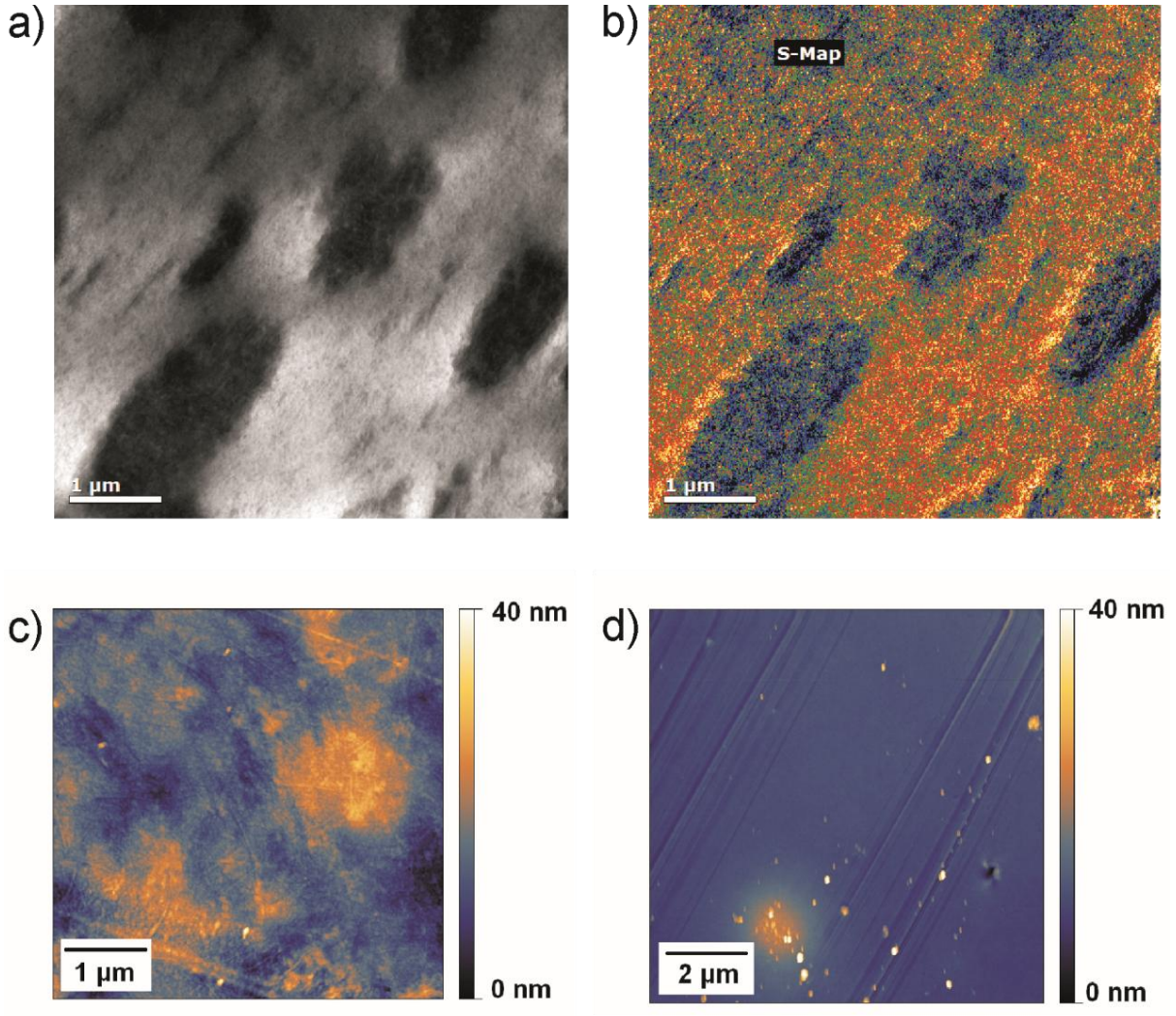

Figure 12.2: TEM images of **(50)**. b) Sulfur map, obtained by EELS, of the same area that is shown in a). Yellow indicates high sulfur content, corresponding to ionic domains. A comparison of AFM images of c) **(50)** and d) **(r)** clearly shows that the superordinate morphology is only present for **(50)**.

12.3 ^{1}H MAS NMR

The question arises if enhanced water uptake with increasing block length is only due to the growing size of hydrophilic domains, or if the quality (i.e. the ionic character) of hydrophilic domains in the membrane is also growing. Protons involved in hydrogen-bonded structures often exhibit well-resolved ^{1}H resonances and can be identified by ^{1}H MAS NMR.[74] Typical evidence of strong hydrogen bonding is a high-frequency shifted ^{1}H chemical shift.[75-77] It is reasonable to conclude that with increasing ionic character of hydrophilic domains, the hydrogen bonding also becomes stronger. Figure 12.3 shows a series of solid-state ^{1}H MAS NMR spectra of different SPI membranes. All samples were dried at 100°C in vacuo for two days before the measurements. The ratio of the area under the respective peaks (i.e. acidic proton and polymer backbone) is close to the theoretical value of 1:11 expected for a water free polymer. Thus, water molecules were effectively removed from the membranes. Notably, without drying of the membranes a very intense and broad dominating proton resonance of free water at around 6.8 ppm was detected.

As a result of enhanced hydrogen bonding, the ^{1}H chemical shift of the acidic protons is shifted to higher values with increasing block length (cf. spectra in Figure 12.3c), pointing towards better phase separation for longer block lengths. The lowest shift was found for random copolyimide **(r)** ($\delta_{\mathrm{iso}} = 10.70$ ppm at 320 K) and the highest shift for fully sulfonated polyimide **(f)** ($\delta_{\mathrm{iso}} = 11.38$ ppm). Sample **(f)** can be considered as the case of infinite, perfect ionic domains, as there are no hydrophobic sequences present. Hence, its SO_3H chemical shift is expected to be the highest that can be observed for this kind of SPI, as the ionic interactions should be maximal. Regarding the block co-SPIs, compound **(50)** exhibited the highest δ_{iso} of 10.93 ppm. The fact that this is substantially lower than the value found for membrane **(f)** demonstrates that even for long blocks, the phase separation between ionic and hydrophobic domains is far from being sharp and well-defined. Figure 12.4 shows the chemical shift of all membranes as a function of temperature. As can be seen from Figure 12.3a, at low temperature no distinct intensity maxima are observed for the acidic protons and chemical shift positions could only be extracted by deconvolution of the experimental spectra. This leads to an error bar of the chemical shift values for random and block co-polyimides, which is estimated to be ±0.1 ppm. For fully sulfonated polyimide the error is ±0.3 ppm. At higher temperatures, the chemical shift moved towards lower ppm. This is a direct result of weaker effective hydrogen bond strength due to thermal motion.

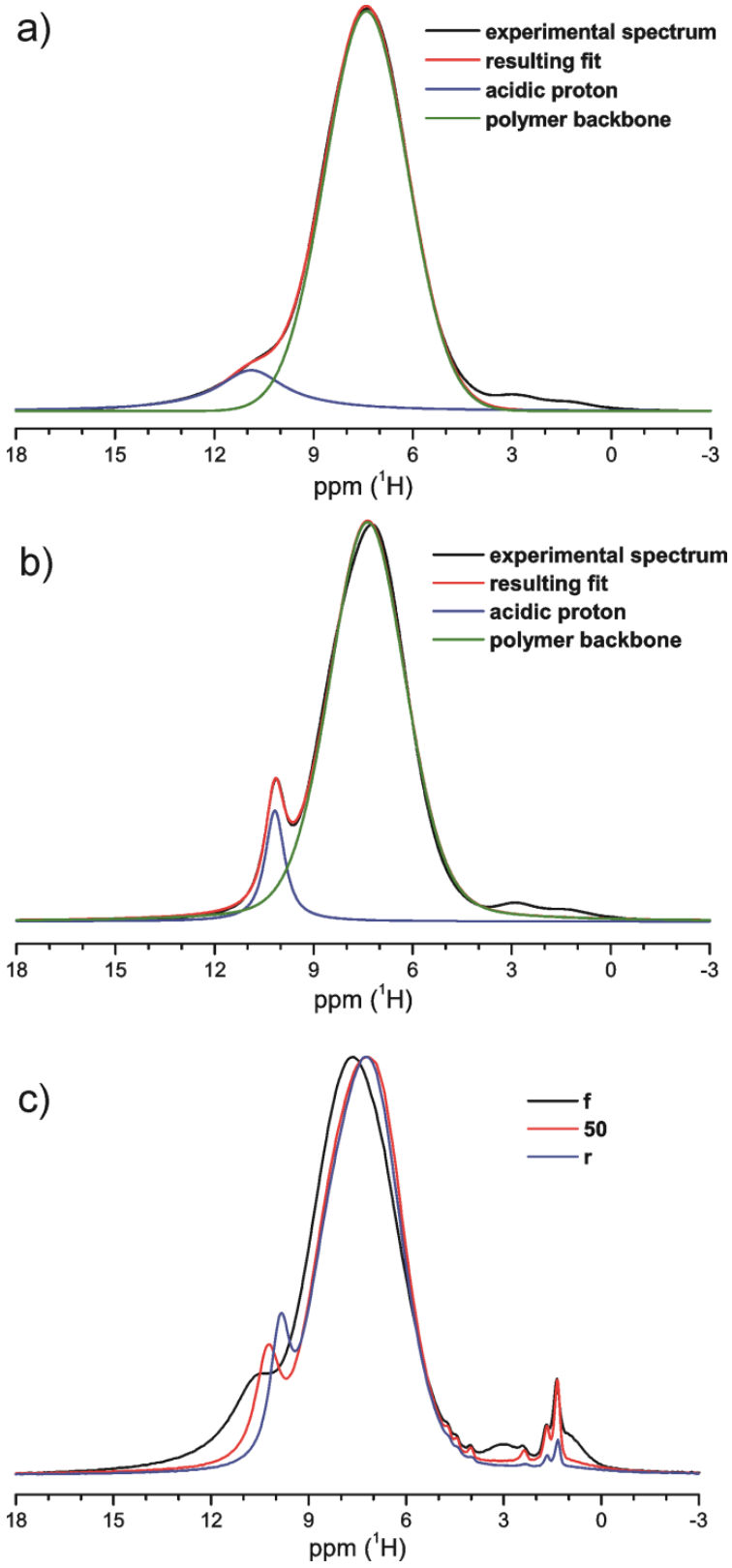

Figure 12.3: Deconvolution of ^{1}H MAS NMR spectra of dried **(20)** at a) 320 K and b) 400 K. The resonance of the polymer backbone does not narrow significantly with increasing temperature, whereas a distinct proton resonance is visible for the SO_3H proton at 400 K. The fit is very accurate, so that the underlying experimental spectrum (black) is hardly visible. c) Comparison of ^{1}H MAS NMR spectra of fully sulfonated PI **(f)**, block co-SPI **(50)** and random copolyimide **(r)** at 400 K. Clearly, the chemical shift of the acidic proton depends on the type of membrane. For all membranes, unexpected intensity in the low-ppm region at around 3 ppm was detected. The signal may originate from side products that are formed during the polycondensation reaction, chain ends or residual solvent (*m*-cresol, DMSO). Except for **(f)**, the amount of this intensity is well below 3%.

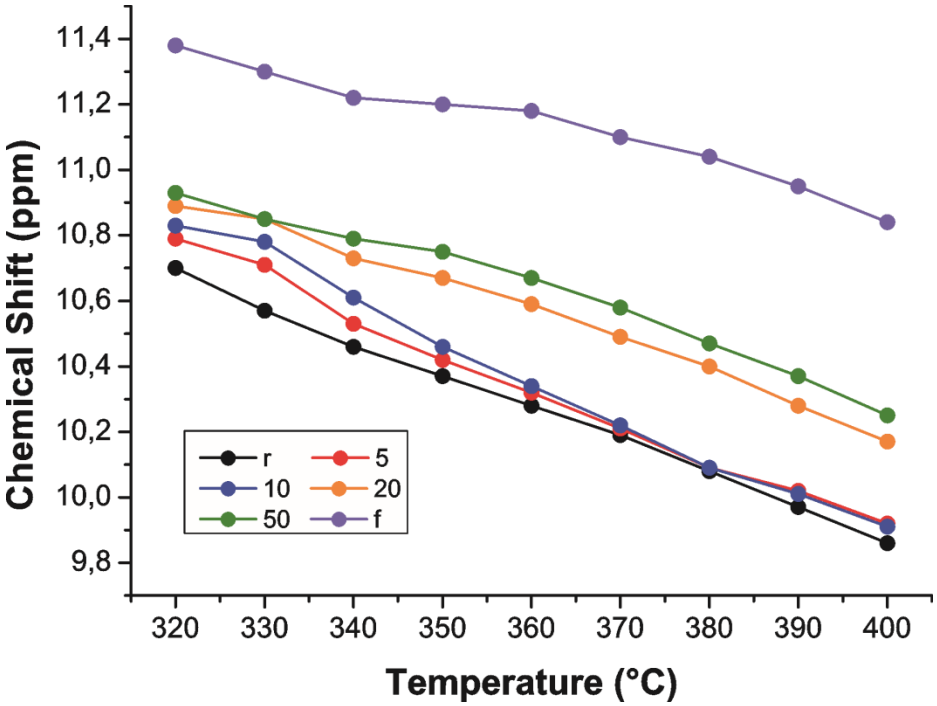

Figure 12.4: ^{1}H Chemical shift of the acidic SO_3H proton in dry SPI membranes plotted vs. temperature. The chemical shift of the fully sulfonated PI membrane is substantially larger than for block co-SPIs, despite the estimated error of +/- 0.3 ppm for **(f)**.

Nevertheless, **(f)** maintains the highest shift, followed by the block SPI **(50)** with the longest block length. Notably, ^{1}H double quantum (DQ) filtered MAS NMR spectra of dry membranes using one rotor period (50 µs) excitation/ reconversion period removed the SO_3H proton resonance that is present in conventional ^{1}H single pulse MAS NMR experiments. This is ascribed to the DQ filter removing resonances due to weak ^{1}H-^{1}H dipolar couplings (e.g. due to rapid motional averaging) and typical for sulfonated aromatic polymers, illustrating the high mobility of the acidic protons that are responsible for conduction.[75, 76] DQ refers to the coherence order created as a result of dipolar interactions between two (or more) coupled nuclei.

The line width of the acidic protons as a function of temperature can be analyzed using the Arrhenius Equation. In the motional narrowing limit the temperature dependence of the effective transversal relaxation time T_2^* for the acidic proton is sensitive to protons hopping between different sites. This limit is defined by the exchange rate Ω, which has to be much larger than the frequency difference between the sites undergoing exchange. Thus, proton mobility on the microscopic scale can be probed by determining proton hopping activation energies according to

$$\Omega \cong \Delta\nu = {}^{1}/_{\pi T_2^*} = \Omega_0 e^{-\frac{E_A}{RT}} \quad (12.1)$$

$$-\ln(T_2^*) = \ln(\pi\Omega_0) - \frac{1}{T}\frac{E_A}{R} \quad (12.2)$$

where $\Delta\nu$ is the line width of the resonance and T_2^* is the effective transverse relaxation time.[77, 78] The aromatic proton resonance shows an almost invariable line width for the whole temperature range, implying that the motions of polymer chains do not increase significantly until 400 K.

Figure 12.5 displays the plot of $-\ln(T_2^*)$ for SO_3H in **(20)** as a function of temperature. The slope of the line of best fit allows determining an activation energy of ≈ 15 kJ mol^{-1}. The extracted values for the other samples are listed in Table 12.3. The activation energy can be observed to be in the range of 12 to 16 kJ/mol for all samples.

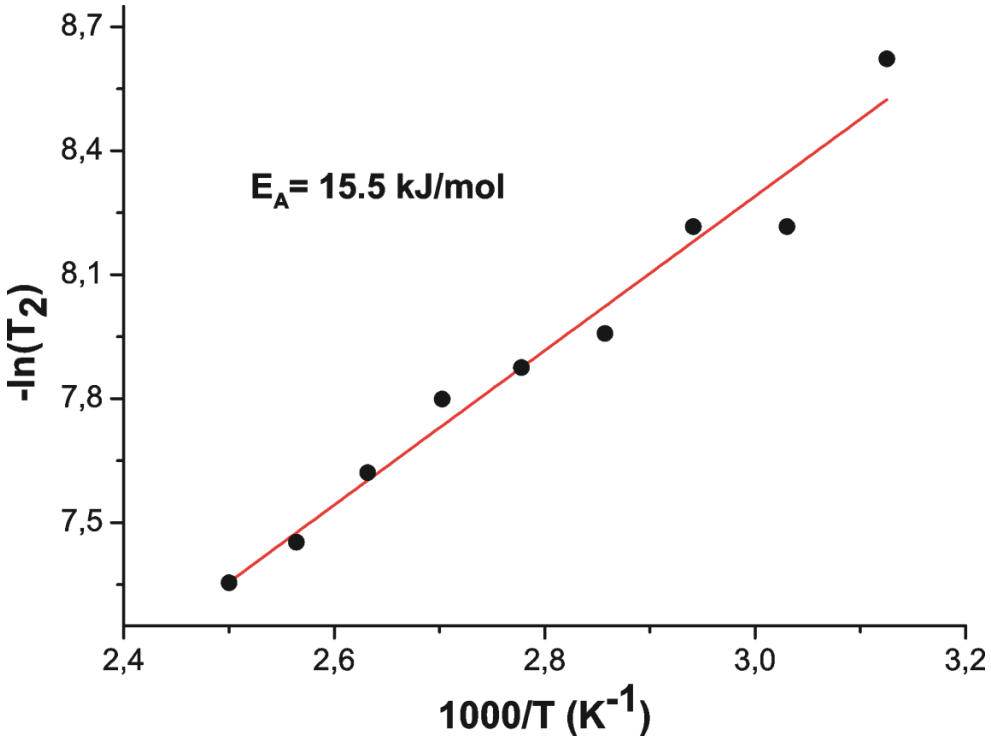

Figure 12.5: Arrhenius plot of the temperature dependence for the relaxation time T_2^* of the sulfonic acid ^{1}H resonance for membrane **(20)**.

Table 12.3: Activation energy for proton mobility in SPIs obtained by linear fitting to the Arrhenius Equation. The given error is equal to the standard deviation of the activation energy value.

code	r	5	10	20	50	f
E_A (kJ/mol)	15.4 ± 0.8	12.9 ± 1.5	12.8 ± 1.0	15.5 ± 1.0	14.0 ± 0.6	12.4 ± 1.2

Unexpectedly, **(20)** and **(50)** tend to have higher activation energies than **(5)** and **(10)**, even though the phase separation (i.e. the ionic character) is better for SPIs with the higher block lengths (cf. Figure 12.4). This issue is discussed further in the ^{1}H PFG NMR section, where it is also shown that the obtained activation energy for **(50)** is just an apparent value, which is the result of a superposition of two distinct proton environments. The observed activation energy range is slightly lower than the value found in dehydrated Diels-Alder material (≈ 18 kJ mol^{-1}),[76] dried sulfonated poly(ether ether ketone)s and Nafion[75]. Importantly, for **(f)** an initial narrowing of the line width with increasing temperature is observed, followed by a plateau value of approx. 1100 Hz at 370 K. This is the inherent line width that is no longer dominated by anisotropic interactions that could be averaged by increasing temperature. Hence, only data from the initial part of the slope (320 K to 370 K) was used to calculate the activation energy.[77] It has to be pointed out that the determined NMR activation energies provide information about the local environment of the acidic protons only, like those associated with the Grotthus hopping mechanism due to the dry state of the membrane. Hence, from this data alone, no direct conclusions can be drawn about the proton conductivity since this is a macroscopic property and strongly depends on the specific morphology.[77]

12.4 Proton Conductivity

As mentioned above, proton conductivity is extremely sensitive to the relative humidity of the environment and increases with increasing water content of the membrane. As presented in Figure 12.6, the multiblock membranes show good proton conductivities that approach the values of Nafion at high humidity. Above 60% RH, random and block co-SPIs exhibited approximately the same conductivity (> 0.05 S/cm at 90% RH). At low RH conditions, the performance strictly depends on the block length with the longer blocks having the better conductivity values. For example, at 5% RH the conductivity of **(50)** is more than 12 times higher than that of the random copolyimide ($4.63 \cdot 10^{-6}$ S/cm vs. $3.65 \cdot 10^{-7}$ S/cm). This is most likely related to an enhanced microphase separation for membranes with longer blocks (see Figure 12.1 and 12.4). There are two ways how optimal phase separation can lead to a better proton transport: i) Either through well-developed ionic percolation pathways within the hydrophobic matrix and/or ii) through higher water uptake for a given RH and temperature. The water uptake for samples **(r)** and **(50)** at 50°C can be seen in Figure 12.7.

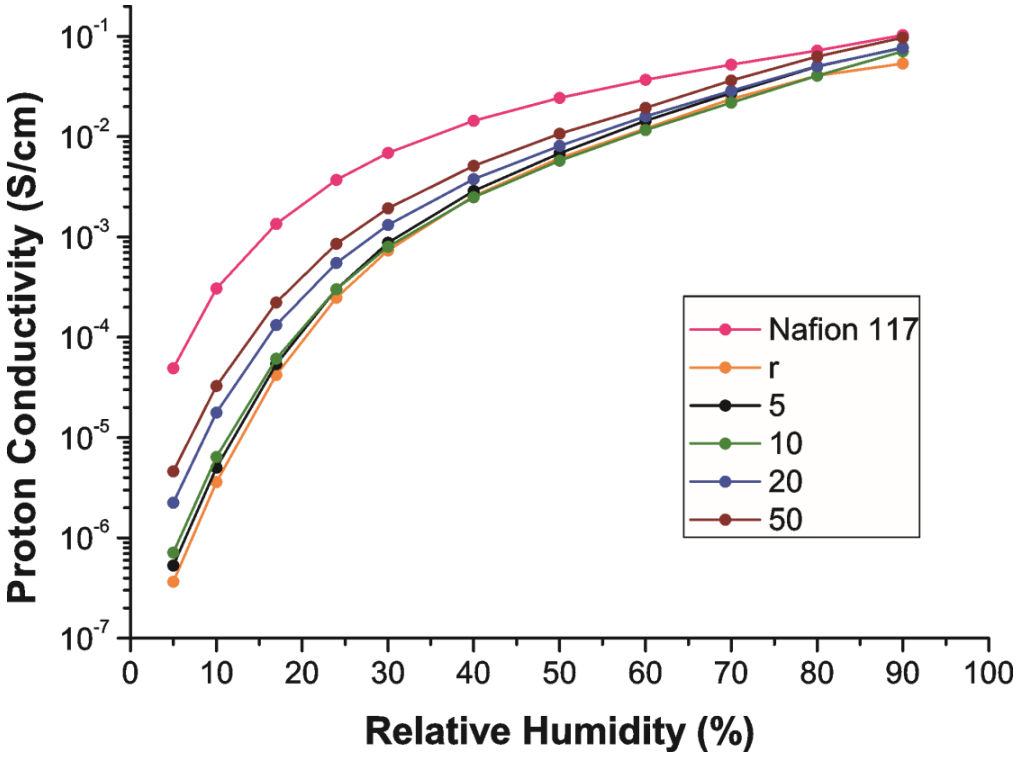

Figure 12.6: Proton conductivity of the SPI membranes and Nafion 117 as a function of relative humidity measured at 50°C.

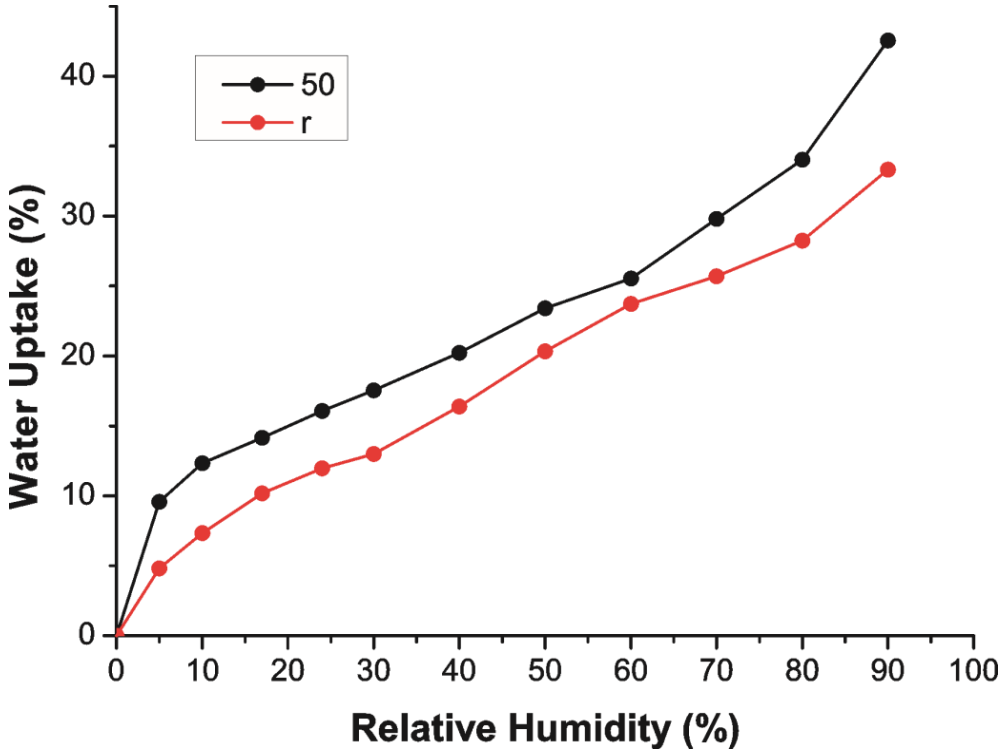

Figure 12.7: Water uptake of block co-SPI **(50)** and random SPI **(r)** at 50°C. The water uptake at 0% RH was determined after storing the membrane at 100°C in vacuo overnight. The respective RH was adjusted with the help of a climatic chamber.

The state of the membrane after being kept under vacuum at 100°C overnight was defined as 0% water uptake. At 5% RH, compound **(50)** adsorbs almost twice the amount of water compared to **(r)**. At higher relative humidity, the water uptake of both membranes grows in parallel with each other, leading to a smaller *relative* difference. This shows that the relative difference in water uptake of the block membranes compared to the random membrane is highest at low RH. This is exactly the range where the strong dependence of conductivity on block length is observed and characteristic for most sulfonated block copolyimides.[24, 27] The better performance in conductivity for block copolymers is therefore due to enhanced water absorption under dry conditions. However, a significant contribution of percolation effects on the enhanced proton conductivity for block copolymers cannot be excluded.

12.5 ^{2}H Quadrupolar NMR

Anisotropy in co-SPI membranes was assessed by examining the quadrupole splittings ($\Delta\nu_Q$) observed in ^{2}H NMR spectroscopy on absorbed D_2O. For an isotropic system such as liquid water, a single peak is observed due to the fast molecular reorientation of D_2O molecules. Non-isotropic morphology on the nanometer scale, such as aligned hydrophilic channels or stacked lamellar layers, leads to anisotropic diffusion that results in a ^{2}H peak splitting. Thus, $\Delta\nu_Q$ is dependent on the anisotropy of the environment and the direction of the material alignment axis relative to the spectrometer field:[64, 66, 79]

$$\Delta\nu_Q = Q_P \rho S_{matrix}((3\cos^2\theta - 1)/2) = {}^1/_2\,\Delta\nu_0(3\cos^2\theta - 1 + \eta\sin^2\theta) \qquad (12.3)$$

where Q_P is the quadrupole coupling constant (≈ 260 kHz for rigid O-D bonds) and S_{matrix} the order parameter of the network matrix. The interaction of the host matrix and the water molecules depends on several complex factors, including channel size or nature of the network surface. These contributions are all summarized in the scaling factor ρ. The right-hand side of Equation (12.3) is used to fit experimental splittings as a function of angle θ, where θ defines the angle between the material alignment axis and the spectrometer magnetic field B_0. Here, $\Delta\nu_0$ is the maximum splitting observed for a given membrane and η is the biaxiality parameter that is equal to zero for uniaxially aligned structures. For all membranes investigated in this work, η is zero within experimental error. More specifically, the term material alignment axis refers to a symmetry axis, which as such does not clarify does not clarify which kind of morphology is present in the examined material (e.g. spheres, channel, lamellar layers). Judging from the TEM and AFM images in Figure 12.1, the co-SPIs investigated here mainly exhibit a channel like morphology rather than lamellar layers.

Figure 12.8 shows the ^{2}H solid state NMR spectrum of fully hydrated membrane **(5)** for three different membrane orientations with respect to the spectrometer magnetic field direction B_0. When the membrane through-plane axis was oriented perpendicular to B_0, the splitting was 252 Hz (θ = 90°). This is half the size of the splitting observed if the through-plane axis coincided with B_0 ($\Delta\nu = 505$ Hz, $\theta = 0°$). At $\theta = 54.7°$, the doublet collapsed into a single line.

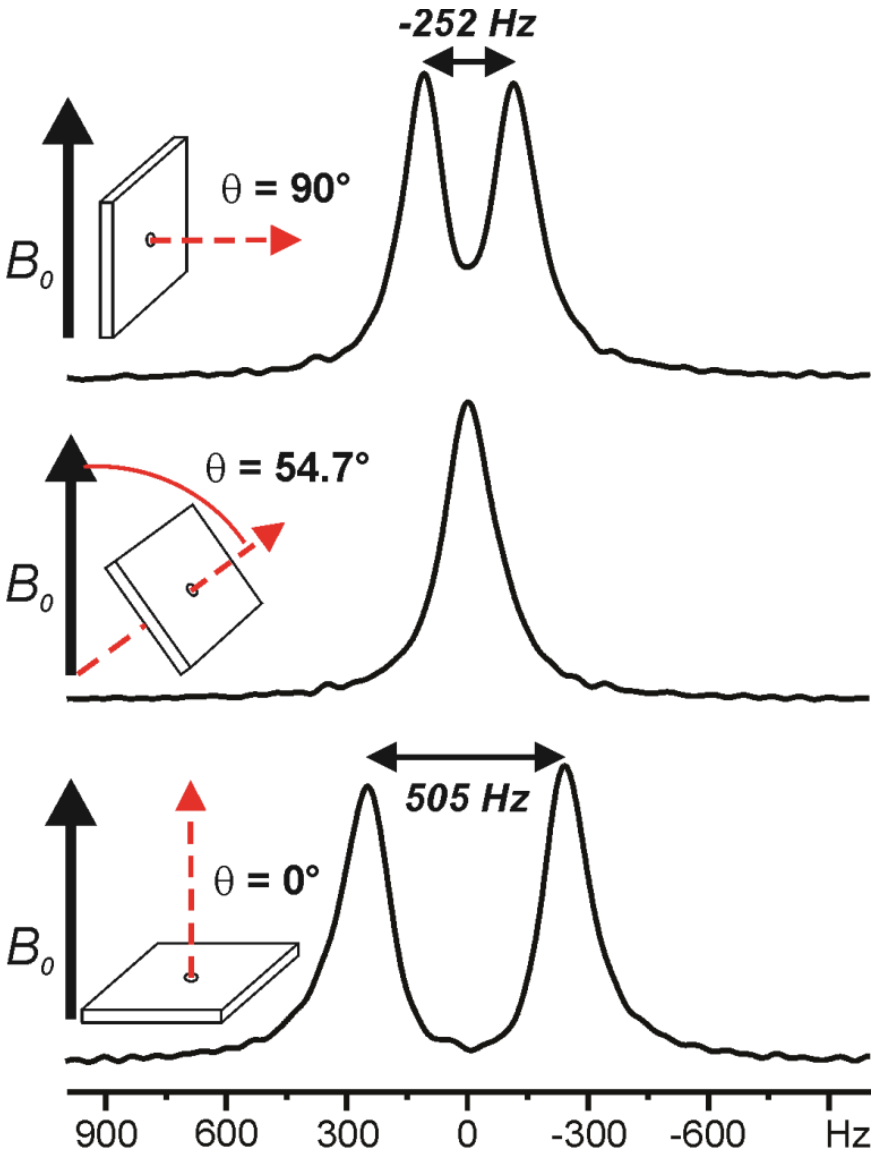

Figure 12.8: Room temperature ^{2}H NMR spectra of fully hydrated multiblock copolymer **(5)**. θ defines the angle between the material alignment axis (through-plane in this case) and the spectrometer magnetic field B_0. As predicted by Equation (12.3), the maximum splitting is equal two times the minimum splitting, which is observed when B_0 is parallel to the orientation of the membrane plane.

In Figure 12.9, Equation (12.3) is plotted for θ values ranging from 0° to 90°, with $\Delta\nu_0 = 505$ Hz and $\eta = 0$.

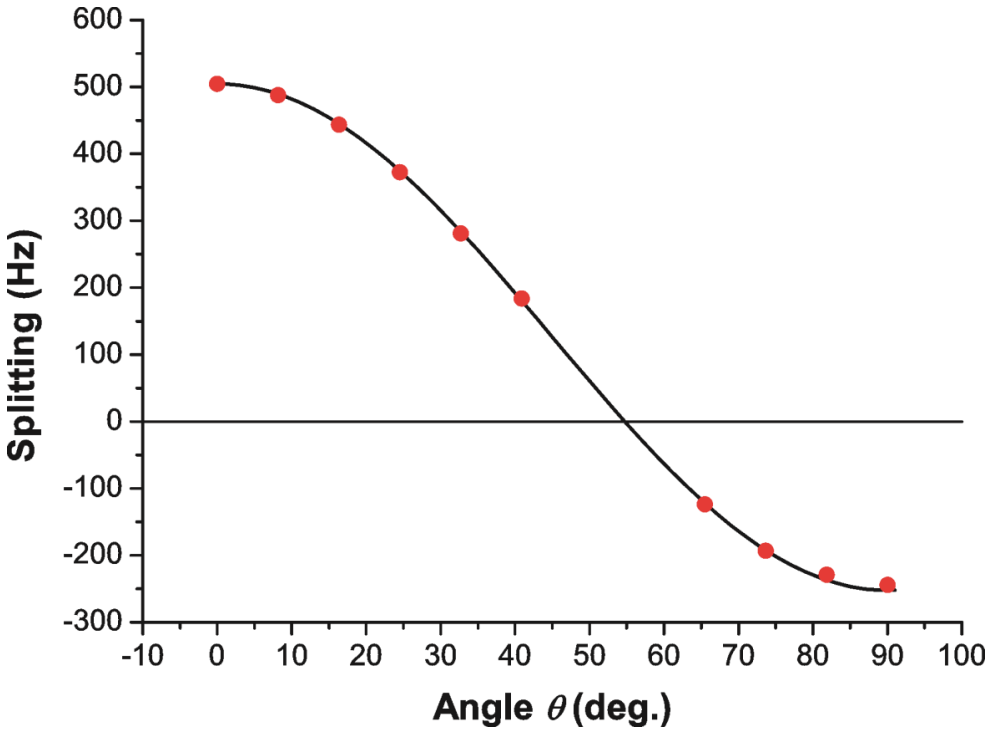

Figure 12.9: Plot of quadrupole splitting $\Delta\nu_Q$ vs. angle θ for **(5)** in the fully hydrated state. The solid line is a fitted curve using Eq. (12.3), where $\eta = 0$. $\Delta\nu_0$ is the maximum splitting that is found at $\theta = 90°$ (cf. Figure 12.8).

Experimental data (red data points) fit very well, indicating a preferential orientation (alignment) of hydrophilic channels macroscopically over the membrane. This is favorable, as the through-plane direction is the proton diffusion path in the actual fuel cell and thus proton conductivity should be maximized in this direction. It has been proposed, that this alignment arises from solvent evaporating in the direction normal to the membrane plane during the casting process and possibly additional processes during annealing.[80] It has to be emphasized, that this does not mean, that all channels are perfectly aligned in through-plane direction. Instead it can only be concluded that the *average* alignment direction of all channel domains within the D_2O diffusion length is through-plane. The length scale probed by the ^2H NMR measurement can be estimated with the help of a random walk expression:[64]

$$\sqrt{\langle r^2 \rangle} = \sqrt{\left(^{2D}/_{\Delta\nu_Q}\right)} \qquad (12.4)$$

where D is the diffusion coefficient (≈ $5 \cdot 10^{-11}$ m^2/s, see PFG section) and $\sqrt{\langle r^2 \rangle}$ the diffusion length, that is calculated to ≈ 0.5 µm for $\Delta\nu_Q$ = 500 Hz.

Control over the direction and extent of orientational order of the hydrophilic channels allows for increased proton conductivity. For example it has been demonstrated, that Nafion 112 and Nafion 117 (both extruded) show axially oriented channels in the extrusion direction, whereas the channels in Nafion NRE212 (dispersion-cast) are oriented perpendicular to the membrane plane.[64] However, also uniaxial elongation of already cast membranes may lead to significant orientation and strongly anisotropic morphology.[81]

Besides different values for $\Delta\nu_0$, all multiblock co-SPI membranes and **(r)** exhibit the same dependence of $\Delta\nu$ on θ as **(5)**, i.e. the material alignment axis is perpendicular to the membrane plane. This is most likely due to the identical solvent cast process for all samples.

Water uptake is a crucial parameter when determining the properties of a proton exchange membrane. For example, proton conductivity may vary over several orders of magnitude when altering the relative humidity (see Figure 12.6). Correspondingly, quantitative analysis of diffusion coefficients, as well as quadrupole splitting, is dubitable and non-reproducible, if no control over water content is achieved. Thus, sealed and low-dead-volume sample cells are indispensable.[64] To meet this requirement a customized and homemade Teflon sample cell was developed for performing PFG measurements as depicted in Figure 12.10.

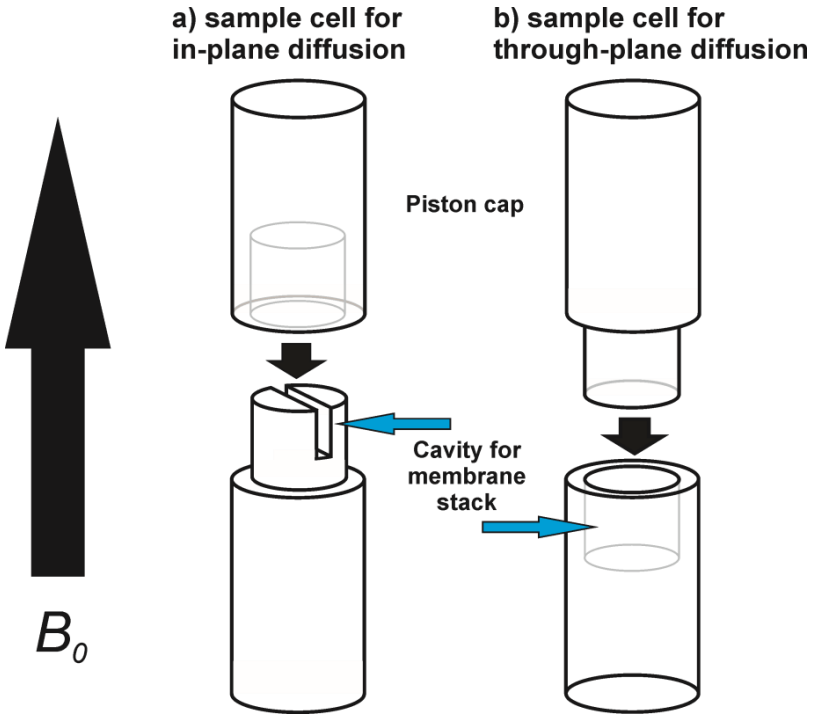

Figure 12.10: Schematic diagram of the sample cells for a) in-plane diffusion and b) through-plane diffusion PFG experiments. In both cases, at least 10 sheets of membrane were stacked to ensure a very low dead volume. Care was taken to fabricate tight-fitting caps to prevent loss of water during the experiments. For in-plane diffusion measurements, membranes were cut into rectangular pieces of 3 mm x 4 mm in size. For through-plane diffusion measurements, round shaped sheets were punched out of the membrane and stacked on top of each other in the cylindrical cavity.

The direct proportionality between the NMR signal intensity and the D_2O content of the membrane for sufficient long recycle delays was used to determine the level of hydration. As water uptake as well as the absolute intensity of ^2H NMR experiments on fully saturated membranes at room temperature is known (Table 12.2), the intensity of ^2H NMR experiments on partially hydrated membranes can be exploited to calculate the specific water uptakes. In general, the quadrupole splitting increases as the membrane D_2O content decreases (Figure 12.11), which can be attributed to an increased anisotropic interaction (e.g. caused by restricted rotations) with the channel walls.

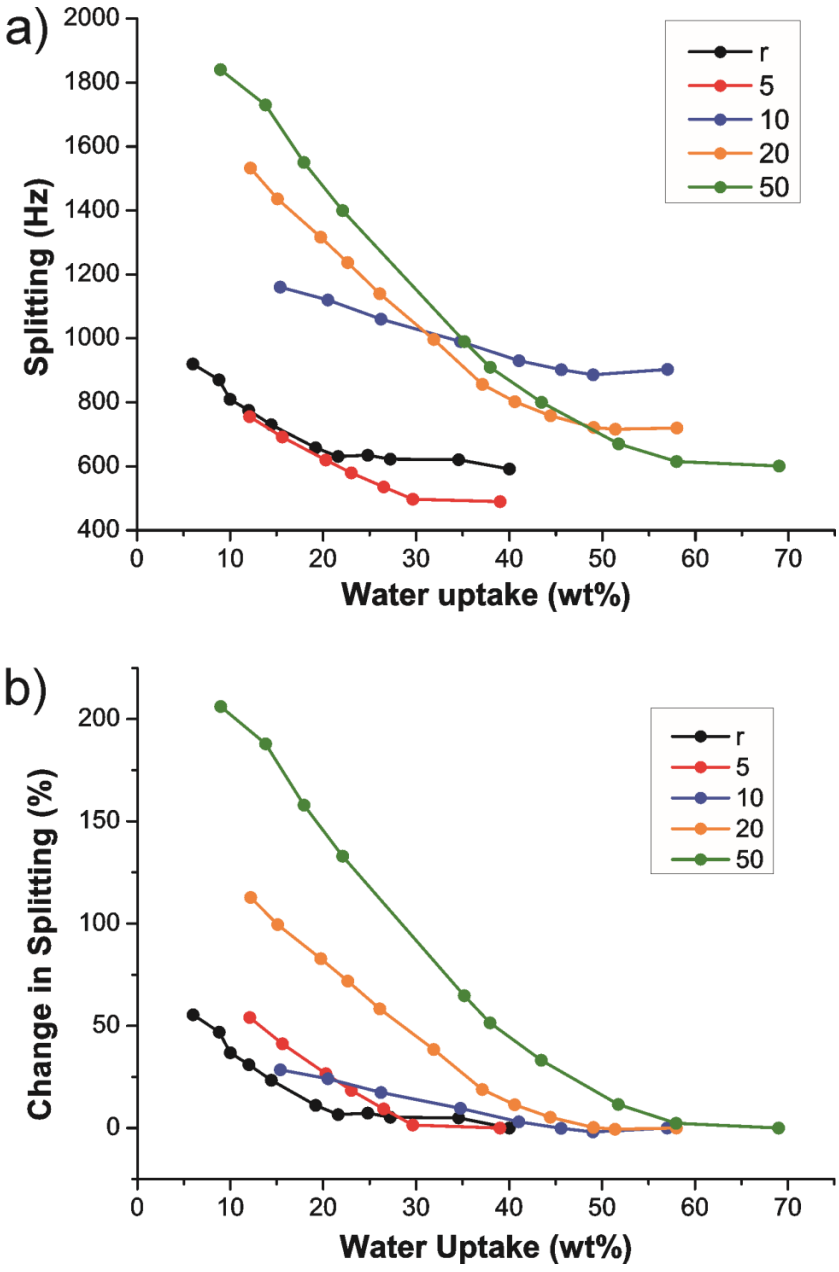

Figure 12.11: Room temperature ^2H splitting $\Delta\nu_Q$ vs. D_2O uptake.

This effect originates from shrinking of the average hydrophilic domain diameter upon loss of water and is consistent with the observation of water uptake dependent quadrupolar splittings for Nafion membranes[64, 81] and sulfonated poly(arylene ether sulfone) block copolymers.[66] Specifically, it is the scaling factor ρ that increases with decreasing hydrophilic channel diameter as the quadrupole coupling constant Q_{P} and the order parameter S_{matrix} should not vary with water content to a first approximation.

Similarly, the ^{2}H splitting decreases on the order of 0.5 to 1.0 Hz per Kelvin with increasing temperature (not shown). This is most likely due to thermal expansion of the hydrophilic channels and enhanced isotropic D_2O rotation induced by higher kinetic energy of the water molecules.[64] Figure 12.11b illustrates that the longer the block length, the higher the *relative* increase in deuteron splitting when the water uptake is lowered. This phenomenon has already been observed for sulfonated block copolymers and may be related to a faster, relative shrinking of hydrophilic channels for larger domains.[66] A simple, intuitive explanation for the difference in *absolute* splitting cannot be given at this point because i) no clear trend with respect to block length is observed and ii) the quadrupolar splitting for different batches of membranes with formally the same block length varied considerably for identical water uptake. For example, the maximum splittings of D_2O saturated membranes with formal block length of 10 are 470, 675 and 900 Hz for three different batches. Remembering that the length scale accessible of the NMR experiment is around 0.5 µm, this suggests that very small differences in the membrane casting procedure and/ or polymer characteristics (block length, IEC, poly dispersity etc.) may have a tremendous effect on the interactions on a *local* scale. In contrast, conductivity measurements (length scale several µm) show virtually identical values.

12.6 ^{1}H Pulsed Field Gradient NMR

By applying a magnetic field gradient with strength g for a period δ, diffusing molecules can be marked depending on their position in the sample. After a diffusion time Δ, the new position of the spatially labeled molecule is decoded with a second gradient of the same strength and duration. Stejskal and Tanner developed the first pulse sequence, the pulse gradient spin echo (PGSE),[56] to measure diffusion coefficients and in the case of rectangular gradients one finds

$$I = I_0 e^{-\gamma^2 g^2 \delta^2 \left(\Delta - \frac{\delta}{3}\right) D} = I_0 e^{-bD} \quad (12.5)$$

$$\ln\left(I/I_0\right) = -bD \quad (12.6)$$

Here, I is the spin-echo signal intensity, I_0 is the signal intensity at zero gradients, γ is the gyromagnetic ratio of the probe nucleus and D the self-diffusion coefficient of the observed molecule. For reasons of simplification, $(\gamma g \delta)^2(\Delta - \delta/3)$ is reduced to b. Practically, it is impossible to generate perfect rectangular gradient pulses, as extremely high voltage would be required, leading to irreproducible pulses. For this reason, sine shaped pulses were applied. Furthermore, instead of the PGSE experiment, the pulse gradient stimulated echo (PGSTE) sequence was used since it is mainly dependent on T_1 instead of T_2 $(T_1 > T_2)$.[82] Compared to the PGSE experiment, this sequence has less limits on the choice of the diffusion time Δ. The self-diffusion coefficients D were determined by plotting b vs. $\ln(I/I_0)$, while b was varied by incrementing the gradient strength g in linear steps. In case of a monomodal intensity decay, i.e. all water molecules exhibit the same diffusion coefficient, Equation (12.6) predicts a straight line with slope D.

Similar to ^{2}H quadrupolar NMR, control of the water content is a must for experiments on proton exchange membranes. As for the ^{1}H PFG NMR experiments, tight-fitting caps with low dead volume were used to minimize water evaporation once the cell is put out of the climatic chamber and into the NMR tube.

Figure 12.12a shows the plot of $\ln(I/I_0)$ vs. b for samples **(r)** and **(50)** together with the respective best linear fit. Clearly, the expected straight line is obtained for **(r)**, but not for **(50)**. If the same experimental data of **(50)** is plotted vs. gradient g (Figure 12.12b), it becomes apparent that experiment and monomodal fit deviate not only for large values of g, but also especially at the beginning of the experiment. However, fitting the data for **(50)** with a superposition of two exponentials (bimodal) yields satisfying result, which physically corresponds to two distinct diffusion processes whose NMR signals overlap.

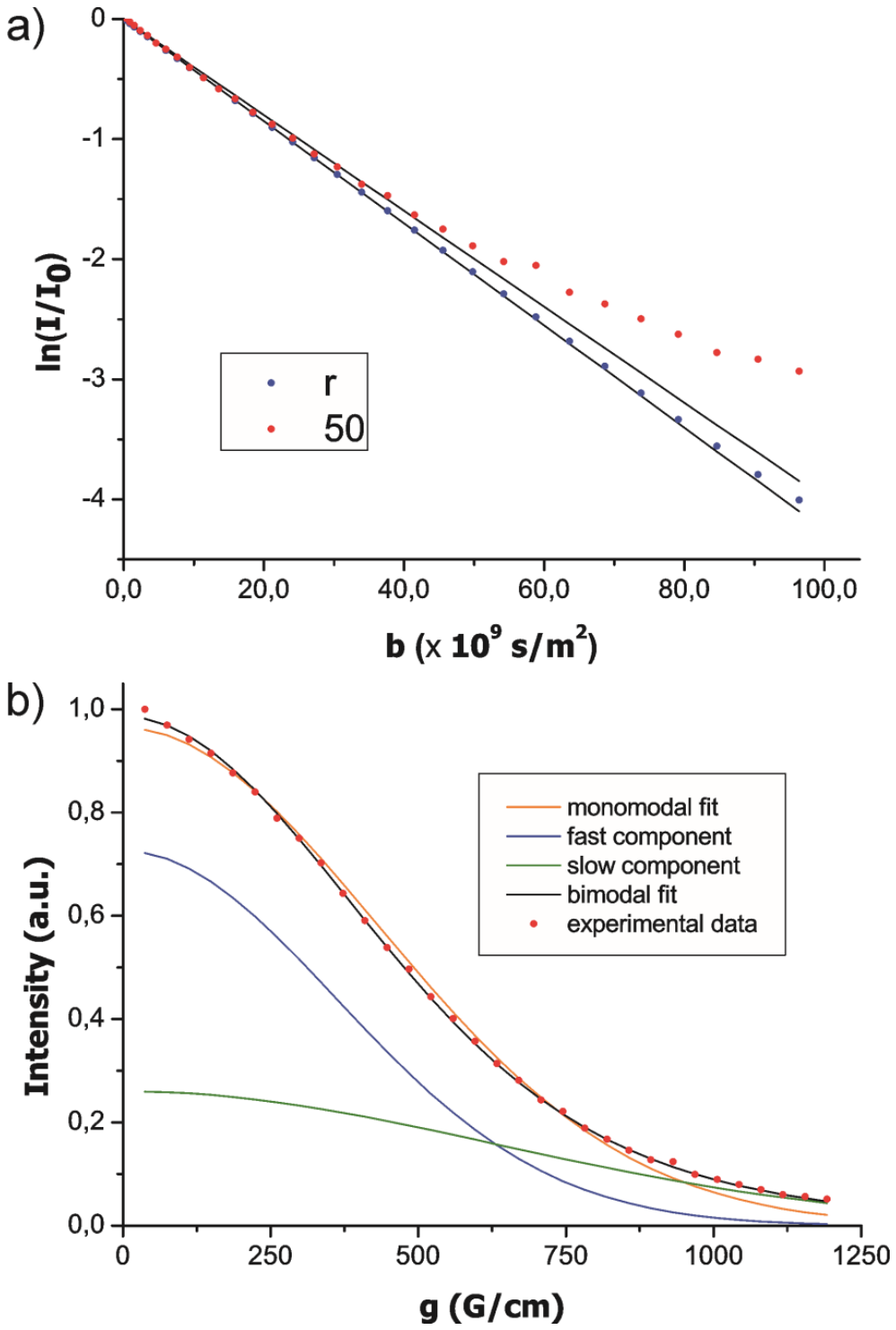

Figure 12.12: Identical experimental data for **(50)** at 60% relative humidity and 25°C, plotted in two different ways. Solid lines are best fits according to Equation (12.5) and (12.6) respectively. a) Normalized signal amplitudes $\ln(I/I_0)$ of stimulated echo decays as a function of parameter b. Data of **(r)** recorded under the same experimental conditions is included for comparison. Monomodal (i.e. monoexponential) fits were applied. In contrast to **(50)**, experimental data for **(r)** forms a straight line. b) Intensity vs. gradient g. Note the deviations of experiment and best monomodal fit, especially for small and large gradient values. A bimodal (i.e. biexponential) fit represents the experimental data very well. The observed intensity is decomposed into two components: a fast species with D_1 = 5,66·10^{-11} m^2/s and a slow one with D_2 = 1,85·10^{-11} m^2/s. Relative proportions are 73% and 27% respectively.

As the only diffusing species is H_2O, the difference in diffusion coefficients must be induced by two unalike environments within the membrane, where water diffuses fast in one domain (assigned to diffusion-coefficient D_1) and slow (corresponds to D_2) within the other, i.e. $D_1 > D_2$. It can be seen that the fast process accounts for the steep intensity decay for small values of g, whereas the slow diffusion process (D_2) explains the relatively slow decay of intensity for strong gradients. Most likely this difference in diffusion coefficients is directly related to the inhomogeneities on the micrometer scale found for membrane **(50)** in TEM images. Water in the sulfur-rich domains is expected to diffuse faster due to the more ionic character of the environment. In contrast, the less sulfur-rich environment offers water molecules a more hydrophobic diffusion pathway, hindering fast travelling that manifests itself in a lower diffusion coefficient. The length scale of the PFG NMR experiment is given by (cf. eq. (12.4)):

$$\sqrt{\langle r^2 \rangle} = \sqrt{(2D\Delta)} \qquad (12.7)$$

Here, Δ is the diffusion time and with D = $5 \cdot 10^{-11}$ m^2/s, we find $\sqrt{\langle r^2 \rangle}$ in the range of 1 µm, corresponding to the length scale of the superordinate morphology found for **(50)**. As **(50)** is the only membrane with observable micrometer scale phase separation, all other membranes exhibit ^1H PFG NMR curves that can be fitted with a single diffusion coefficient. Indeed, PFG NMR data of **(50)** are the only requiring a bimodal fit, irrespective of the relative humidity conditions.

Figure 12.13 lists the results of ^1H PFG NMR experiments for all membranes at 19%, 30%, 45% and 60% relative humidity. For all materials, water diffusion coefficients increased with increasing relative humidity. At 19% relative humidity, the diffusion coefficient was below 10^{-12} m^2/s and rose to approx. $5 \cdot 10^{-11}$ m^2/s at 60% relative humidity. This is due to an increasing water uptake that swells the hydrophilic channels in the membrane and facilitates proton transport. Diffusion coefficients of absorbed water in Nafion and sulfonated block poly(sulfones) were reported to be one order of magnitude higher,[64, 66] indicating that the local environment is more favorable in these materials compared to the block poly(imides) investigated here. The self-diffusion coefficient of pure water is $2{,}30 \cdot 10^{-9}$ m^2/s at 25°C,[83] i.e. even two orders of magnitude higher and demonstrates that diffusion of water in the hydrophilic channels is highly restricted by its surroundings.

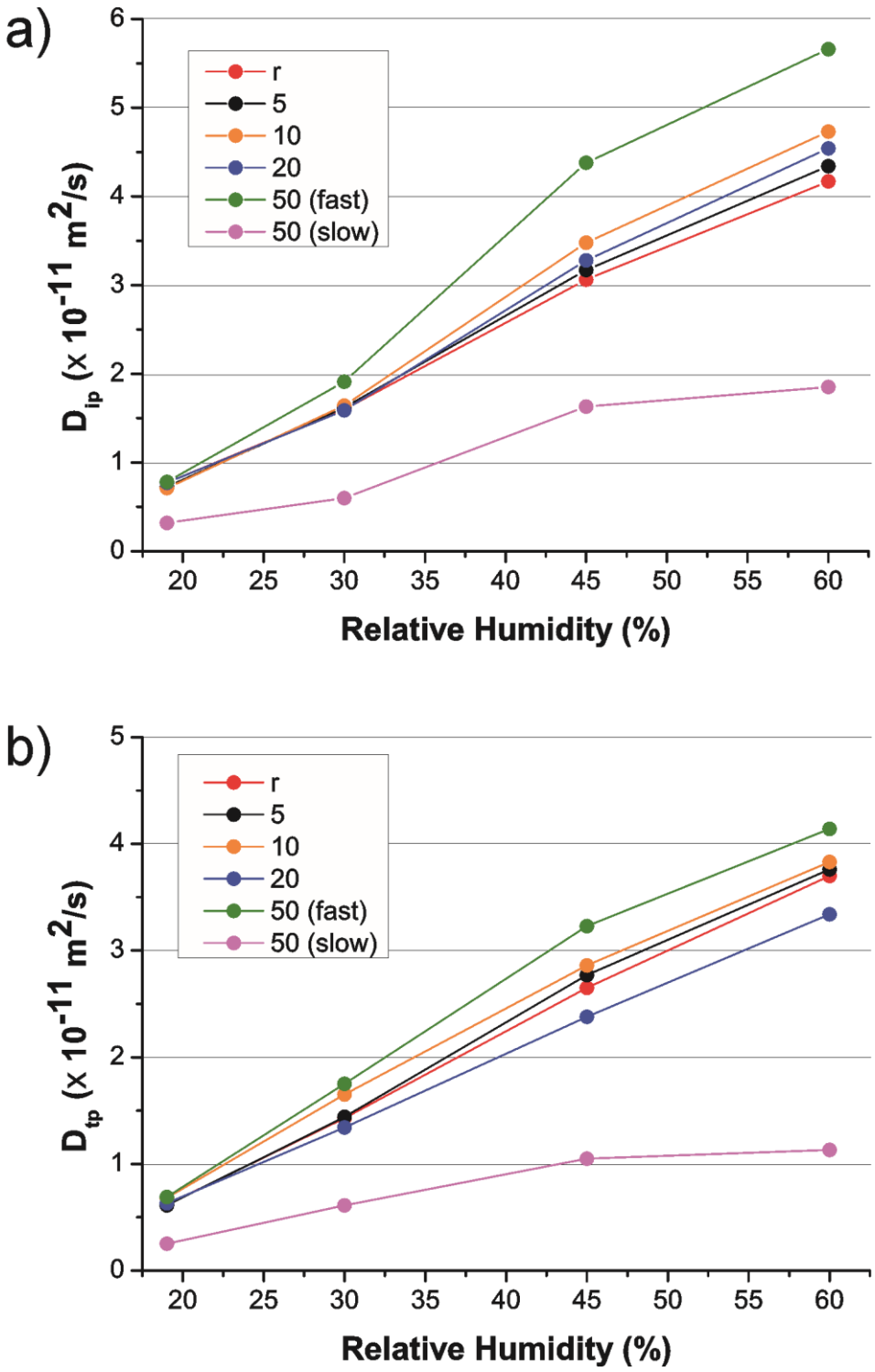

Figure 12.13: Plots of water diffusion coefficients a) in-plane and b) through-plane vs. water uptake, measured at 25°C. The annotations fast and slow for membrane **(50)** denote the deconvolution of the experimental data into two processes.

It has to be emphasized, that it is not possible to draw conclusions on conductivity based on the values of diffusion coefficients alone. Even though diffusion processes should be related to conductivity due to the required motion of water in both cases, the length scale of both experiments is different. Hence, a direct correlation is not possible. This is demonstrated in

Figure 12.13a and b, where diffusion coefficients increase with increasing block length in the order **(r)**, **(5)** and **(10)** before a drop for **(20)** is observed. However, conductivity is higher for **(20)** than for membranes with smaller block length. It can be speculated that, even though the local environment is unfavorable for proton diffusion in **(20)**, a very effective long-range percolation network is present in this membrane, overcompensating for the comparable slow small-range diffusion. This is supported by the data of Table 12.3. In analogy to ^{1}H PFG NMR, the analysis of temperature dependent ^{1}H line widths is also a local probe of proton mobility and relatively high activation energy E_A for the hopping of acidic protons is found for **(20)**, pointing towards an unfavorable local environment. As explained above, two diffusion processes could be identified for sample **(50)**: a fast (D_1) and a slow one (D_2). D_1 is higher than the diffusion coefficient of the other membranes, whereas D_2 is lower over the whole humidity range. This correlates well with the ^{1}H MAS NMR data (Figure 12.4) that suggests that hydrophilic domains in **(50)** have the highest ionic character owing to an effective phase separation. The calculated contribution of the fast component to the overall signal intensity is about 2/3 for all experiments.

Weak diffusion anisotropy, defined as the ratio of through-plane (D_{tp}) to in-plane diffusion coefficient(D_{ip}), is observed for all membranes. Assuming a channel-like morphology as derived from TEM and AFM images (Figure 12.1) and taking into account the results of ^{2}H quadrupolar NMR, hydrophilic channels are expected to be oriented perpendicular to the membrane plane. Consequently, diffusion is expected to be faster in this direction, rather than in-plane. However, the diffusion coefficients were found to be highest for in-plane diffusion (Figure 12.13a). One explanation is that membranes comprise a lamella-like structure. In this case, as the symmetry axis is oriented through-plane, the lamellar layer plane would be oriented in-plane. Water molecules would prefer to diffuse within the membrane plane and only be able to transport perpendicular to the lamellae by the presence of morphological defects. Even though this might explain the PFG NMR results, there is no evidence of lamellar morphology in the TEM and AFM experiments. Thus, this issue requires further investigation, which is beyond the scope of this thesis.

13 Summary

A series of sulfonated block copolyimides was synthesized, using a two-pot procedure. Observed feature differences between the membranes can solely be ascribed to differences in block length as the IEC was held constant and only the block length was varied from 5 to 50 repeat units. Proton conductivity increases with increasing block length. Especially at low relative humidity conditions, the performance of random copolyimide is inferior to its block counterparts. Water uptake measurements reveal that to some extent this is caused by the good water retaining properties of block copolymers. Morphology was assessed by TEM and AFM measurements. Both techniques revealed growing domain size with increasing block length that point towards a channel-like morphology. For membrane **(50)**, the hydrophilic character of the phase-separated, ionic channels was examined by solid-state NMR. These experiments demonstrated that the quality of the phase-separation rises with growing domain size. Although sample **(20)** is a better proton conductor than **(5)** and **(10)**, the *local* proton environment does not support fast proton mobility. However, proton conductivity is a macroscopic feature that also depends on a developed percolation network and additional large-scale influences.

From a combination of ^{1}H PFG NMR and ^{2}H quadrupolar NMR, insights into domain alignment and anisotropic structures were achieved. The symmetry axis of diffusion is found to be perpendicular to the membrane plane for all membranes investigated. The finding that diffusion is faster in in-plane than in through-plane direction does not support the existence of hydrophilic channels aligned in through-plane direction. However, TEM and AFM give no indication for a layer-like morphology that would explain the ^{1}H PFG NMR results. Application of these methods to other membrane materials is desirable to develop general concepts and to gain control of material alignment in next generation membranes.

14 Experimental Section

14.1.1 Materials

1,4,5,8-Naphthalene tetracarboxylic dianhydride (NTDA), 4,4'-diaminodiphenyl ether (ODA), *m*-cresol and triethylamine (TEA) were purchased from Sigma-Aldrich and used as received. 2,2-bis(4-aminophenyl)hexafluoropropane and benzoic acid were obtained from Acros. 4,4'-Oxydianiline-2,2'-disulfonic acid (ODADS) was prepared according to the method previously reported.[46] Monomers were stored under vacuum to avoid moisture contamination.

14.1.2 Synthesis of random sulfonated copolyimide

To a 100 ml completely dried flask equipped with a condenser were successively added ODADS (540.5 mg, 1.5 mmol), *m*-cresol (15 ml) and TEA (0.5 ml, 3.6 mmol) under argon flow with stirring. After ODADS was completely dissolved, NTDA (804.5 mg, 3.0 mmol), BAHF (501.4 mg, 1.5 mmol) and benzoic acid (512.9 mg, 4.2 mmol) were added. The mixture was stirred at room temperature for a few minutes and then heated at 80°C for 4 h and 180°C for 20 h. After cooling to 100°C, additional 15ml *m*-cresol were added to dilute the highly viscous solution, which was then poured into 300 ml of acetone. The precipitate was filtered off, washed with acetone, and dried in vacuo for 24 h at 80°C.

14.1.3 Synthesis of multiblock sulfonated copolyimide

Multiblock co-SPIs were synthesized by a two-pot method as described in Scheme 9.1. As an example, the synthesis of NTDA-ODADS/BHF (20/20), where the Figures in parentheses refer to the hydrophilic/hydrophobic block lengths, is described below.

An anhydride-end-capped hydrophilic oligomer was synthesized as follows. A completely dried 100 ml flask equipped with a condenser was charged with ODADS (540.5 mg, 1.5 mmol), *m*-cresol (6 ml) and TEA (0.5 ml, 3.6 mmol) under argon flow with stirring. After ODADS was completely dissolved, NTDA (418.2 mg, 1.5592 mmol) and benzoic acid (268.7 mg, 2.2 mmol) were added to the flask. The reaction solution was heated to 80°C, left to stir for 4 h and then kept at 180°C for 20 h.

An amine-end-capped hydrophobic oligomer was synthesized as follows. A completely dried 100 ml flask equipped with a condenser was charged with BAHF (496.3 mg, 1.4847 mmol) and *m*-cresol (8 ml) under argon flow with stirring. After BAHF had dissolved, NTDA (382.2 mg, 1.4253 mmol) and benzoic acid (268.7 mg, 2.2 mmol) were added to the flask. The reaction solution was stirred at 120°C for 24 h.

The hydrophobic block oligomer solution was carefully added to the flask with the hydrophilic oligomer solution. The mixture was left to stir for 2 h at 120°C, followed by 22 h at 180°C. After cooling to 120°C, additional *m*-cresol (15 ml) was added to dilute the viscous solution. The dark mixture was poured into 300 ml acetone and the precipitate was filtered, washed with acetone and dried in vacuo for 24 h at 80°C.

14.1.4 Preparation of sulfonated copolyimide membranes

The sulfonated copolyimide membranes were prepared using a solvent-cast method. Co-SPIs in TEA salt form with block lengths up to 20 were dissolved in DMSO (ca. 5 wt%) in the heat, the solution filtered and cast onto glass plates. Due to solubility problems, co-SPI NTDA-ODADS/BHF (50/50) was dissolved in *m*-cresol (ca. 5 wt%). The glass plates were put in the oven in the oven at 120°C and ambient pressure, followed by 24 h at 120°C in vacuo to remove residual solvent. Obtained membranes of random co-SPI and multiblock co-SPIs with block lengths up to 20 were transparent. However, the co-SPI NTDA-ODADS/BHF (50/50) membrane was opaque although it formed a transparent solution in *m*-cresol before film casting. The as-cast membranes were soaked in methanol at 50°C for 1 h and then proton exchange was conducted by immersing the films in 1.0 M hydrochloric acid at room temperature overnight. The membranes in proton-form were thoroughly washed with deionized water and dried in vacuo at 120°C for 24 h. The thickness of the co-SPI films was in the range of 30 µm.

14.1.5 Membrane characterization

^{1}H solution state NMR spectra were measured at 250 MHz on an AVIII spectrometer. Thermogravimetric analyses (TGA) were conducted with a Mettler Toledo SDTA851 machine at a heating rate of 10°C/min in air (30°C to 900°C). Differential scanning calorimetry (DSC) was performed in air from 30°C to 200°C at a heating rate of 10°C/min, using a Mettler Toledo 822/400. Molecular weight of protonated polymers and oligomers was measured with gel permeation chromatography (GPC). Before the addition of the hydrophobic oligomer reaction mixture to the flask containing the sulfonated oligomer, a sample of about 0.1 ml of each oligomer reaction mixture was taken and precipitated in acetone (hydrophilic block) and methanol (hydrophobic block) respectively. Prior to the GPC measurement, the hydrophilic oligomers were transferred to the protonated state as described above. It turned out that the hydrophobic oligomers as well as the multiblock copolyimide with the longest blocks (50 repeat units) were not soluble in DMF, resulting in turbid solutions. Thus,

molecular weights are only given for hydrophilic oligomers and multiblock copolyimides with block lengths shorter than 50. A Waters machine equipped with three PSS GRAM columns and a Soma S-3702 UV detector (270 nm) were used with DMF containing 0.01 M LiBr as eluent (flow rate: 1.0 ml/min, temperature: 60°C). Polymer solutions were filtered through a 0.45 µm PTFE filter prior to injection. Molecular weights were calculated against poly(styrene) standards.

Proton conductivity of the membranes was measured by dielectric spectroscopy in a two-electrode in-plane geometry over a frequency range from 0.1 to 10^6 Hz, using a SI 1260 impedance/gain-phase analyzer and a Novocontrol broadband dielectric converter. The samples with a typical size of 10 x 10 mm were contacted by E-TEK™ electrodes and placed in a climatic chamber (Binder KBF 240). The membranes were exposed to the specified relative humidity and temperature until impedance data showed that moisture content had equilibrated. Due to the small membrane thickness of 20-40 µm, this state was obtained within several hours. The specific conductivity was calculated from Bode plots. At least two samples of each membrane were measured and values averaged.

Light scattering experiments were performed at room temperature using an ALV unit equipped with an ALV/CGS3 compact goniometer (ALV-Laser Vertriebsgessellschaft mbH, Langen, Germany), ALV/LSE-5004 correlator and a He/Ne laser (λ =632.7 nm). Signals from the detector were processed by ALV5000 software. The samples were dissolved in H_2O, DMF (1 g/L LiBr) and DMSO to give a concentration of 1 g/L and filtered with 0.45 µm PTFE filters prior to measurements.

For TEM examination the samples were sectioned at room temperature to a nominal thickness of 80 nm by microtome cutting with a diamond knife and transferred to a 400 mesh copper TEM grid. Microstructural characterization of these thin sections was done using a FEI Tecnai F20 transmission electron microscope equipped with a Gatan Tridiem 863 post column energy filter. All micrographs were taken at an acceleration voltage of 200 kV. The elemental distribution of sulfur was acquired by applying the three window method under the assumption of a power law background in the electron energy loss spectrum.[84] Membranes were stained with silver by immersion of samples in a 0.5 M $AgNO_3$ aqueous solution for 24 hours, rinsed with distilled water and finally dried at room temperature. TEM measurements were conducted by Ingo Lieberwirth.

The AFM topography mapping was performed in intermittent contact mode under ambient conditions. Measurements were done with a Bruker D3100. Tapping mode cantilevers were applied (nominal resonance frequency 70 kHz and 2 N/m spring constant, OMLAC 240 TS, Al back side coated). Tips were changed at regular intervals to avoid artifacts resulting from tip changes during scanning. For domain size analysis, all points in an image above 65% of height were selected. The average domain size was calculated using GWYIDDION software. AFM measurements were conducted by Esha Sengupta.

Ion exchange capacities (IECs) were determined by titration and compared with the theoretical values calculated from the monomer feed ratios. The membranes in proton-form were immersed in a 1 M NaCl solution for 24 h to liberate the protons. Then the solution with released H^+ ions was titrated with aqueous 0.01 M NaOH solution using phenolphthalein as indicator. Additionally, membranes in proton-form were dissolved in DMSO-d_6 for ^{1}H NMR measurements. No residual TEA resonances were visible, pointing towards quantitative proton exchange. Ion exchange capacity is given in milliequivalents per gram, i.e. the amount of NaOH necessary to neutralize the sulfonic acid groups in one gram of dry polymer. The prefix *milli* denotes that the measure is divided by 1000.

Water uptake experiments at room temperature were carried out by drying ca. 30 mg per membrane sheet in vacuo at 100°C overnight, followed by an immersion of the sheets in deionized water for two days. Then the films were taken out, wiped with tissue paper, and quickly weighed on a microbalance. Water uptake at defined relative humidity (RH) and elevated temperature was measured by equilibrating membrane sheets in a climatic chamber for at least 3 h at 50°C. Water uptake (WU) of the films was calculated from:

$$\mathrm{WU(wt\%)} = (W_{wet} - W_{dry})/W_{dry} \tag{14.1}$$

where W_{wet} and W_{dry} are the weights of dry and water-swollen membrane respectively.

Dimensional change of the SPI membranes was measured by drying a round shaped sample (2 cm diameter) in vacuo at 100°C overnight, followed by an immersion of the sheets in deionized water for two days. Through-plane and in-plane dimensional changes as well as the anisotropic membrane swelling ratio were calculated from:

$$\Delta t = (t - t_0)/t_0 \tag{14.2}$$

$$\Delta l = (l - l_0)/l_0 \tag{14.3}$$

$$\Delta_{t/l} = \Delta t/\Delta l \tag{14.4}$$

Where t_0 and l_0 are the thickness and length of the dry membrane respectively; t and l refer to the values measured after immersion in water.

Solid-state ^{1}H magic-angle spinning (MAS) NMR spectra of dried membranes were acquired using single-pulse excitation on a Bruker AVANCE 700 spectrometer. Experiments were carried out in a Bruker 2.5 mm double resonance (MAS) probe spinning at 25.0 kHz, a $\pi/2$-pulse length of 2.5 µs, and a recycle delay of 1 s (well above T_1). The spectra were recorded using 32 transients. The spectra are referenced to TTSS (0.27 ppm, ^{1}H) and the sample temperature was corrected to include heating effects arising from high-speed MAS.[85]

^{13}C MAS NMR spectra were acquired at 125.77 MHz using a Bruker DSX 500 machine with a contact time of 1 ms, coadding 32k transients. The experiments were carried out using a Bruker 2.5 mm double resonance MAS probe spinning at 25 kHz, a π/2-pulse length of 2.5 µs, and a recycle delay of 2 s.

14.1.6 ^{1}H PFG NMR

Self-diffusion coefficients of water in membranes were measured in-plane (D_{ip}) and through-plane (D_{tp}) using the 700 MHz Bruker AVIII narrow-bore NMR equipped with a single axis diffusion probe having a maximum gradient of 1192 G/cm in B_0 direction. PGSTE experiments with $\delta = 1\ \mathrm{ms}\ (\leq T_2)$ and $\Delta = 10\ \mathrm{ms}$ were performed at 25°C for membranes equilibrated in 60%, 45% and 30% relative humidity, whereas Δ was set to 20 ms for samples with the lowest water content (19% relative humidity). D proved to not vary with Δ in the range of 10 to 50 ms. T_1 was about 10 ms, so a recycle time of 0.43 s was sufficient for all measurements. 16 scans were coadded for each gradient step. Temperature was calibrated using a solution of 4% CH_3OH in CD_3OD as standard. The gradient constant was calibrated by measuring the diffusion coefficient of 1% H_2O in a solution of 0.1 mg/ml $GdCl_3$ in D_2O ("doped water") to a literature value of $1.91 \cdot 10^{-9}$ m^2/s at 25°C.[86, 87] 32 gradient steps were applied. For in-plane diffusion, the sample stacks were loaded into a handmade Teflon sample cell (depicted in Figure 12.10), which can fit vertically into a regular 5 mm NMR tube. For through-plane, another Teflon cell comprised of a cylindrical cavity was used. In the first case, the spectrometer magnetic field B_0 direction is parallel to the membrane surface, whereas in the second case it is normal to the membrane surface. Care was taken to place the samples in the center of the RF coil. Membrane water uptake was adjusted by putting the open (without piston cap), loaded sample cell into a climatic chamber with defined RH at

25°C overnight. Fitting of the data and calculation of diffusion coefficients was executed with Bruker TopSpin 2.1 software.

14.1.7 ^{2}H NMR

^{2}H solid-state NMR spectroscopy was performed at 25°C on a Bruker AVIII 7.0 T wide-bore spectrometer corresponding to a ^{2}H Larmor frequency of 46.09 MHz. A single channel detection static solids probe with 8 mm inside diameter horizontal solenoid coil was used. The sample cell could be rotated in the NMR coil casing, using a goniometer to accurately adjust orientation of the sample cell to ±2° accuracy. The shape of the sample cell was identical to the cell used for ^{1}H PFG NMR experiments for in-plane diffusion measurements (Figure 12.10). However, due to the larger inside diameter of the solenoid coil, the slit for the membrane stack had a size of 6 mm x 6 mm. Experiments were carried out using a single $\pi/2$ pulse of 15 μs, repetition time of 0.5 s (well above T_1), and typically 256 scans per spectrum. Quadrupole splittings were extracted by fitting each spectrum using the program DMFit.[88] Membranes were soaked in D_2O for at least 24 h, cut into 10 pieces of 6 mm x 6 mm in size, stacked together and trimmed to match the rectangular shaped cavity in the cell. The wt% of unsaturated membranes was measured using relative NMR signal intensities. D_2O was allowed to slowly evaporate from the membranes by partially removing the sample cell cap in nitrogen atmosphere.

15 Literature

[1] K. Kacholia, R. A. Reck, *Clim. Change* **1997**, *35*, 53.

[2] R. W. Dorner, D. R. Hardy, F. W. Williams, B. H. Davis, H. D. Willauer, *Energy Fuels* **2009**, *23*, 4190.

[3] M. Ree, J. Y. Bae, J. H. Jung, T. J. Shin, *J. Polym. Sci., Part A: Polym. Chem.* **1999**, *37*, 1863.

[4] W. Ross Morrow, K. S. Gallagher, G. Collantes, H. Lee, *Energy Policy*, *38*, 1305.

[5] J. Larminie, A. Dicks, *Fuel Cell Systems Explained, 2nd Edition*, Wiley, **2003**.

[6] J. R. Rostrup-Nielsen, *Catal. Today* **1994**, *18*, 305.

[7] A. J. Appleby, *Fuel Cell Systems*, Plenum Publishing, New York, **1994**.

[8] W. Grot, *Chem.-Ing.-Tech.* **1972**, *44*, 167.

[9] W. Grot, *Chem.-Ing.-Tech.* **1975**, *47*, 617.

[10] M. Doyle, G. Rajendran, *Handbook of Fuel Cells, Vol. 3*, Wiley, Weinheim, **2003**.

[11] L. Gubler, G. G. Scherer, *Adv. Polym. Sci.* **2008**, *215*, 1.

[12] N. Agmon, *Chem. Phys. Lett.* **1995**, *244*, 456.

[13] D. Marx, M. E. Tuckerman, J. Hutter, M. Parrinello, *Nature (London)* **1999**, *397*, 601.

[14] H. Zhang, P. K. Shen, *Chem. Rev.* , Ahead of Print.

[15] N. Sammes, R. Bove, K. Stahl, *Curr. Opin. Solid State Mater. Sci.* **2005**, *8*, 372.

[16] K. D. Kreuer, *J. Membr. Sci.* **2001**, *185*, 29.

[17] E. P. Jutemar, P. Jannasch, *J. Membr. Sci.* **2010**, *351*, 87.

[18] Y. A. Elabd, E. Napadensky, C. W. Walker, K. I. Winey, *Macromolecules* **2006**, *39*, 399.

[19] C. Zhao, X. Li, Z. Wang, Z. Dou, S. Zhong, H. Na, *J. Membr. Sci.* **2006**, *280*, 643.

[20] K. Schmidt-Rohr, Q. Chen, *Nat. Mater.* **2008**, *7*, 75.

[21] B. Bae, K. Miyatake, M. Watanabe, *Macromolecules* **2009**, *42*, 1873.

[22] L. Chen, D. T. Hallinan, Y. A. Elabd, M. A. Hillmyer, *Macromolecules (Washington, DC, U. S.)* **2009**, *42*, 6075.

[23] T. Soboleva, Z. Xie, Z. Shi, E. Tsang, T. Navessin, S. Holdcroft, *J. Electroanal. Chem.* **2008**, *622*, 145.

[24] N. Asano, K. Miyatake, M. Watanabe, *J. Polym. Sci., Part A: Polym. Chem.* **2006**, *44*, 2744.

[25] A. S. Badami, O. Lane, H.-S. Lee, A. Roy, J. E. McGrath, *J. Membr. Sci.* **2009**, *333*, 1.

[26] K. Matsumoto, T. Higashihara, M. Ueda, *Macromolecules* **2009**, *42*, 1161.

[27] T. Nakano, S. Nagaoka, H. Kawakami, *Polym. Adv. Technol.* **2005**, *16*, 753.

[28] A. Roy, M. A. Hickner, X. Yu, Y. Li, T. E. Glass, J. E. McGrath, *J. Polym. Sci., Part B: Polym. Phys.* **2006**, *44*, 2226.

[29] T. D. Gierke, G. E. Munn, F. C. Wilson, *J. Polym. Sci., Polym. Phys. Ed.* **1981**, *19*, 1687.

[30] M. Eikerling, A. A. Kornyshev, E. Spohr, *Adv. Polym. Sci.* **2008**, *215*, 15.

[31] K. A. Mauritz, R. B. Moore, *Chem. Rev.* **2004**, *104*, 4535.

[32] T. J. Peckham, S. Holdcroft, *Adv. Mater.* **2010**, *22*, 4667.

[33] C. Marestin, G. Gebel, O. Diat, R. Mercier, *Adv. Polym. Sci.* **2008**, *216*, 185.

[34] Y. Yang, A. Siu, T. J. Peckham, S. Holdcroft, *Adv. Polym. Sci.* **2008**, *215*, 55.

[35] K. Yamazaki, Y. Tang, H. Kawakami, *J. Membr. Sci.* **2010**, *362*, 234.

[36] S. Faure, N. Cornet, G. Gebel, R. Mercier, M. Pineri, B. Sillion, *New Mater. Fuel Cell Mod. Battery Syst. II, Proc. Int. Symp., 2nd* **1997**, 818.

[37] F. Zhang, N. Li, Z. Cui, S. Zhang, S. Li, *J. Membr. Sci.* **2008**, *314*, 24.

[38] N. Li, Z. Cui, S. Zhang, W. Xing, *Polymer* **2007**, *48*, 7255.

[39] N. Li, J. Liu, Z. Cui, S. Zhang, W. Xing, *Polymer* **2009**, *50*, 4505.

[40] N. Li, Z. Cui, S. Zhang, S. Li, *J. Polym. Sci., Part A: Polym. Chem.* **2008**, *46*, 2820.

[41] Y. Yin, O. Yamada, K. Tanaka, K.-I. Okamoto, *Polym. J.* **2006**, *38*, 197.

[42] G. Meyer, G. Gebel, L. Gonon, P. Capron, D. Marscaq, C. Marestin, R. Mercier, *J. Power Sources* **2006**, *157*, 293.

[43] N. Endo, K. Matsuda, K. Yaguchi, Z. Hu, K. Chen, M. Higa, K. Okamoto, *J. Electrochem. Soc.* **2009**, *156*, B628.

[44] Y. Sutou, Y. Yin, Z. Hu, S. Chen, H. Kita, K.-I. Okamoto, H. Wang, H. Kawasato, *J. Polym. Sci., Part A: Polym. Chem.* **2009**, *47*, 1463.

[45] X. Guo, J. Fang, K. Tanaka, H. Kita, K.-I. Okamoto, *J. Polym. Sci., Part A: Polym. Chem.* **2004**, *42*, 1432.

[46] J. Fang, X. Guo, S. Harada, T. Watari, K. Tanaka, H. Kita, K. Okamoto, *Macromolecules* **2002**, *35*, 9022.

[47] K. Yaguchi, K. Chen, N. Endo, M. Higa, K.-i. Okamoto, *J. Power Sources* **2010**, *195*, 4676.

[48] X. Guo, J. Fang, T. Watari, K. Tanaka, H. Kita, K. Okamoto, *Macromolecules* **2002**, *35*, 6707.

[49] K. Chen, Z. Hu, N. Endo, M. Higa, K.-i. Okamoto, *Polymer* **2011**, *52*, 2255.

[50] Z. Hu, Y. Yin, K. Yaguchi, N. Endo, M. Higa, K.-i. Okamoto, *Polymer* **2009**, *50*, 2933.

[51] J. Yan, C. Liu, Z. Wang, W. Xing, M. Ding, *Polymer* **2007**, *48*, 6210.

[52] M. J. Park, N. P. Balsara, *Macromolecules* **2010**, *43*, 292.

[53] O. Yamada, Y. Yin, K. Tanaka, H. Kita, K.-I. Okamoto, *Electrochim. Acta* **2005**, *50*, 2655.

[54] Y. Cohen, L. Avram, L. Frish, *Angew. Chem., Int. Ed.* **2005**, *44*, 520.

[55] W. S. Price, *Mod. Magn. Reson.* **2006**, *1*, 105.

[56] E. O. Stejskal, J. E. Tanner, *J. Chem. Phys.* **1965**, *42*, 288.

[57] T. Ohkubo, K. Kidena, A. Ohira, *Macromolecules* **2008**, *41*, 8688.

[58] K. Kidena, *J. Membr. Sci.* **2008**, *323*, 201.

[59] R. L. Smith, E. Oldfield, *Science* **1984**, *225*, 280.

[60] H. Toriumi, B. Deloche, J. Herz, E. T. Samulski, *Macromolecules* **1985**, *18*, 304.

[61] B. Deloche, E. T. Samulski, *Macromolecules* **1981**, *14*, 575.

[62] K. Matsumura, K. Hayamizu, T. Nakane, H. Yanagishita, O. Yamamoto, *J. Polym. Sci., Part B: Polym. Phys.* **1988**, *26*, 2215.

[63] C. Migchelsen, H. J. C. Berendsen, *J. Chem. Phys.* **1973**, *59*, 296.

[64] J. Li, K. G. Wilmsmeyer, L. A. Madsen, *Macromolecules* **2009**, *42*, 255.

[65] J. Li, J. K. Park, R. B. Moore, L. A. Madsen, *Nat. Mater.* **2011**, *10*, 507.

[66] J. Hou, J. Li, L. A. Madsen, *Macromolecules* **2010**, *43*, 347.

[67] K. Schmidt-Rohr, H. W. Spiess, *Multidimensional Solid-State NMR and Polymers*, Academic Press Inc., London, **1994**.

[68] M. Rankothge, Haryadi, G. Moran, J. Hook, L. Van Gorkom, *Solid State Ionics* **1994**, *67*, 241.

[69] G. Xu, Y. S. Pak, *Solid State Ionics* **1992**, *50*, 339.

[70] R. S. Chen, J. P. Jayakody, S. G. Greenbaum, Y. S. Pak, G. Xu, M. G. McLin, J. J. Fontanella, *J. Electrochem. Soc.* **1993**, *140*, 889.

[71] K. Lienkamp, C. F. Kins, S. F. Alfred, A. E. Madkour, G. N. Tew, *J. Polym. Sci., Part A: Polym. Chem.* **2009**, *47*, 1266.

[72] P. Choi, N. H. Jalani, R. Datta, *J. Electrochem. Soc.* **2005**, *152*, E123.

[73] G. Maier, J. Meier-Haack, *Adv. Polym. Sci.* **2008**, *216*, 1.

[74] M. R. Chierotti, R. Gobetto, *Chem. Commun.* **2008**, 1621.

[75] G. Ye, N. Janzen, G. R. Goward, *Macromolecules* **2006**, *39*, 3283.

[76] B. R. Cherry, C. H. Fujimoto, C. J. Cornelius, T. M. Alam, *Macromolecules* **2005**, *38*, 1201.

[77] G. R. Goward, M. F. H. Schuster, D. Sebastiani, I. Schnell, H. W. Spiess, *J. Phys. Chem. B* **2002**, *106*, 9322.

[78] C. P. Slichter, *Principles of Magnetic Resonance*, 3rd ed., Springer-Verlag, Berlin, **1990**.

[79] P. T. Callaghan, E. T. Samulski, *Macromolecules* **2003**, *36*, 724.

[80] J. Li, K. G. Wilmsmeyer, L. A. Madsen, *Macromolecules* **2008**, *41*, 4555.

[81] J. K. Park, J. Li, G. M. Divoux, L. A. Madsen, R. B. Moore, *Macromolecules* **2011**, *44*, 5701.

[82] J. E. Tanner, *J. Chem. Phys.* **1970**, *52*, 2523.

[83] R. Mills, *J. Phys. Chem.* **1973**, *77*, 685.

[84] C. Jeanguillaume, P. Trebbia, C. Colliex, *Ultramicroscopy* **1978**, *3*, 237.

[85] B. Langer, I. Schnell, H. W. Spiess, A.-R. d. Grimmer, *Journal of Magnetic Resonance* **1999**, *138*, 182.

[86] M. Holz, H. Weingaertner, *J. Magn. Reson.* **1991**, *92*, 115.

[87] K. Zick, BRUKER BioSpin GmbH, **2009**, p. 27.

[88] D. Massiot, F. Fayon, M. Capron, I. King, S. Le Calve, B. Alonso, J.-O. Durand, B. Bujoli, Z. Gan, G. Hoatson, *Magn. Reson. Chem.* **2002**, *40*, 70.

16 Appendix

16.1 Curriculum Vitae

...

16.2 Acknowledgements

Ich danke allen, die auf unterschiedlichste Art und Weise zum Gelingen dieser Arbeit beigetragen haben.

Mein aufrichtiger Dank gilt meinem Doktorvater … für die Möglichkeit, diese Arbeit in seinem Arbeitskreis am Max-Planck-Institut für Polymerforschung durchführen zu können; insbesondere für die Unterstützung in den letzten Wochen meiner Arbeit.
Meinem Projektleiter … möchte ich für die menschliche Betreuung herzlich danken. Ich bedanke mich für die zahlreichen mir zugestandenen Freiheiten beim Arbeiten und die vielen Diskussionen über den Tellerrand der Fachfragen hinaus.
Ich danke … für seine Geduld, Hilfsbereitschaft und sein stets offenes Ohr, wann immer Probleme auftraten.
Bei allen meinen Betreuern möchte ich mich insbesondere für die offene Atmosphäre und ihr Verständnis bedanken.

Ich möchte mich bei allen Kollegen im Arbeitskreis für das freundschaftliche Miteinander bedanken. Mein spezieller Dank geht an … und … . So ein spezielles und einmaliges Büro wird es nie wieder geben (twis). Danke auch an … für die guten Arbeitsbedingungen an den NMR-Geräten und die gute Organisation.

Ich danke … für die zahllosen DSC Messungen, die wertvollen und unbezahlbaren Orientierungshilfen in den ersten Wochen, sowie ihren besonderen Einsatz. … danke ich für die vielen unterhaltsamen Gespräche und ihre freundliche Art.
… danke ich für sein Interesse, seine Hilfsbereitschaft und vor allem für seine Zeit. Ohne sein Engagement wäre die Arbeit so nicht möglich gewesen und ich weiß das sehr zu schätzen.
Ich danke … für das Bereitstellen des Ofens und die Unterstützung bei den mechanischen Messungen, sowie … und … für die technische Unterstützung rund um die NMR Spektrometer und Probenköpfe. Vielen Dank auch an … , … und … für die Unterstützung bei den Leitfähigkeitsmessungen, die AFM-Messungen bzw. die Elektronenmikroskop-aufnahmen.

Vielen Dank an alle meine Kooperationspartner, auch wenn unsere Ergebnisse keinen Eingang in diese Doktorarbeit gefunden haben:

- … für die Bereitstellung der spannenden Dendrimerproben und die angenehme Kommunikation
- allen Angestellten von … und sonstigen im Projekt eingebundenen Personen für die fachlichen Diskussionen während der zahlreichen Treffen und die Bereitstellung der Photovoltaikfilme. Insbesondere möchte ich … und … danken, mit denen die Zusammenarbeit immer konstruktiv und angenehm war.
- … für die Kooperation im Rahmen der Lithiumleiter. Vielen Dank für die vielen aufheiternden Stunden zu fortgeschrittener Zeit.
- … für die Bereitstellung der Zeolithe.

Vielen Dank an alle Verantwortlichen der Graduiertenschule MAINZ für das Angebot an *Soft Skill* Kursen und *Summer Schools*. In diesem Zusammenhang danke ich insbesondere … und … für ihre Bereitschaft meine Doktorarbeit zu begleiten.

Ich danke vor allem meiner Familie und meiner Freundin … für die bedingungslose Unterstützung und das Vertrauen. Ich konnte mich immer darauf verlassen, dass ihr mir den Rücken frei haltet.